Toughen and recycle plastics with strategically designed polyolefin copolymers

A DISSERTATION
SUBMITTED TO THE FACULTY OF
UNIVERSITY OF MINNESOTA
BY

Jun Xu

IN PARTIAL FULFILLMENT OF THE REQUIREMENTS
FOR THE DEGREE OF
DOCTOR OF PHILOSOPHY

Frank S. Bates

September 2018

Acknowledgement

Firstly, I would like to express my sincere gratitude to my advisor, Prof. Frank Bates, for his guidance and support in my research during the last five years. It was his incredible passion that keeps motivating me and his patience that gives me the strength and courage to carry on. I still remembered when I had a slow start in my first summer, he told me how he struggled because of no background in polymer and then managed to succeed in his own PhD career. He also explained that he had graduated a lot of PhDs and understood that everyone has their own pace. Looking back, I feel so blessed by having such a mentor who is willing to share his research knowledge and life wisdom with me to prepare myself to be a good research scientist and a decent person in general.

Secondly, I am fortunate to work with and learn from many great researchers. I want to acknowledge my collaborators on various projects: Dr. James Eagan, Dr. Sung-Soo Kim, Dr. Kailong Jin, Dr. Michael Maher, Dr. Bongjoon Lee, Sanshui Pan and Micah Howard. I would like to extend my acknowledgement to Dr. Anne Lapointe, Prof. Geoffrey Coates, Prof. Chris Macosko and Prof. Chris Ellison. Even though you are not my advisor, you generously offered me with insightful suggestions otherwise my research wouldn't have gone smoothly. It is really a privilege to work in the polymer group/family. I would like to thank Dr. Jie Lv, Dr. Tuoqi Li, Dr. Yiming Zeng and Dr. Siddharth Chanpuriya for teaching me anionic polymerization, Dr. Chris Thurber for showing me melt processing and rheology, Ronald Lewis for helping me with the X-ray scattering experiments (also continuing to be a colleague at Infineum), Fang Zhou and Chris Frethem for the training and assistance in TEM and SEM, and all the Bates group members for the helpful discussions. I am grateful to Dr. Karen Harman, Dr. Tessie Ewert, Dr. Alex Mannion and

Dr. Tim Gillard for being the big sisters and brothers in the research group and always looking after us. Thank you all for your help along the way!

Thirdly, it is my invaluable asset to get to know and become friends with so many fantastic and helpful people. Thank you all for supporting and helping each other through the overwhelming first two years loaded with countless homework and exams: Xinlong, Motao, Qiong, Xiaolan, Qile, Yaming, Ziang, Hongshi and Chung-hsuan. Thank you all for spending the afternoons with me along Mississippi river, waiting for the fish to bite the bait and then sharing the joy of catch: Yiming, Zichao, Qile, Yan, En & Hongyun and Zhuoran. Thank you for accompanying me in the hiking, BBQ and game nights and putting colors in my life: Tianqi & Motao, Ziang & Wenjia, En & Hongyun, Yiming, Lian, Qile, Kailong, Yan and Han. Thank you, all my workout and bowling buddies: Sung-Soo, Qile, Zhengyuan, Bo, Sanshui, Han, Xiayu & Yangming, En and Maggie. Thank you for your encouragement and support in my job hunting process: Tuoqi, Jing, Jingwen, Lian, Yifeng and Tianqi. Thank you for our everlasting friendship that was affected by time and distance: Chen, Yongxiang, Wenhao, Yujie, Yezhe and Kexin. Special thanks go to Qile and Tianqi. You always showed up and had my back in my toughest moments and through that, you showed me what true friendship is like!

I want to thank my parents for their unconditional love, care, support, understanding and faith in me. Without your efforts to guide me to the right path in my childhood, my life would be totally different, and I could never possibly get to the point I am standing today. Sue and Pete are my host family, whom I respect very much and regard as my parents in the US. They welcomed me in their house with warmth and hospitality and let ‘homeless’ me stay for two weeks when I first came to Minnesota. They have invited me to have dinner,

watch movies and even spend Christmas with their family members for countless times in the last five years. Thank you so much for offering me a home away from home! Last but not least, I would love to thank my beloved girlfriend Yuyang. We have known each other for almost 7 years now. Together we have been through ups and downs but thrived by trusting and relying on each other. Hope I will be the lucky one to have you by my side for the rest of my life.

Dedication

To my beloved family and friends

Abstract

The goal of fabricating materials with better properties and understanding the underlying structure-property-performance relationship has continuously driven research efforts and motivated our work in this thesis. Unique block copolymers have been strategically designed and employed in concert with commercially available resins to achieve blend materials with well-controlled nano-structures and excellent mechanical properties.

We first carried out a model system study of the phase behavior between *i*PP and a series of synthesized copolymers that are potentially miscible with *i*PP according to the conformation asymmetry theory. Though they are not miscible with *i*PP as predicted by theory because of density mismatch, their marginal immiscibility imparted very low interfacial tensions with *i*PP, producing blends with nano-sized dispersed droplets and excellent optical transparency. More interestingly, 5 wt% of these copolymers raised the elongation at break from 20% for neat PP to more than 300%, which is attributable to greatly reduced interparticle distance and cavitation induced shear yielding as evidenced in electron microscopy studies.

With the knowledge learned from the model study, we proceeded to strategically design 'amphiphilic' block copolymers (BCPs) to explore the application of block copolymer micelles for toughening of semi-crystalline *i*PP matrix. When melt blended with *i*PP, these polyolefin block copolymers were uniformly dispersed as sub-100nm micelles. Moreover, these excellent toughening agents increased the tensile toughness by 20 times with merely 5 wt% addition and improved the impact strength by 12 times with 10 wt% addition, and more importantly, no significant deterioration in the elastic modulus or tensile

strength was observed. Electron microscopy revealed coexistence of the cavitated micelles and shear band structure in the matrix of the BCP modified blends, suggesting a cavitation induced shear yielding toughening mechanism. A well-established theory was employed to model the dependence of toughening performance on the modifier size and an optimal size range was identified where particle cavitation and matrix shear yielding can occur simultaneously so that maximum toughness can be achieved.

Lastly, we targeted the grand PP/PE recycling challenge faced by the global society using *i*PP-PE block copolymers synthesized by our Cornell collaborators. The compatibilizing performance of the *i*PP-PE block copolymers was evaluated from two perspectives: blend morphology studied with electron microscopy and interfacial adhesion studied with model T-peel testing. Then the mechanical properties of compatibilized blends were measured with tensile testing. The *i*PP-PE diblock copolymers with high molecular weights and multiblock copolymers with moderate molecular weights are shown to be exceptional compatibilizers, significantly reducing the droplet size in the blend morphology and leading to PE cohesive failure during peel testing. To explain the molecular weight and architecture dependence, we have invoked two mechanisms concerning cocrystallization in diblocks and interlocked entanglements in multiblocks. The finer blend morphology and enhanced interfacial adhesion translate into excellent blend mechanical properties. Tough blends can be obtained with as little as 0.5 wt% BCP, an amazing result that demonstrates the amazing interfacial activity of these BCP species.

Table of Contents

List of Tables

List of Figures

1. Chapter 1: Introduction

1.1 Polyolefin mixing thermodynamics

Polyolefins composed of only carbon and hydrogen atoms are arguably the most important polymers in the world. Polyethylene (PE) and polypropylene (PP) are the world's top two plastics. More than 70 million metric tons (MMT) of PE and 50 MMT of PP are produced annually. They have become indispensable parts of human society, finding applications in nearly every corner of human life and creating great convenience. Meanwhile, however, their recycling has caused great environmental and economic pressure. Despite their almost identical chemical structures, they are immiscible and phase separate from each other at relatively low molecular weights (i.e. several kg/mol) when melt compounded together, which leads to poor blend mechanical properties. To resolve this grand challenge, we need a better understanding of the origin of their immiscibility or more broadly speaking, polyolefin mixing thermodynamics. With this powerful tool, polymers of great use can be strategically designed, for example in this thesis, block copolymer toughening agents and compatibilizers.

The Flory-Huggins theory[1-5] is the most common and convenient framework for understanding the thermodynamic properties of polymer/solvent and polymer/polymer mixtures. It is simply an extension of regular solution theory, giving the following expression for the Gibbs free energy density of mixing of a binary mixture system

$$\frac{\Delta G_m}{k_B T} = \frac{\phi_1}{N_1}\ln\phi_1 + \frac{\phi_2}{N_2}\ln\phi_2 + \chi\phi_1\phi_2 \quad (1)$$

where ΔG_m is the molar free energy of mixing, k_B is the Boltzmann constant, T is the temperature, ϕ_1 and N_1 represent the volume fraction and degree of polymerization of species 1 and χ is the Flory-Huggins interaction parameter which captures the unfavorable interaction energy of mixing unlike segments. For a symmetrical binary mixture system (i.e. N_1 and N_2 are equal, and ϕ_1 =0.5), the critical χN for phase separation is 2.

The interaction parameter χ is strictly the dimensionless interaction energy between two species in regular solution theory, which can be estimated by using the solubility parameters of the two homopolymers in a polymer blend:

$$\chi = \frac{V_{ref}}{RT}(\delta_1 - \delta_2)^2 \quad (2)$$

where V_{ref} is the reference volume, R is the gas constant, T is the temperature and δ_1 and δ_2 are the Hildebrand solubility parameters of species 1 and 2, respectively.

Equation (1) is a crude theory that ignores various nonideal factors in polymer mixtures. For example, Flory-Huggins theory assumes no volume change in the mixing process or differences in thermal expansivity and compressibility, and does not account for interchain contacts and excluded volume.[6, 7] In the 1960's, Flory successfully included thermal expansion and compressibility in their generalized equation of state (EOS) theory to explain the unusual lower critical solution temperature (LCST) phenomena in low molecular weight hydrocarbon mixtures[3, 4]. However, it tends to fail in high molecular weight polyolefin blends characterized with relatively low χ values.

Our understanding towards phase behavior of polymer mixtures has constantly grown in the last several decades via directly measuring χ parameters with innovative

experimental techniques (i.e. X-ray and neutron scattering)[6-13] and predicting thermodynamic properties with simulation methods thanks to fast-growing computation power[14-19]. Among all the progress, there are four main streams of theories that successfully account for the nonideal aspects of polymer blends and are backed by experimental results: namely, lattice cluster theory (LCT), polymer reference interaction site model (PRISM), equation of states (EOS) theory and conformational asymmetry theory.

Freed *et al.*[16, 20, 21] used lattice cluster theory to account for compressibility, different monomer sizes and monomer structure effects on lattice packing, as well as the dependence of χ on chain architecture and monomer sequence in copolymers. Schweizer *et al.*[14, 15] extended the polymer reference interaction site model (PRISM) to polyolefin binary mixtures and found that χ depends on backbone stiffness asymmetry, attractive interaction potential asymmetry, and other thermodynamic variables. Even though they agreed well with some experimental data and can be useful in interpreting results, it is very challenging to put them to practical use due to inherently complicated mathematics.

Graessley and coworkers[10, 22] have examined the relationship between the phase behavior of various polyolefin blends and the equation of state effects of the corresponding homopolymers. They calculated the solubility parameters δ using *PVT* measurements of the pure components and the following expression: $\delta=(\frac{T\alpha}{\gamma})^{1/2}$, where *T* is the temperature, α is the thermal expansion coefficient of the liquid and γ is isothermal compressibility. Then they compared the calculated solubility parameter scheme of pure components (i.e. δ_i and δ_j) to the interaction strengths derived from SANS fitting of binary blends (i.e. $\delta_i-\delta_j$) and found that 75% of the blends obeyed this solubility parameter formalism, which they denoted as regular mixing while the method failed in the 25% of 'irregular' blends.

Recently, Mulhearn and Register[12] further expanded polyolefin pairs by introducing diblocks containing polyethylene and a family of substituted hydrogenated polynorbornenes and found that interaction strengths derived in this series of polymers don't quantitatively follow regular mixing. To advance the EOS theory, White *et al.*[23, 24] have applied a lattice-based equation of state method and correlated the difference in pure component energetic parameters with that of the mixed segment interactions by fitting the pure component EOS to *PVT* data and obtaining the correlated mixed segment interaction parameters. Nevertheless, this method largely relies on accurate measurements of the *PVT* data so it is very challenging to be truly predictive of the phase behavior with pure component properties in a quantitative manner.

In Graessley's work[22], an excellent correlation between the solubility parameter of a polymer and its statistical segment length was observed, which they suggested is a sign of regular mixing with other components. Bates and Fredrickson[7, 25] also examined the influence of statistical segment lengths of pure components/blocks on the blend/block copolymer phase behaviors and established the conformational asymmetry theory. They reported that the magnitude of χ is related to the asymmetry in the statistical segment lengths of the two components or blocks in polyolefins.[6] It was speculated that the nonlocal conformational rearrangement of two molecules occupying different volumes caused the excess free energy in mixing. They have used a parameter β (originally defined by Helfand and Sapse[26]), an invariant combination of pure component parameters as follows:

$$\beta_i^2 = \frac{R_{g,i}^2}{V_i} = \frac{b_i^2}{6v_i} \tag{3}$$

where $R_{g,i}$ is the radius of gyration, V_i is the chain volume, b_i is the statistical segment length and v_i is arbitrarily defined reference volume, to quantitatively capture the space-filling

characteristics of a flexible polymer coil. Using this mathematical context, they speculated that miscibility can be achieved if $\beta_1=\beta_2$. And when the same reference volume is used, β only depends on the statistical segment length b and therefore polyolefins with close b values will form miscible blends. The b values can be obtained by measuring the radius of gyration (R_g) of a polymer and the relation:

$$R_g = b(N/6)^{1/2} \tag{4}$$

where N is the number of statistical segments per polymer.

In Table 1.1, we have summarized the chemical structures and statistical segment lengths of a series of polyolefins with the same reference volume of 118 $Å^3$ approximately corresponding to that of a four-carbon repeat unit at 140 °C. The statistical segment length of a random copolymer can be estimated by $b^2 = \sum \phi_i \cdot b_i^2$, where ϕ_i and b_i are the volume fraction and statistical segment length of the pure components.

As predicted by Schweizer and shown experimentally by Graessley (i.e. in irregular mixing), molecular asymmetry is not the only factor governing miscibility in polyolefins, thus arguments based solely upon molecular conformation are too simple to provide a general explanation of polyolefin thermodynamics. Nevertheless, when $b_1=b_2$, conformational symmetry appears to result in miscible blends. For example, random copolymers of ethylene and ethyl ethylene which possess ethyl ethylene contents ranging from 0.58 to 0.96 were found to be melt-miscible with *i*PP, which is consistent with the conformational asymmetry concept.[27, 28] In this thesis, we aim to further advance our understanding of polyolefin mixing thermodynamics and also exploit knowledge learned to prepare useful block copolymer additives for PP toughening and PP/PE compatibilization.

Table 1.1 Statistical segment length and chemical structures of polyolefins at 140 °C

Polymer	Chemical structure	*b* (Å)
PE[a]	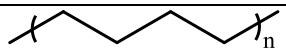	8.4[b]
PEP[c]	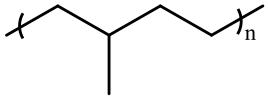	6.8[b]
*i*PP	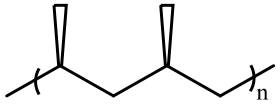	6.2[d]
PEE[e]	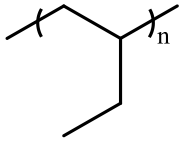	5.1[f]
PCHE[g]	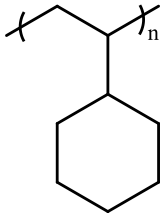	4.6[b]

a. This PE is a hydrogenated polybutadiene composed of 93% 1,4 and 7% 1,2 units
b. Values are taken from Cochran and Bates, *Macromolecules*, 2002 (Reference 29)
c. Poly(ethylene-*alt*-propylene) (PEP) is a hydrogenated polyisoprene composed of 94% 1,4 and 6% 3,4 units
d. Value is taken from Weimann *et al.*, *Macromolecules*, 1999 (Reference 27)
e. Poly(ethyl ethylene) (PEE) is a hydrogenated polybutadiene composed of 100% 1,2 unit
f. Value is taken from Bates *et al.*, *Macromolecules*, 1992 (Reference 6)
g. Poly(cyclohexyl ethylene) (PCHE) is a hydrogenated polystyrene

1.2 Isotactic polypropylene toughening with block copolymers

The major market driver for isotactic polypropylene is the automotive industry, aiming to reduce vehicle weight and therefore increase fuel efficiency. As the major

components of bumpers, *i*PP suffers from poor impact resistance. Blending has been the most widely used and efficient approach to enhance material properties including morphological, mechanical, electrical, biological and surface properties as seen in various matrices[30-36]. The majority of *i*PP toughening research has focused on traditional rubbers[37-40], i.e. ethylene propylene rubber (EPR) and ethylene-propylene-diene-monomer (EPDM) rubber, rigid fillers[41-46] and composite systems composed of both ingredients[47-50]. Rigid particles are generally less effective than rubbers as they greatly deteriorate the tensile elongation at break at high filler concentrations. On the other hand, when *i*PP is toughened with rubbers, there is always a tradeoff between high toughness and strength since the presence of a large amount of rubbers lowers tensile strength; moreover, this approach renders opaque products that are not ideal in packaging applications. While for ternary blends of *i*PP, rubbers and rigid fillers, it is hard to control the morphology. Consequently, the mechanical properties are somewhat unpredictable so that tedious screening and optimization process is required. Few good examples are reported in the literature. Some special rubbers, such as styrene-butadiene based[51] and olefin-based block copolymers[52, 53], have been applied in *i*PP toughening. Even though they are more effective than traditional rubbers, a relatively large amount (~ 20 wt%) is still required to produce desirable toughness. In this thesis, we are aiming to exploit mixing thermodynamics to design superior *i*PP toughening agents.

The toughening mechanism of *i*PP modified with rubbers and rigid particles has been extensively investigated in the last several decades.[45, 46, 54-59] The universally accepted toughening process are often described by the following sequence of events:

1) Stress concentration: Elastic deformation leads to stress concentration around the dispersed particles due to stiffness mismatch between the matrix and particles. The stress concentration then causes three-dimensional stresses around the particles and the surrounding matrix materials.
2) Void formation: In rubber toughened *i*PP, cavitation will occur inside the rubber particle and give rise to nano or microvoids.[54, 60-62] As for rigid particle filled *i*PP, because the Young's modulus of the filler is too high to allow deformation, debonding at the interface will take place, resulting in the formation of microvoids.[63, 64] In both cases, due to void formation, the volumetric constraints on the matrix around the particles are released, facilitating crazing and shear yielding.
3) Local plastic deformation: Because of released volumetric strain, local plastic deformation of the matrix can occur through multiple crazing, extensive shear yielding or combination of both depending on the matrix material, blend morphology and testing conditions (i.e. temperature, testing speeds). Local shear yielding in semi-crystalline matrices proceeds by shear of crystals involving crystallographic slip mechanisms and amorphous layers (interlamellar shear).[60]
4) Extensive matrix plastic deformation: A large volume of matrix undergoes extensive plastic deformation and a large amount of energy is absorbed. The stretching of well-bonded rubber particles can also significantly contribute to this absorption process. Meanwhile, the strain hardening stabilizes the deformation process and prevents stress localization which can otherwise result in crack growth and premature fracture. The rigid particles embedded in the matrix can blunt the

crack tip and slow down or even stop crack propagation, which is very important in crazing-prone matrices.

The prerequisite for realizing the discussed events and producing tough blends is to facilitate particle cavitation which is largely dictated by the particle size. Various morphologies of cavitated rubber particles are provided in Figure 1.1. Initial morphologies (homogenous and heterogenous, core-shell particles) and adhesion between the components dictate the morphology produced by cavitation and debonding, which can be single cavitation, fibrilized cavitation, multiple cavitation, single-site debonding or fibrilized debonding as shown in Figure 1.1.

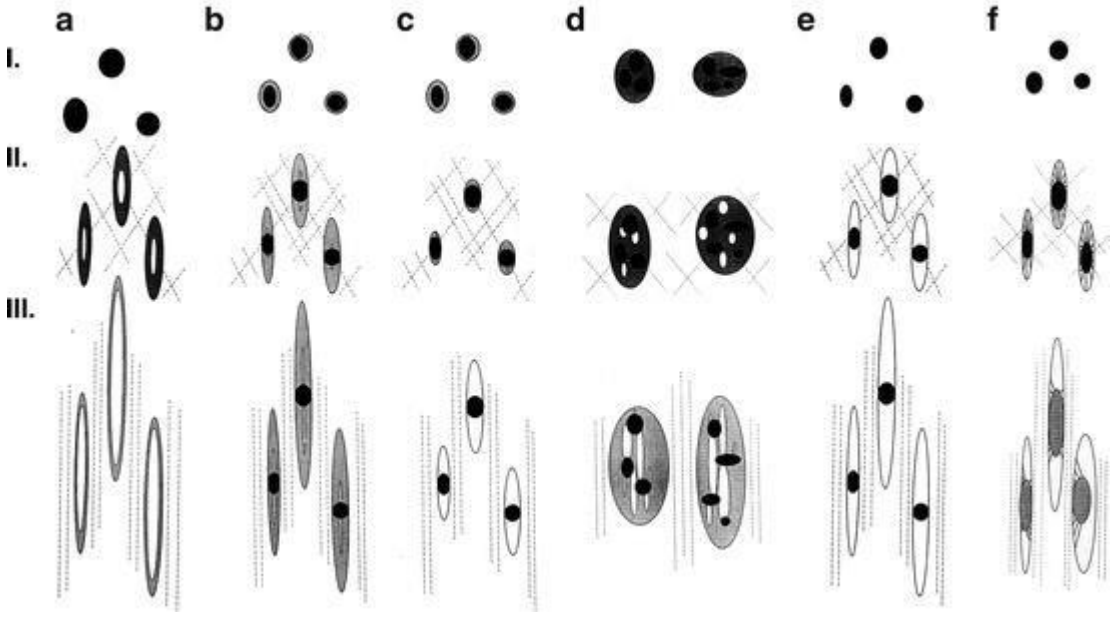

Figure 1.1 Various morphologies produced by cavitation and debonding: (a), (b) single cavitation in homogenous and heterogenous particles, respectively; (c) fibrilized cavitation; (d) multiple cavitation; (e) single debonding; and (f) fibrilized debonding. I. initial morphology, II. Low strain, III. High strain. (Reproduced from Barczak and Galeski[65] with permission of Springer)

It is commonly observed that glassy matrices tend to deform by crazing and benefit from larger particles (i.e. 1-5 μm in diameter) while matrices that absorb energy by shear

yielding, such as *i*PP, are more effectively toughened with smaller particles (0.5 μm or less in diameter)[65]. The particle sizes reported in the past rubber toughened *i*PP works are usually larger than 1 μm, which falls outside of the optimal range and is a possible source of inefficiency in toughening. Rheological properties of the matrix and dispersed phase, and processing conditions are the dominant factors in determining particle size, which is not easily altered in a given blend system. We are seeking alternative methods to reduce the particle size to bring it to the optimal range. Specially designed 'amphiphilic' block copolymers that can self-assemble into nano-size micelles in matrices have been proven to dramatically toughen thermosets[66-73] and thermoplastics[74, 75]. We aim to apply the same approach in the *i*PP matrix, where block copolymers are driven to go through a micellization process by the thermodynamic interactions between *i*PP and block copolymer chains, as shown in the schematic of Figure 1.2. In the melt state (i.e. melt compounder), the blue *i*PP-immiscible chains are incompatible with *i*PP and try to minimize the contacts, while the red *i*PP-miscible chains are compatible with *i*PP, thus forming micelles with blue cores and red coronas.

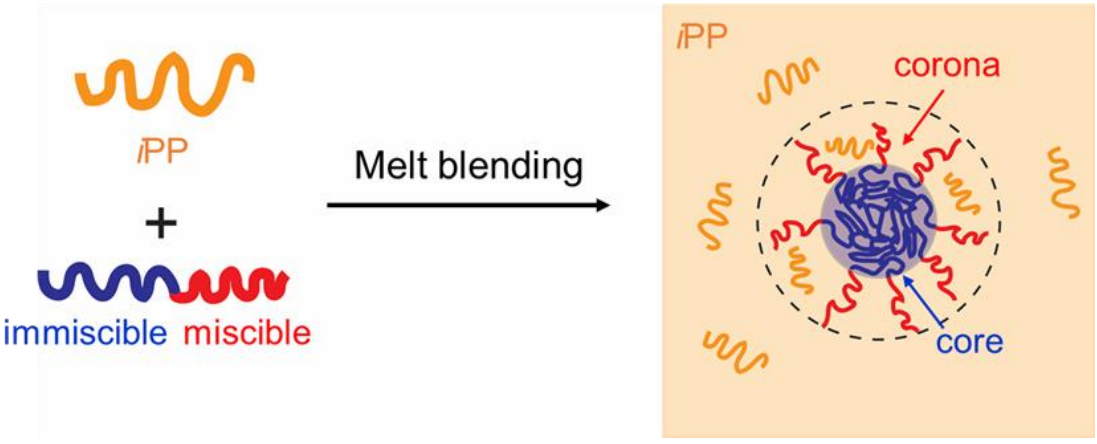

Figure 1.2 Schematic of the micellization process of block copolymer modified *i*PP in the melt state.

The micelle sizes and shapes can be readily tuned by varying the block copolymer molecular weight and composition[66, 67, 71], enabling the possibility of investigating particle size and shape effects on toughening independently. Furthermore, with simple adjustments in synthesis, micelles with different core contents (i.e. rubbery, glassy and semicrystalline) can be synthesized which will have different tendencies to cavitate when subjected to stress. This may offer some fundamental insights into the role of particle cavitation in determining the blend toughness. Tough blends modified with block copolymer micelles are expected to be recognized after this comprehensive and systematic work.

1.3 Isotactic polypropylene and polyethylene compatibilization

As alluded to in Section 1.1, PE and PP phase separate from each other at any commercially relevant molecular weights (i.e. $\chi > 10^{-3}$) and make blends with poor mechanical properties when they are melt compounded together, requiring compatibilization to effectively tackle this issue and fabricate blends with better properties.

One approach is called reactive compatibilization, which is conducted by introducing chemical reactions between functionalized PP and PE polymers[76-79] or promoting chemical reactions between PP and PE with low molecular weight reactive compounds (i.e. peroxides)[80-83]. Since functionalized PP is miscible with PP and resides in PP domains, and the same thing happens in PE side, PP-PE copolymers will be formed at the interface upon chemical reactions. Colbeaux *et al.*[78] added anhydride-grafted PP and anhydride-grafted PE along with coupling agents in the PP/PE blends and achieved finer dispersions with smaller and stable droplet size in static and dynamic conditions. Other

work by Tselios *et al.*[77] utilized esterification reactions between anhydride and hydroxyl groups of added anhydride-grafted PP and polyethylene-*co*-vinyl alcohol, respectively, and demonstrated improved morphology and mechanical properties in PP/PE blends. However, there are several requirements for effective reactive compatibilization: (1) the reactions have to be completed faster than the compounding residence time; (2) the formed chemical bonds need to be stable under processing conditions; (3) preferentially, environmentally benign reagents should be used. All of these greatly limit the applicable chemical reactions. Furthermore, polyolefins are difficult to functionalize, making functionalized polymers much more expensive than the unmodified counterparts.

The other option is to couple PP and PE chains with peroxides so that the immiscible interfaces can be stitched together.[80-83] Nevertheless, it was found that PP undergoes mostly chain scission while PE undergoes crosslink reactions at low peroxide concentrations. At higher concentrations, degradation reactions will dominate and deteriorate the mechanical properties. This approach is not favorable because of uncontrolled degradation and therefore it has been seldom adopted in recent works.

A significant amount of scientific work has been conducted with a more practical and simpler approach, which is to add premade compatibilizers in the melt blending process[84-94]. Appropriately designed, the compatibilizers will tend to go to interfaces in phase separated blends and form a steric barrier that prevents coalescence, effectively stitching the interface, reducing interfacial tension, facilitating smaller droplet formation and sterically stabilizing the blend morphology. Furthermore, in the solid state, when subjected to stress, the compatibilizer layer can promote the stress transfer between the matrix and dispersed phase so that they can plastically deform together[93]. EPR[84, 85, 90] and

EPDM[86, 91, 95] rubbers are the most widely used compatibilizers for PP/PE blends because of their low cost and easy processibility. The ethylene rich-segments are expected to associate with the PE phase and propylene-rich segments will go to the PP phase. However, the EPR and EPDM rubbers can form their own separated domains rather than encapsulating and 'emulsifying' the minor phase, making them less effective. A large amount of EPR or EPDM compatibilizers (> 10 wt%) is usually required to observe significant compatibilizing effects, which reduces the tensile strength.

Block copolymers composed of PP-miscible and PE-miscible chains are considered as more effective alternatives than EPR and EPDM. Lin and coworkers[94] systematically compared a multiblock ethylene-octene copolymer, two random ethylene-octene copolymers, two propylene-ethylene copolymers, and a styrene-based block copolymer as PP/PE compatibilizers and found that with 10 wt% olefin block copolymers (OBC) addition, the low-temperature tensile properties of the blends were dramatically improved due to enhanced adhesion between PP and PE domains. But due to the chain shuttling chemistry for OBC synthesis, the detailed chemical structures of OBC are not well defined, so it is challenging to perform fundamental studies on how the block copolymer molecular weights and compositions affect the compatibilizing performance. In another study, Chaffin *et al.*[96] synthesized PE-PEE$_E$ block copolymers by anionic polymerization and hydrogenation and investigated their performance as PP/PE compatibilizers. They found that the amorphous PEE$_E$ chains were not able to co-crystalize with PP homopolymers, diluting the crystallizable content at the interface and leading to poor mechanical properties. Their work outlines a key characteristics of an ideal block copolymer compatibilizers: the blocks need to be miscible and have the capability to co-crystallize with the corresponding

homopolymers. In this thesis, with the pyridylamidohafnium catalysts developed by the Coates group at the Cornell University, semi-crystalline PP-PE block copolymers with almost identical chemical structures as commercial PP and PE, and easily tunable molecular weights and architectures can be obtained. They are potentially ideal PP/PE compatibilizers and perfect tools to investigate the influencing factors for compatibilizing performance.

1.4 Thesis overview

The goal of fabricating materials with better properties and understanding the underlying structure-property-performance relationship has continuously driven research efforts and motivated our work in this thesis. We have designed and employed unique block copolymers in concert with commercially available resins to achieve blend materials with well-controlled nano-structures and excellent mechanical properties.

The work presented in this dissertation has been divided into six chapters. Firstly, in Chapter 2, the basic experimental procedures and techniques including materials (commercial resins and synthesized polymers), sample preparation and characterization (microstructure, thermal, mechanical and rheological) that are commonly used in the work presented in Chapter 3-5 are introduced.

Chapter 3 describes a model system study of the phase behavior between *i*PP and a series of synthesized copolymers that are potentially miscible with *i*PP according to the conformation asymmetry theory discussed in Section 1.1. Though they are not miscible with *i*PP as predicted by theory because of density mismatch, their marginal immiscibility

imparted very low interfacial tensions with *i*PP, producing blends with nano-sized dispersed droplets and excellent optical transparency. More interestingly, 5 wt% of these copolymers raised the elongation at break from 20% for neat PP to more than 300%, which is attributable to greatly reduced interparticle distance and cavitation induced shear yielding as evidenced in electron microscopy studies. This chapter sheds light on the polyolefin mixing thermodynamics and demonstrates a practical approach to preparing mechanically tough and optically clear polypropylene blends with controlled particle sizes by tuning the statistical segment length and density mismatches.

In Chapter 4, the application of block copolymer micelles for toughening of semi-crystalline *i*PP matrix with strategically designed 'amphiphilic' block copolymers (BCPs) is presented. When melt blended with *i*PP, these polyolefin block copolymers were uniformly dispersed as sub-100nm micelles. Moreover, these superior toughening agents increased the tensile toughness by 20 times with merely 5 wt% addition and improved the impact strength by 12 times with 10 wt% addition. Electron microscopy revealed coexistence of the cavitated micelles and shear band structure of the matrix in the BCP modified blends, suggesting a cavitation induced shear yielding toughening mechanism. A well-established theory was employed to model the dependence of toughening performance on the modifier size and an optimal size range was found where particle cavitation and matrix shear yielding can occur simultaneously and superior toughness can be achieved. This chapter demonstrates the universal applicability of the BCP micelle toughening technique in various matrices and provides valuable insights into the blend toughening mechanism.

Chapter 5 describes PP/PE blends compatibilized with the *i*PP-PE block copolymers synthesized by our Cornell collaborators. This work targets the grand challenge faced by the global society of PP/PE recycling. The compatibilizing performance of the *i*PP-PE block copolymers was evaluated from two perspectives: blend morphology studied with electron microscopy and interfacial adhesion studied with model T-peel testing. Then the mechanical properties of compatibilized blends were measured with tensile testing. The *i*PP-PE diblock copolymers with high enough molecular weights and multiblock copolymers with moderate molecular weights are shown to be exceptional compatibilizers, significantly reducing the droplet size in the blend morphology and leading to PE failure in the peel testing. To explain the molecular weight and architecture dependence, we have invoked two mechanisms concerning cocrystallization in diblocks and interlocked entanglements in multiblocks. The finer blend morphology and enhanced interfacial adhesion translate into excellent blend mechanical properties. Tough blends can be obtained with as little as 0.5 wt% BCP, an amazing result that demonstrates the unparalleled interfacial activity of these BCP species. This chapter introduces a BCP additive that can potentially bring a practical solution to the PP/PE recycling issue and revolutionize the recycling industry and furthermore underlines the importance of having crystallizable blocks in the BCP compatibilizers.

Finally, Chapter 6 presents a summary of this thesis work and offers several future research directions. For *i*PP toughening, hybrid micelles with various core contents, composite systems composed of micelles and rigid particles, and micelle toughening combined with beta modification of *i*PP matrix are worth exploring to prepare even tougher materials. For the PP/PE compatibilization work, a mechanistic study is still required to

help elucidate the source of superior interfacial activity and better understand the effects of molecular weight and architecture on compatibilization performance. Furthermore, different architectures (i.e. graft copolymers) and different chemistries (i.e. chain shuttling) will be explored to find even more effective and economically viable compatibilizers.

2. Chapter 2: Materials and experimental methods*

2.1 Introduction

This chapter introduces the materials and experimental methods used in our work. First, the information of all the commercially available polyethylene and isotactic polypropylene materials will be presented followed by the detailed description of the synthesis of poly(cyclohexyl ethylene-*ran*-ethylene) (CE) random copolymers reported in Chapter 3 and block copolymer toughening agents described in Chapter 4 using anionic polymerization and catalytic hydrogenation techniques. Then sample preparation methods to prepare blends of synthesized polymers and commercial resins using melt compounding are described. Last, we elaborate on the experimental techniques utilized to characterize the blend systems. Blend morphology and microstructure change during deformation were investigated through scanning electron microscopy (SEM) and transmission electron microscopy (TEM). The thermal analysis of neat polymers and polymer blends was conducted with differential scanning calorimetry (DSC). Mechanical properties were evaluated through standard tensile testing and Izod impact testing according to ASTM

*Synthetic schemes reproduced in part with permission from (Xu, J.; Mittal, V.; Bates, F. S. "Toughened Isotactic Polypropylene: Phase Behavior and Mechanical Properties of Blends with Strategically Designed Random Copolymer Modifiers", *Macromolecules*, American Chemical Society) and (Xu, J.; Howard, M. J.; Mittal, V.; Bates, F. S. "Block Copolymer Micelle Toughened Isotactic Polypropylene", *Macromolecules*, American Chemical Society)

standards. Rheology was employed to determine the order-disorder transition temperature in block copolymers and estimate the interfacial tensions between the coexisting components in blends.

In general, the descriptions in this chapter summarize the techniques that the commonly referred to in subsequent Chapters 3-5. Experimental details that are unique to specific chapters (e.g. the synthesis of *i*PP-PE block copolymers and T-peel testing) can be found in the experimental section of those chapters.

2.2 Commercial polyethylene and polypropylene resins

Isotactic polypropylene (HD915CF, Borouge, Abu Dhabi, United Arab Emirates) with a melt flow index (MFI) of 8.0 g/10min (230 °C/2.16 kg) was generously provided by our collaborators and used as the brittle matrix material that requires toughening in Chapter 3 and 4. Isotactic polypropylene (H314-02Z (discontinued now), MFI = 2.0 g/10 min at 230 °C with 2.16 kg) and HDPE (DMDA8904, MFI = 4.4 g/10 min at 190 °C with 2.16 kg) in the compatibilization work of Chapter 5 were both obtained from Dow Chemical Company and used as received.

2.3 Polymer synthesis

2.3.1 Poly(cyclohexyl ethylene-ran-ethylene) (CE)

CE copolymers were synthesized by anionic random copolymerization of styrene and butadiene using a modified version of the method reported by Sardelis *et al.*[97] followed

by heterogeneous catalytic hydrogenation, as shown in Figure 2.1. Styrene (Sigma Aldrich Reagent Plus) was purified by vacuum distillation twice from di-*n*-butyl magnesium and butadiene* (Sigma Aldrich, ≥99%) was purified by vacuum distillation twice from *n*-butyllithium (*n*-BuLi). Cyclohexane was purified over an alumina column as described elsewhere.[98] Potassium *tert*-butoxide (1.0 M in THF, Sigma Aldrich) was employed at a molar ratio of 0.05 relative to the initiator to facilitate the random copolymerization of the two monomers; it was added to a Schlenk reaction flask, completely dried and pressurized with purified argon followed by complete THF removal under dynamic vacuum prior to the addition of cyclohexane. The initiator *n*-BuLi was injected into the flask and stirred in the solution for 15 min before monomers were added. Polymerizations were conducted at 40 °C for 8 h and then terminated with methanol, followed by precipitation of the product in methanol, vacuum drying, and by freeze-drying from benzene.

The heterogeneous catalytic hydrogenation of poly(styrene-*ran*-butadiene) (SB) was performed using a high-pressure reactor operating at 170 °C with H_2 at a pressure of 500 psi. Cyclohexane solutions containing 10-15 g/L of polymer were reacted for 17 hours over a Pt/Re catalyst supported on S_iO_2. The catalyst was removed from the product by filtration and the CE copolymer was recovered by precipitation in methanol followed by vacuum drying overnight at 100 ºC. Complete hydrogenation (>99.9%) without any discernable degradation was confirmed by ^{1}H NMR and SEC analyses.

*__Safety Note__: Butadiene is a gaseous monomer with a boiling point of -4.4 °C and thus needs to be carefully handled

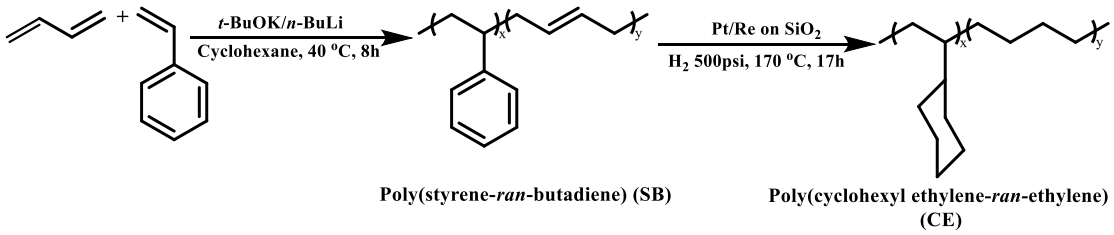

Figure 2.1 Synthetic scheme for the preparation of poly(cyclohexylethylene-*ran*-ethylene) (CE) copolymer. Random copolymerization of styrene and butadiene[97] is followed by heterogeneous catalytic hydrogenation.[99]

2.3.2 Poly(ethylene-*alt*-propylene)-*b*-poly(ethylene-*ran*-ethyl ethylene) (PEP-PEE$_E$)

PEP-PEE$_E$ diblock copolymers were synthesized by sequential anionic polymerization of isoprene and butadiene followed by catalytic hydrogenation as shown in Figure 2.2. Cyclohexane was collected from an alumina column as described above. Isoprene (Sigma-Aldrich, ≥99%) and butadiene (Sigma-Aldrich, ≥99%) were purified by distillation from *n*-butyllithium (*n*-BuLi) twice and transferred into clean and dry burettes. *n*-BuLi was injected into the solvent contained in a Schlenk reactor blanketed with purified argon followed by the addition of isoprene, which was allowed to react for 6 h at 40 °C. An aliquot of the living polymer was extracted by cannula to determine the molecular weight and dispersity then the reactor was cooled to 20 °C and butadiene was added along with a small amount of tetrahydrofuran (THF) ([THF]:[*n*-BuLi] = 200:1). The reaction was terminated with degassed methanol after another 18 h and the diblock copolymer was recovered by precipitation in cold methanol followed by vacuum drying and subsequent freeze drying from benzene.

The PI-PB diblock copolymers were dissolved in cyclohexane at a concentration of 10-20 g/L and hydrogenated to PEP-PEE$_E$ in a high-pressure reactor at 170 °C with 500 psi H_2 for 20 h using a SiO_2 supported Pt/Re catalyst.[99] Then the resulting solution was

filtered to remove the catalyst and the polymer product was precipitated in cold methanol and dried in a vacuum oven at 100 °C overnight.

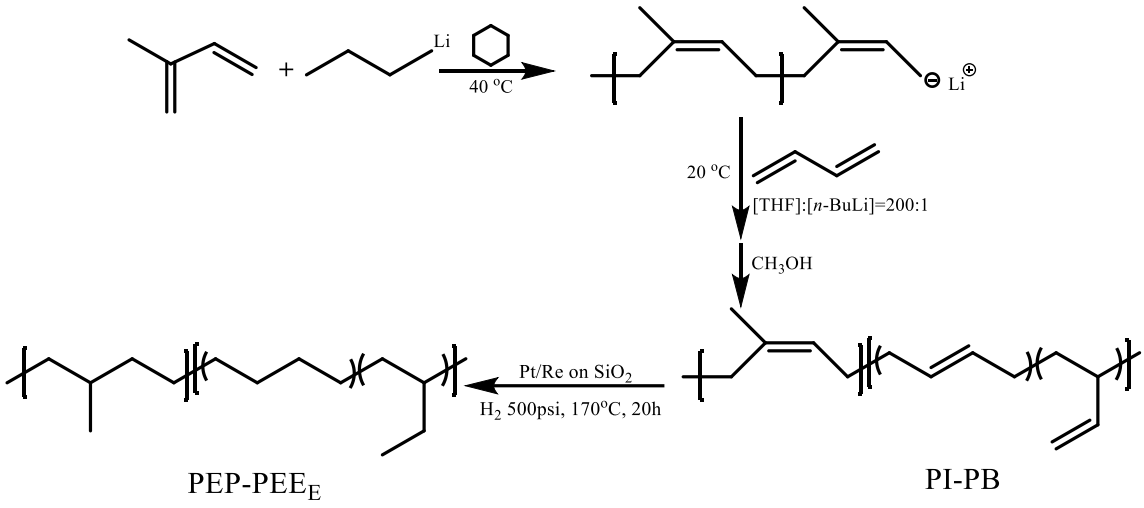

Figure 2.2 Synthetic scheme for PEP-PEE$_E$ diblock copolymers. Sequential anionic polymerization of isoprene and butadiene is followed by catalytic hydrogenation.

Other 'amphiphilic' diblock copolymers, i.e. poly(ethylene)-*b*-poly(ethylene-*ran*-ethyl ethylene) (PE-PEE$_E$) and poly(cyclohexyl ethylene)-*b*-poly(ethylene-*ran*-ethyl ethylene) (PCHE-PEE$_E$) can be synthesized by changing the first monomer to butadiene and styrene respectively.

2.4 Sample preparation

Blends of the CE copolymers and *i*PP with 5-20 wt% CE were prepared using a recirculating, conical twin-screw batch mixer (DSM Xplore, 5mL capacity) operated at 100 rpm with a barrel temperature of 180 °C and extruded into cold water to form thread-like sample as shown in Figure 2.3.

Figure 2.3 DSM Xplore microcompounder with circulating and conical twin-screws (left) and extruded samples after water cooling and drying (right).

Blends of *i*PP and PEP-PEE$_E$ block copolymers (BCP) with 1.25-20 wt% BCP modifiers were prepared with the same procedure as discussed above. Larger batches of blends (100 -150 g) with 5-10 wt% BCPs were prepared with 200 ppm antioxidant BHT using a 16-mm twin-screw extruder (PRISM, L:D 24:1, four heating zones at 180 °C and a feed zone at 130 °C) operated at screw speed 30-35 rpm followed by water cooling, air drying and pelletizing. The pellets were fed and extruded again to eliminate potential inhomogeneity in the blends.

2.5 Morphology and microstructure characterization

2.5.1 Transmission electron microscopy (TEM)

TEM was employed to investigate the *i*PP/PEP-PEE$_E$ blend morphology and determine the BCP micelle size and distribution. Prior to any mechanical testing, bulk

specimens were cryo-sectioned at -120 °C using a Leica EM UC6 ultramicrotome (Model FC-S Cryo attachments) fitted with a trimming knife. This was done perpendicular to the gauge direction for compression molded samples, and perpendicular to the flow direction for injection molded ones; then the smooth surface was stained with a freshly prepared RuO_4 solution for 120 min.[100] A plastic pippette of sodium hypochlorite solution (1 ml of 10w/v%) was added to 15-20 mg of $RuC1_3 \cdot 3H_2O$ in a 5 ml glass vial and immediately capped. Samples were fastened to the inside of the vial cap with adhesive tape and stained by the RuO4 vapours above the reddish-brown staining solution for 2h. Following staining, the specimen should de-gas in thefume hood for several hours prior to ultramicrotomy. Ultrathin sections (c.a. 100 nm) were obtained by cryo-microtoming the stained smooth surface at -120 °C with a Micro Star diamond knife and then collected on copper grids. To study the toughening mechanism, specimens were stretched to yield point and subject to the same TEM section preparation protocols except that whitened gauge areas were used. Samples were imaged using a Tecnai G2 Spirit Biotwin microscope with an accelerating voltage of 120 kV.

2.5.2 Scanning electron microscopy (SEM)

The morphology of *i*PP/CE blends and microstructure change after tensile testing, tensile specimens were evaluated using specimens cryo-fractured in liquid nitrogen perpendicular to the tensile direction before and after mechanical testing. Fractured specimens were cut with a fresh razor blade along the tensile direction and the surfaces were sputtered with a thin layer of gold-platinum coating (ca. 50 Å) to prevent charging.

The microscope was operated with an accelerating voltage of 5 *k*V and a working distance of around 10 mm.

SEM was also utilized to study the blend morphology of *i*PP/PEP-PEE$_E$ and fracture surfaces of Izod impact specimens. Pristine tensile bars were cryo-fractured in liquid nitrogen, immersed in tetrahydrofuran for at least 24 h to extract the diblock copolymer from the *i*PP matrix and dried at room temperature in a vacuum oven overnight. Fracture surfaces were imaged without any further processing after the Izod impact tests. To image the microstructure of the whitened zone under the Izod fracture surface, the specimen was cut open perpendicular to the notch with a fresh razor blade. All SEM specimens were sputter coated with a 5-nm thick iridium layer to prevent charging before being examined using a Hitachi S4700 field emission scanning electron microscope with 5 *kV* accelerating voltage and approximately 10 mm working distance.

2.6 Thermal analysis

The glass transition temperatures (T_g) and melting (T_m) and crystallization (T_c) temperatures of the SB and CE copolymers, and PEP-PEE$_E$ block copolymers were characterized with differential scanning calorimetry (DSC). Samples (5-10 mg) were contained in hermetically sealed aluminum pans and analyzed with a TA Q1000 differential scanning calorimeter instrument. Specimens were first heated to 200 °C at a rate of 10 °C/min and held at this temperature for 10 min to erase any thermal history in the materials, then cooled to -100 °C and heated to 200 °C both at a rate of 10 °C/min. The

reported T_g and T_m values were determined from the second heating cycle and T_c values were obtained from the first cooling cycle.

2.7 Mechanical performance evaluation

Tensile testing. Dumbbell-shaped tensile bars (ASTM D1708, 0.6 mm thick, 5 mm gauge width, 22 mm gauge length) were compression molded at 180 °C and 3 MPa pressure for 5 min using a Carver hot press followed by water cooling to room temperature. Tensile tests were conducted at room temperature using a Shimadzu AGX tensile tester operated at a crosshead speed of 5 mm/min. At least 10 samples were tested to allow meaningful statistical analysis.

Notched Izod impact testing. Izod impact specimens (ASTM D256) were molded with a Morgan Press injection molder (barrel temperature = 220 °C, nozzle temperature = 230 °C and mold temperature = 50 °C) and notched with a CEAST NotchVis notcher. Notched Izod impact strength was determined using a CEAST impact strength tester (model 6545). All specimens were aged at room temperature for 72 h prior to testing. A specimen is displayed in Figure 2.4 with the following dimensions: a = 10.16 ± 0.05; b = 31.8 ± 1.0; c = 63.5 ± 2.0; e = 12.7 ± 0.20 in mm. The impact strength is reported in units of either J/m or kJ/m^2, calculated by dividing the impact energy (J) by the specimen thickness or the area under the notch (thickness × a) respectively. At least 10 parallel tests were performed to obtain statistically significant impact properties. The equiments employed are displayed in Figure 2.5.

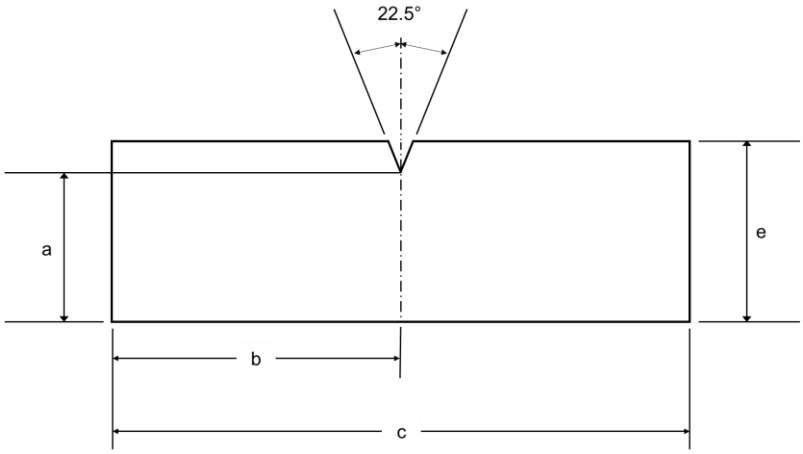

Figure 2.4 Izod-type specimen according to ASTM D256.

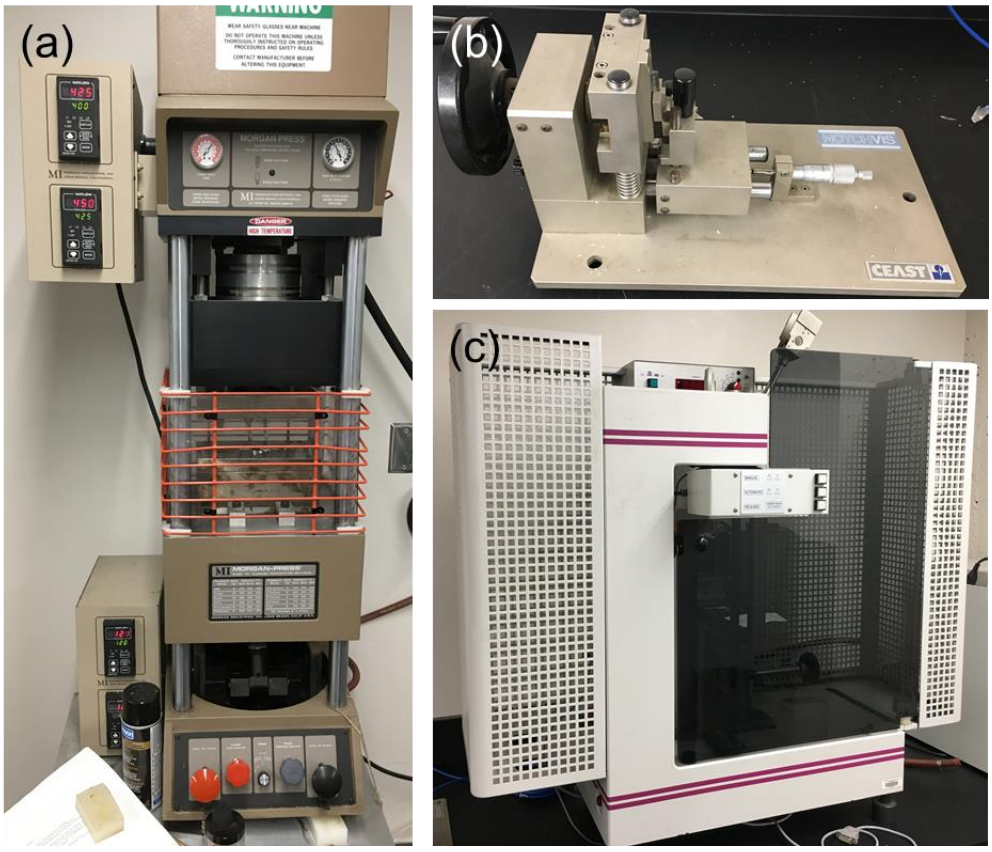

Figure 2.5 (a) Injection molder, (b) CEAST manual notcher and (c) Izod impact tester with adjustable energy scale.

2.8 Rheology

Rheological measurements were conducted to estimate the interfacial tensions between the CE copolymers and *i*PP matrix in the melt state. The measurements were made on an ARES rheometer using a 25-mm parallel plate configuration with a gap between 0.8 and 1.0 mm. Experiments were performed between 180-260 °C over a frequency range of 0.01-100 rad/s. Data obtained at different temperatures were reduced to a master curve with a reference temperature of 180 °C using the time-temperature superposition principle. Depending on the temperature and frequency, the strain was set to between 1 and 25% to obtain a sufficient torque value; strain sweep experiments verified that the measurements were conducted in the linear viscoelastic regime.

For the determination of ordered-disordered transition temperature (T_{ODT}) of the PEP-PEE$_E$ block copolymers, samples were loaded at room temperature and temperature ramps from 30 to 120 °C at a heating rate of 10 °C/min were conducted followed by frequency sweep experiments over a range of 0.1 rad/s -100 rad/s at various temperatures with a 10 °C increment. While for the PE-PEE$_E$ and PCHE-PEE$_E$ block copolymers, samples were loaded to the rheometer at 180 °C because of the T_m of PE and the T_g of PCHE and followed by a temperature ramp to 250 °C at a heating rate of 10 °C/min to probe the potential T_{ODT} and frequency sweeps at various temperatures with a 10 °C increment.

3. Chapter 3: Phase behavior and mechanical properties of isotactic polypropylene (*i*PP) and a new class of poly(cyclohexyl ethylene-*ran*-ethylene) copolymers (CE)*

3.1 Introduction

This chapter presents the design of a new class of model polyolefin random copolymer with various cyclohexyl ethylene (C) and ethylene (E) contents and the study of phase behaviors between these materials and a commercial *i*PP homopolymer. It provides some fundamental understanding of the mixing thermodynamics and the structure (morphology)-property-performance relationship in polyolefin blends.

Isotactic polypropylene is used in a plethora of industries such as packaging, textile, automotive, electrical, medical and construction owing to good processability, excellent chemical resistance, low density and low cost. However, application of *i*PP as an engineering plastic is often limited due to its intrinsic brittleness at low temperatures or high strain rates. Extensive research has been conducted over the past several decades with

* Reproduced in part with permission from (Xu, J.; Mittal, V.; Bates, F. S. "Toughened Isotactic Polypropylene: Phase Behavior and Mechanical Properties of Blends with Strategically Designed Random Copolymer Modifiers", *Macromolecules,* American Chemical Society)

the aim of improving in the ultimate properties of *i*PP, especially the impact toughness[38, 41, 43, 45, 59, 101-103]. Compounding or blending with immiscible additives, which offers an effective and economical approach to creating materials with enhanced toughness, has been a particular focus.

Cavitation, shear yielding and crazing are the main toughening mechanisms operative in *i*PP blends, similar to what governs toughness in thermoset epoxy and certain other glassy[73, 104-107] and semicrystalline polymer systems[108, 109]. The following sequence of events controls failure in particle toughened plastics: *i*) stress is concentrated around the inclusions due to differences in the stiffness of the particles relative to the matrix; *ii*) micro- or nano-voids formed by cavitation events that occur inside rubbery particles or at the rigid particle-matrix interface; *iii*) local yielding and matrix deformation occur via shear yielding or multiple crazing; *iv*) crack propagation is blunted by the particles.[65] Wu *et al.*[108] have shown that nylon/rubber blends with well-dispersed small particles tend to have better fracture performance than blends with larger particles due to reduced interparticle distances, which facilitates cavitation. This model has been demonstrated in other semi-crystalline blends loaded with rubbers and rigid inorganic particles, including high density polyethylene (HDPE)[106, 110] and *i*PP.[39, 111] These factors motivated us to pursue a better understanding of polyolefin mixing thermodynamics with the goal of designing *i*PP blends with controlled morphologies and enhanced toughness.

Despite the nominally simple nature of the dispersive segment-segment interactions that govern the excess mixing free energy of polyolefin blends, there is no universally accepted model that accounts for the ubiquitous thermodynamic incompatibility of saturated hydrocarbon polymers such as poly(ethylene) and poly(propylene). Nevertheless,

various theories have been advanced to account for this behavior. In the 1960's Flory generalized the equation-of-state (EOS) approach that successfully accounts for non-ideal mixing in low molecular weight compounds to polymer solutions and blends, taking into account differences in thermal expansion and compressibility.[3, 4] While capable of accounting for certain unusual features in polymer solutions (e.g., lower critical solution temperature (LCST) behavior)[5, 112], EOS theory has not found much application with high molecular polymer melts characterized by relatively small χ parameters. The polymer reference interaction site model (PRISM) developed by Schweizer *et al.*[14, 15] and lattice cluster theory (LCT) introduced by Freed *et al.*[16, 21] provide alternative theoretical approaches to capturing differences in polyolefin molecular structure. The essential concept of the PRISM approach is that structural differences (i.e. branching) and energetic asymmetries captured by coarse-grained van der Waals interactions must be carefully balanced to achieve blend miscibility. LCT accounts for the excess free energy based on a detailed statistical treatment of the local packing of structurally dissimilar repeat units. Practical application of both these theories is challenging. Graessley *et al.*[113, 114] used a traditional solubility parameter approach and argued that components with similar cohesive energy densities tend to form miscible blends. This simple and intuitive strategy was shown to be successful with roughly 75% of the saturated hydrocarbon mixtures studied, denoted "regular" blends, but failed to account for the phase behavior of the other 25% referred to as "irregular" mixtures.[115]

Bates and Fredrickson[7, 25] argued that the miscibility of polyolefin blends is controlled in part by the asymmetry in statistical segment length $b = R_g(6/N)^{1/2}$ where N is the number of repeat units defined based on a common segment volume for the components.

They speculated that the conformational rearrangements required for filling space at a constant density (i.e. constant molar volume) lead to an excess free energy of mixing with entropic origins. A study by Weimann *et al.*[27] demonstrated that poly(ethylene-*ran*-ethylethylene) (EE_E) random copolymers with roughly 70% to 90% E_E units (based on 4 carbon atoms) are melt miscible with *i*PP, which is consistent with the conformational asymmetry concept; these isomeric polymers have nearly matched *b* values and essentially identical melt densities (hence matched solubility parameters).

Guided by both the enthalpically based solubility parameter (χ_H) and entropically based conformational asymmetry parameter (χ_S) approaches we have designed a new class of saturated hydrocarbon polymers, poly(cyclohexylethylene-*ran*-ethylene) (CE) copolymers, for use in toughening isotactic polypropylene. The ideal toughening agent should be marginally immiscible with the targeted matrix material. Sufficient thermodynamic incompatibility must be imparted to result in phase separation at appropriate molecular weights. Simultaneously, the interfacial tension between coexisting phases should be kept small enough to permit the formation of small particle sizes during melt blending in order to exploit the toughening mechanisms referred to earlier. In this chapter, we demonstrate the application of these principles by adjusting χ_H and χ_S through the composition of the CE copolymers. Poly(cyclohexylethylene) (PCHE or C) and poly(ethylene) (PE or E) have the smallest and largest *b* values of all known saturated hydrocarbon polymers. Hence, the copolymer statistical segment length can be tuned to match that of virtually any other polyolefin including *i*PP. At the same time, PCHE has a melt density that is about 12 % higher than that of PE, which results in a composition dependent cohesive energy density in CE copolymers; the melt densities of PE and *i*PP are

nearly identical. Here we show that the overall $\chi = \chi_H + \chi_S$ parameter between *i*PP and CE can be adjusted to values below that associated with *i*PP and PE (mainly controlled by $\chi_S > 0$ since $\chi_H \approx 0$) by minimizing conformational asymmetry ($\chi_S \rightarrow 0$) while imparting a finite $\chi_H > 0$. This strategy produces a reduced interfacial tension leading to nanoscale particle dispersion of melt blended CE in *i*PP. The resulting blends exhibit superior tensile properties at relatively low particle loadings and optical clarity equal to or exceeding that of the neat *i*PP. The improved toughness is explained with the Wu's interparticle distance model[108] since the nano size droplets significantly reduced the interparticle distance.

3.2 Experimental

3.2.1 Materials

Commercially available *i*PP (HD915CF, Borouge, Abu Dhabi, United Arab Emirates) with a melt flow rate (MFR) of 8.0 g/10min (230 °C/2.16 kg) was used as the matrix polymer. As mentioned in Chapter 2, CE copolymers were synthesized with anionic copolymerization of styrene and butadiene followed by catalytic hydrogenation. The synthetic scheme is provided in Figure 2.1.

3.2.2 Sample preparation

As mentioned in Chapter 2, blends of the CE copolymers and *i*PP were prepared using a recirculating, conical twin-screw batch mixer (DSM Xplore, 5mL capacity) operated at 100 rpm with a barrel temperature of 180 °C. The extruded samples were dried

in a vacuum oven overnight after water cooling and then compression molded into tensile specimens with the dimensions according to ASTM D1708.

3.3 Results and discussion

3.3.1 CE random copolymers

Table 3.1 summarizes the molecular characteristics of the six polymers employed in this study including four CE copolymers and homopolymers of poly(cyclohexyl ethylene) (PCHE) and poly(ethylene) (PE). The random copolymer composition and extent of short (ethyl) branching were determined using ^{1}H NMR by integration of characteristics peaks present in the traces obtained from the parent SB copolymers. Molecular weights and dispersity were determined using room temperature SEC calibrated with THF as the mobile phase and calibrated with polystyrene standards. The representative SEC and ^{1}H NMR traces before and after hydrogenation are provided in Figure 3.1 Representative SEC (a) and ^{1}H NMR traces (b) traces of CE50 (red) and unsaturated counterpart SB50 (black). The disappearance of peaks associated with aromatic hydrogen in the NMR spectrum and an invariant SEC trace indicate complete hydrogenation without degradation.. All polymers have relatively narrow dispersity and similar molecular weights between 50 and 70 kg/mol. The glass transition temperatures and densities were measured by DSC and density gradient column experiments, respectively, where both properties rise with increasing amounts of cyclohexylethylene.

Table 3.1 Molecular characteristics of CE copolymers

Polymer	M_n[a] (kg/mol)	M_w /M_n[a]	Cyclohexyl ethylene wt.%[b]	Ethyl branches per 100 backbone carbon atoms in ethylene units[b]	T_g[c] (°C)	ρ[d] (g/cm^3)
PE	65	1.04	-	3.5	-31	0.907
CE50	49	1.05	51	3.5	-20	0.918
CE60	67	1.05	60	2.6	7	0.928
CE70	52	1.05	72	3.3	30	0.937
CE80	65	1.05	84	2.4	43	0.947
PCHE	70	1.05	100	-	144	0.960

a. Measured with SEC using the parent SB copolymer with universal calibration. The Mark-Houwink parameters for PS and PB are K_{PS} = 8.63 × 10-3 mL/g, α_{PS} = 0.736 and K_{PB} = 25.2 × 10-3 mL/g, α_{PB} = 0.727.[116] The K and α of SB copolymers are estimated using the weight-averaged values of the homopolymer counterparts.
b. Calculated from the integration of characteristic peaks in ^{1}H NMR spectra
c. Determined with DSC
d. Measured with density gradient column at 23 °C

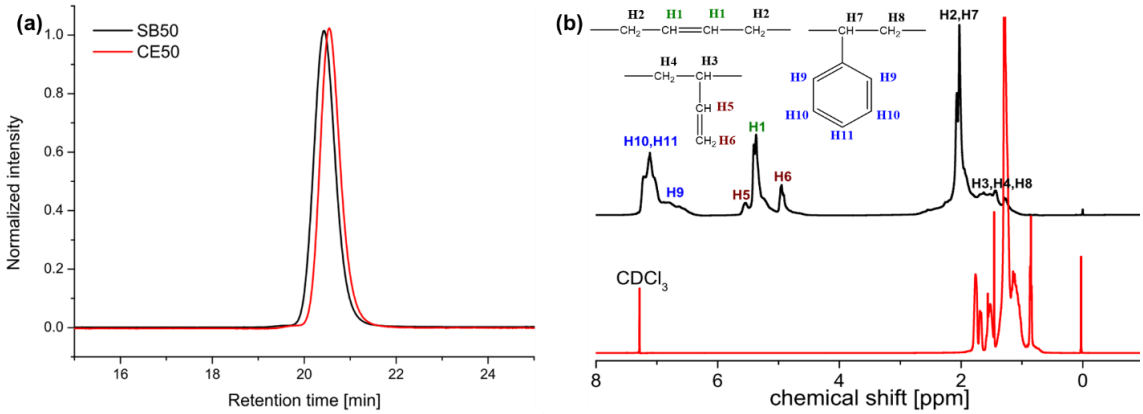

Figure 3.1 Representative SEC (a) and ^{1}H NMR traces (b) traces of CE50 (red) and unsaturated counterpart SB50 (black). The disappearance of peaks associated with aromatic hydrogen in the NMR spectrum and an invariant SEC trace indicate complete hydrogenation without degradation.

DSC traces for the CE and parent SB copolymers are shown in Figure 3.2. The single and relatively narrow glass transitions of the SB copolymers are consistent with statistically random copolymer structures.[117, 118] Aliquots were taken at various times during the polymerization of SB50 to determine the composition as a function of reaction time, demonstrating a modest degree of tapering (i.e., 21 mol% S at the beginning of the reaction and an overall 33 mol% in the final product; see Figure 3.3 (a)). Transmission electron microscopy (TEM) and small angle X-ray scattering (SAXS) experiments conducted on these polymers confirm the absence of nanoscale segregation, which indicates that the gradient in copolymer sequencing is sufficiently small to avoid any microphase separation (see Figure 3.3 (b) and (c)). Upon hydrogenation, the glass transition temperatures of the copolymers increase but remain single-valued and relatively narrow. A small endothermic peak centered at about 50 °C in CE50 and a larger endotherm in the PE DSC traces corresponds to the melting of PE crystals, reflecting about 4 % and 17 % crystallinity, respectively.

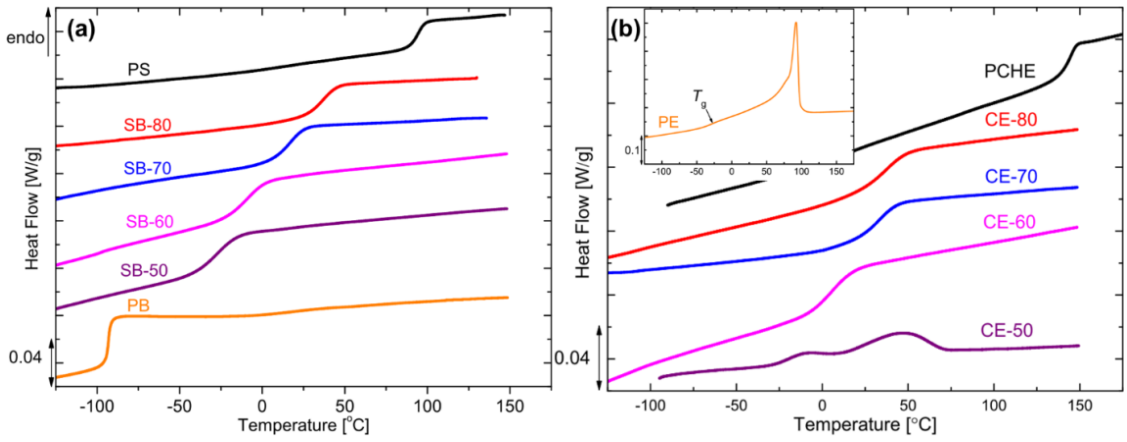

Figure 3.2 Representative DSC traces of (a) SB copolymers and (b) the corresponding CE copolymers. These results are consistent with a random copolymer molecular structure. The crystallinity in CE50 and PE (inset) are estimated to be 4% and 17 %, respectively.

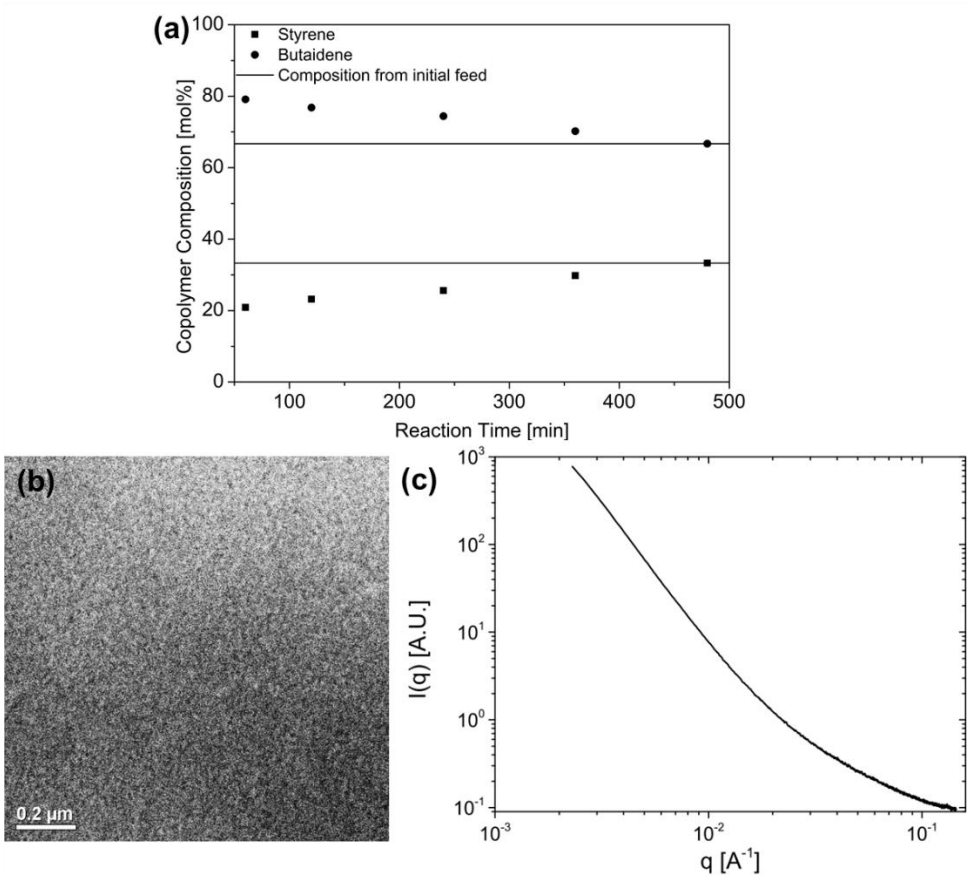

Figure 3.3 (a) SB50 copolymer composition as a function of reaction time taken at 1h, 2h, 4h, 6h and 8h of the reaction, (b) representative TEM image and (c) SAXS profile of SB50.

3.3.2 Blend morphology

Representative SEM micrographs shown in Figure 3.4 demonstrate that the 5 wt.% *i*PP/CE copolymer blends phase separate with *i*PP forming a continuous matrix and CE copolymers dispersed uniformly as droplets. Droplet sizes were determined with the aid of image analysis software (ImageJ), which provided measurements of the cross-sectional area of all the particles present in the micrographs. The area of an individual particle *i* was converted to an equivalent diameter,

$$d_i = 2\sqrt{A_i / \pi} \qquad (1)$$

In each case at least 400 particles were used to calculate the number average and volume average particle diameters,

$$d_n = \frac{\sum n_i \cdot d_i}{\sum n_i} \tag{2}$$

$$d_v = \frac{\sum n_i \cdot d_i^4}{\sum n_i \cdot d_i^3} \tag{3}$$

Average droplet sizes of all the blends were established using a log-normal distribution (see Figure 3.4 and Figure 3.5).

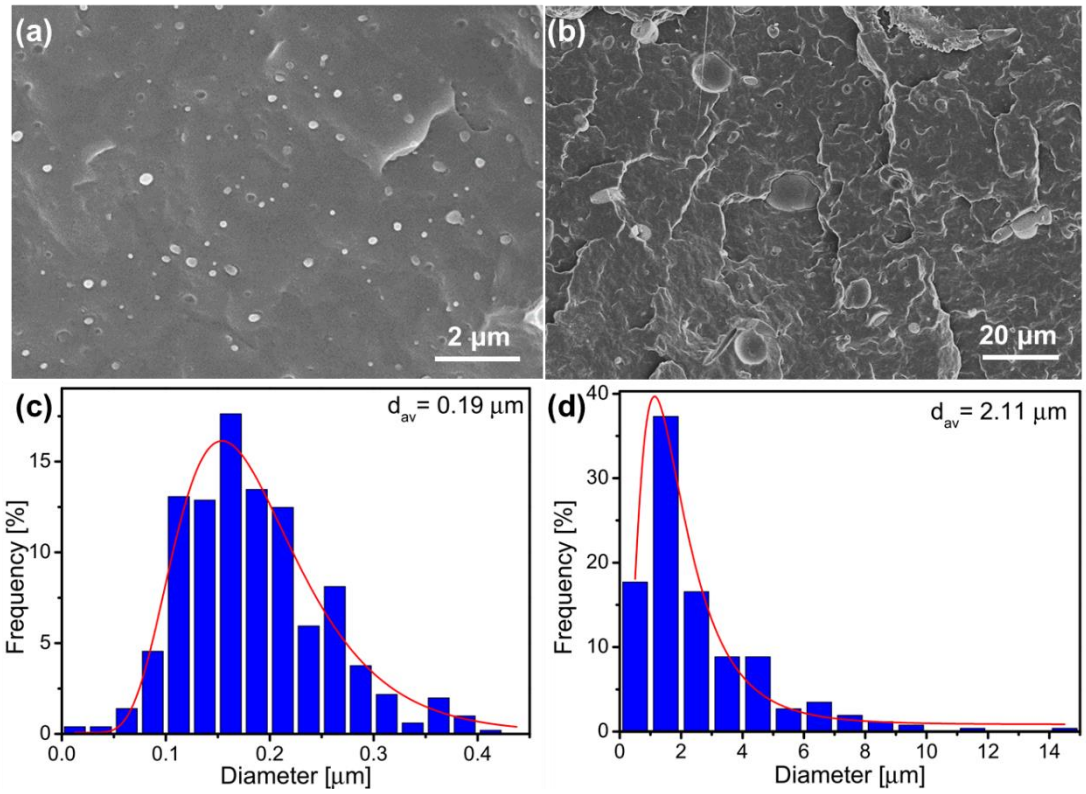

Figure 3.4 Representative SEM micrographs and the corresponding histograms of 5 wt.% loadings of (a,c) CE70 and (b,d) PCHE in *i*PP. The histograms were fit with a log-normal distribution (red curves) and the average diameters (d_{av}) are provided in the histograms.

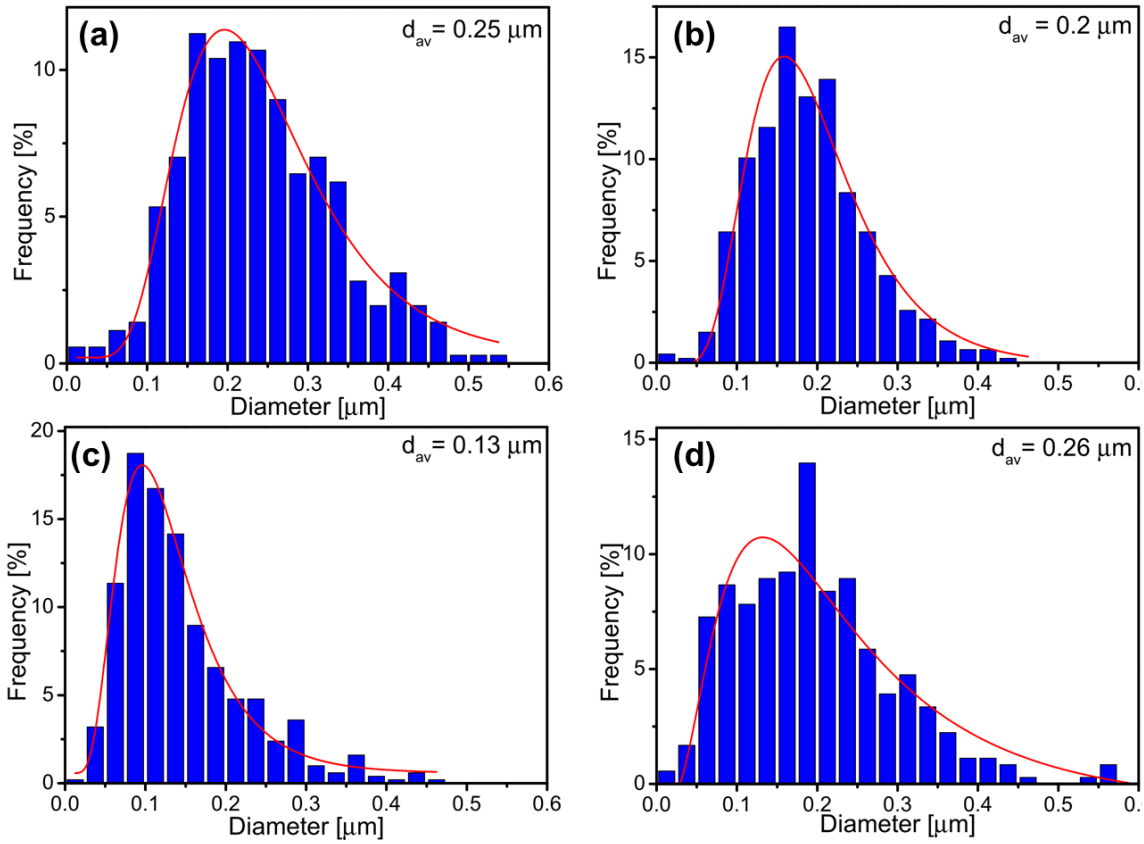

Figure 3.5 Histograms determined from SEM images of 5 wt.% loadings of (a) CE50, (b) CE60, (c) CE80 and (d) PE in *i*PP. The histograms were fitted with log-normal distribution (red solid line) and the average diameter (d_{av}) are provided in the histograms.

Results for the 5 wt.% loadings are summarized in Table 3.2 and a complete set of droplet size with various loadings is shown in Table 3.3. We note that the viscosity ratios between CE copolymers and *i*PP are much less than 1, which doesn't facilitate small droplet formation since Wu *et al.*[119] argued that droplets are smaller when the viscosity ratio between matrix and dispersed phase is closer to unity. We attribute the small droplet formation to low interfacial tension, which is discussed below. The CE copolymers and PE homopolymer are uniformly dispersed as small particles ranging in size from d_n = 0.15 to 0.24 µm while the PCHE homopolymer forms much larger droplets, d_n = 2.5 µm (See histograms in Figure 3.4 and Figure 3.5).

Table 3.2 Blend particle size and viscosity ratio

5 wt.% blends	d_n [µm][a]	d_v [µm][b]	d_v/d_n	Dispersed phase-matrix viscosity ratio η_r at 180 °C[c]
PE	0.19	0.34	1.8	0.78
CE50	0.24	0.33	1.4	0.23
CE60	0.19	0.26	1.4	0.21
CE70	0.18	0.25	1.4	0.11
CE80	0.15	0.27	1.8	0.36
PCHE	2.5	8.2	3.3	9.3

[a] Number average particle diameter. [b] volume average particle diameter.
[c] Calculated by using the viscosity determined at a shear rate of 40 s^{-1}

Table 3.3 Droplet size of *i*PP/CE copolymers blends at various loadings

Blends	CE copolymer weight percentage [%]	d_n [µm]	d_v [µm]	d_v/d_n
***i*PP/PE**	5	0.19	0.34	1.8
	10	0.34	0.69	2.0
	20	0.83	1.9	2.3
***i*PP/CE50**	5	0.24	0.33	1.4
	10	0.28	0.46	1.6
	20	0.55	1.1	2
***i*PP/CE60**	5	0.19	0.26	1.4
	10	0.3	0.5	1.7
	20	0.56	1.0	1.9
***i*PP/CE70**	5	0.18	0.25	1.4
	10	0.2	0.36	1.8
	20	0.44	1.0	2.3
***i*PP/CE80**	5	0.15	0.27	1.8
	10	0.16	0.29	1.8
	20	0.52	1.2	2.3
***i*PP/PCHE**	5	2.5	8.2	3.3
	10	4.2	18	3.9
	20	4.6	20	4.4

Droplet sizes determined for CE, PE and PCHE at loadings of 5 wt.%, 10 wt.% and 20 wt.% are presented in Figure 3.6. The CE copolymers form small droplets, ranging in size from an average diameter (d_n) of about 200 nm at 5wt.% to 500 nm at 20 wt.%. while the PCHE homopolymer forms large particles, $d_n > 2$ µm at all the loadings. At 5 wt.% and

10 wt.% loadings, the droplet sizes for the PE/*i*PP blends are comparable to those for the CE copolymers. However, at 20 wt.% loading, irregularly shaped particles with sizes approaching 1 μm in diameter were observed due to coalescence. No significant evidence of coalescence was observed in the SEM images for any of the other blends (See Figure 3.7).

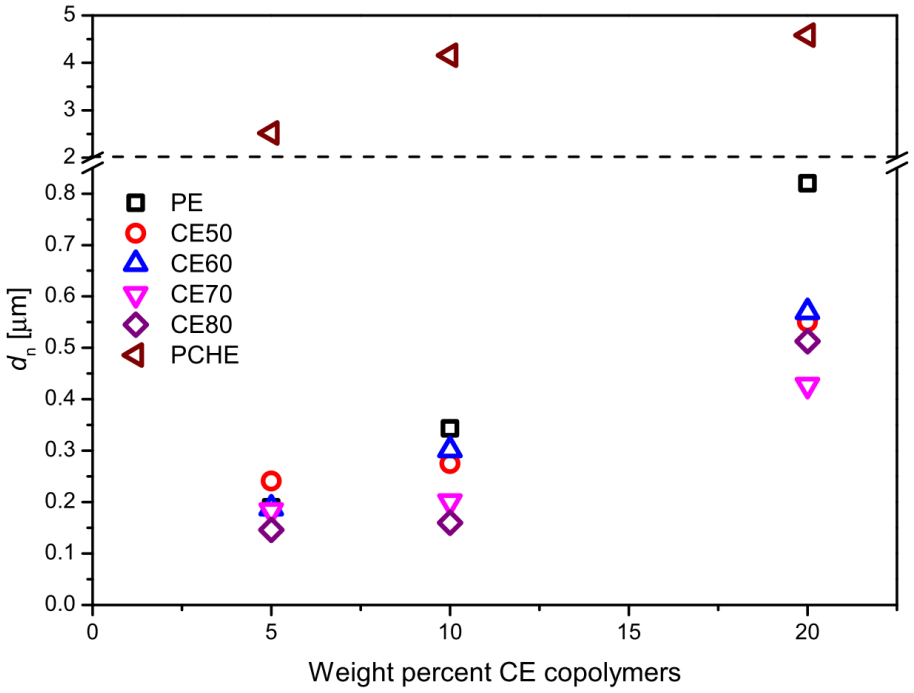

Figure 3.6 Number average diameter (d_n) of CE copolymer, PE and PCHE droplets in *i*PP matrix at different loadings. Note the break in the vertical axis.

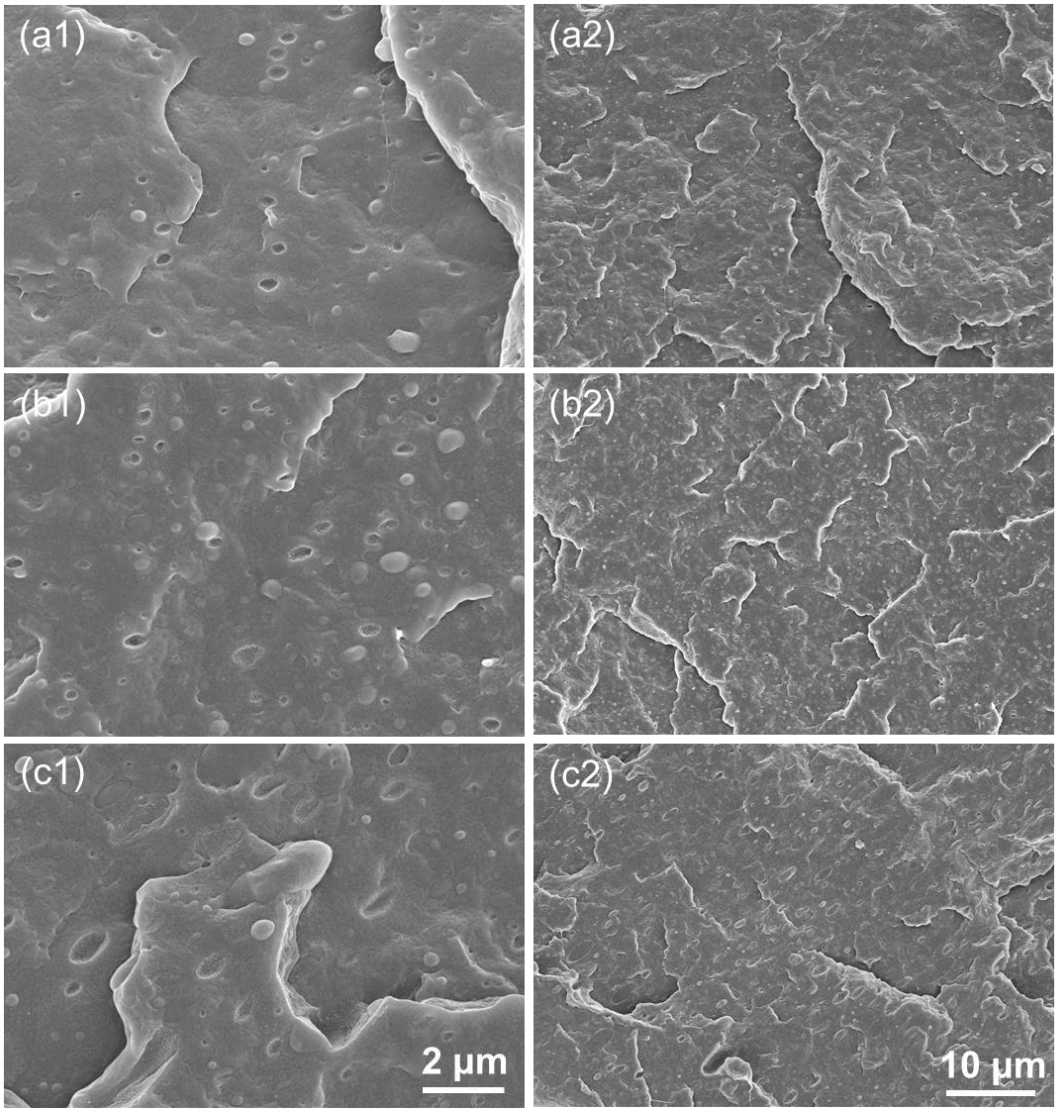

Figure 3.7 Representative SEM images of *i*PP blends containing (a1, a2) 5 wt.%, (b1, b2) 10 wt.%, (c1, c2) 20 wt.% CE50 at higher (1) and lower (2) magnification.

3.3.3 Blend mechanical properties

Representative stress-strain curves for the 2-phase blends (5 wt.% and 20 wt.%) are presented in Figure 3.8. These results fall into two categories. CE50, CE60 and CE70 are very effective in toughening the *i*PP at all concentrations where the strain at break increases from 20% for the pure *i*PP to more than 300%. At the lower concentration (5 wt.%) the yield stress and elastic modulus of these blends are comparable to those of the pure *i*PP

(See Table 3.4). At 20 wt.% loading, the CE50 and CE60 blends exhibit a somewhat depressed yield stress but with little or no consequence on the modulus, similar to what is widely reported in other rubber toughened systems;[40, 59, 107, 120] the CE70/*i*PP blends exhibit comparable mechanical properties at all loadings. Noticeable strain hardening is evident in the CE50 and CE60 blends at 20% loading probably due to stretching of the rubber particles. On the other hand, the blends with CE80 and PCHE (both glassy particles at room temperature) are at least as brittle as the pure *i*PP, while the semicrystalline PE offers a modest amount of toughening at 5 wt.% loading (≈ 100% strain at break) but little improvement at the 20 wt.% level.

Table 3.4 Mechanical properties of the *i*PP/CE copolymers blends

Blends	CE copolymer weight percentage [%]	Elastic modulus *E* [GPa]	Yield stress σ_y* [Mpa]	Elongation at break ε_b [%]
***i*PP**	0	1.68 ± 0.07	30 ± 1	14 ± 5
***i*PP/PE**	5	1.60 ± 0.04	31 ± 1	93 ± 25
	10	1.52 ± 0.03	29 ± 1	26 ± 9
	20	1.32 ± 0.10	25 ± 1	20 ± 7
***i*PP/CE50**	5	1.64 ± 0.04	27 ± 1	346 ± 60
	10	1.54 ± 0.04	25 ± 1	432 ± 51
	20	1.32 ± 0.06	20 ± 2	480 ± 47
***i*PP/CE60**	5	1.62 ± 0.05	27 ± 1	357 ± 45
	10	1.53± 0.02	26 ± 1	430 ± 49
	20	1.40 ± 0.04	22 ± 1	509 ± 47
***i*PP/CE70**	5	1.67 ± 0.06	29 ± 2	415 ± 34
	10	1.72 ± 0.12	28 ± 1	375 ± 41
	20	1.68 ± 0.07	27 ± 1	390 ± 25
***i*PP/CE80**	5	1.76 ± 0.04	31 ± 1	19 ± 5
	10	1.82 ± 0.07	30 ± 2	25 ± 7
	20	1.77 ± 0.05	-	3 ± 0.4
***i*PP/PCHE**	5	1.85 ± 0.04	28 ± 1	19 ± 5
	10	1.79 ± 0.04	20 ± 1	10 ± 2
	20	1.82 ± 0.07	-	2 ± 0.3

* Unspecified yield stress indicates that the specimen broke before yielding.

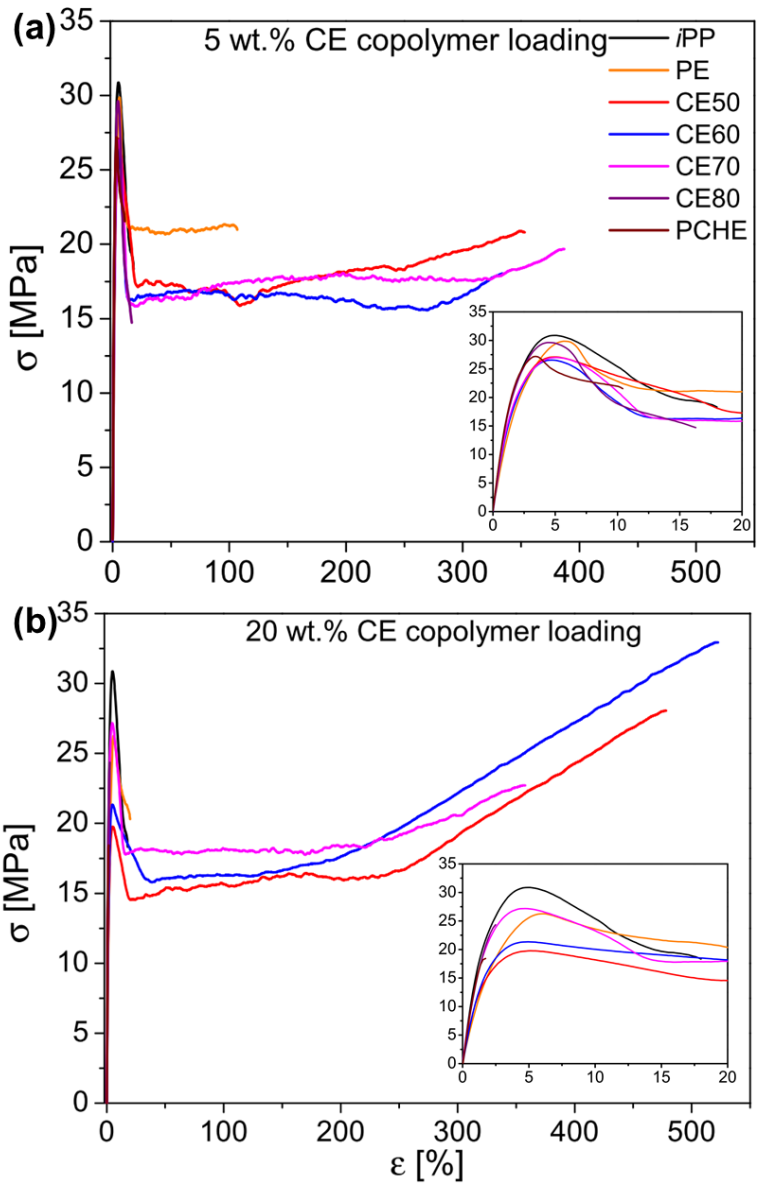

Figure 3.8 Representative stress-strain curves for (a) 5 wt.% blends and (b) 20 wt.% blends. The insets show the curves between 0 and 20 % strain.

Two key performance parameters, the tensile strength (maximum stress in the stress-strain curve, corresponding to either the yield stress or stress at break) and tensile toughness (the area under stress-strain curve prior to fracture) are plotted for all the blend materials studied as a function of loading in Figure 3.9. Table 3.4 lists the numerical values

of these parameters along with the elastic modulus, which is relatively invariant (< 20% variation) under all the conditions studied. The addition of CE50, CE60 and CE70 to *i*PP leads to significant improvements in toughness with little reduction in tensile strength, with CE70 offering the optimal balance between stiffness and strength. We note that the toughening performance of the CE copolymers may deteriorate below the glass transition temperature of the particles (See Table 3.1) although this has not been tested.

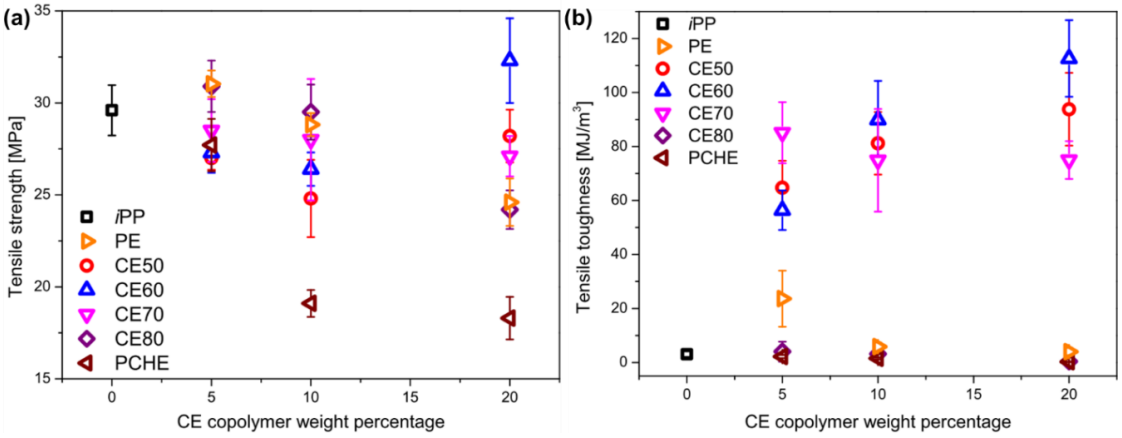

Figure 3.9 (a) Tensile strength and (b) tensile toughness as a function of loading in blends of CE copolymers, PE and PCHE homopolymers, with *i*PP. The error bars represent the standard deviations based on at least 10 specimens.

3.3.4 Blend rheology

Frequency-dependent storage (G′) and loss (G″) moduli for *i*PP, CE50, and the 20 wt.% CE50/*i*PP blend, recorded at various temperatures and time-temperature superimposed to the reference temperature 180 °C, are presented in Figure 3.10. The behavior of the pure components, *i*PP and CE50 (inset of Figure 3.10) reflect significantly different terminal relaxation times, primarily due to differences in the molecular weight and entanglement density. These differences are also evident in the CE50/*i*PP blend results,

where the liquid-like CE50 particles reduce slightly the moduli at high frequencies (see Figure 3.11 for direct comparisons). For the blend, the transition to a terminal response is shifted to lower frequencies than for the pure *i*PP due to the presence of the particles. This subtle effect is most evident in G′ as seen in Figure 3.11.

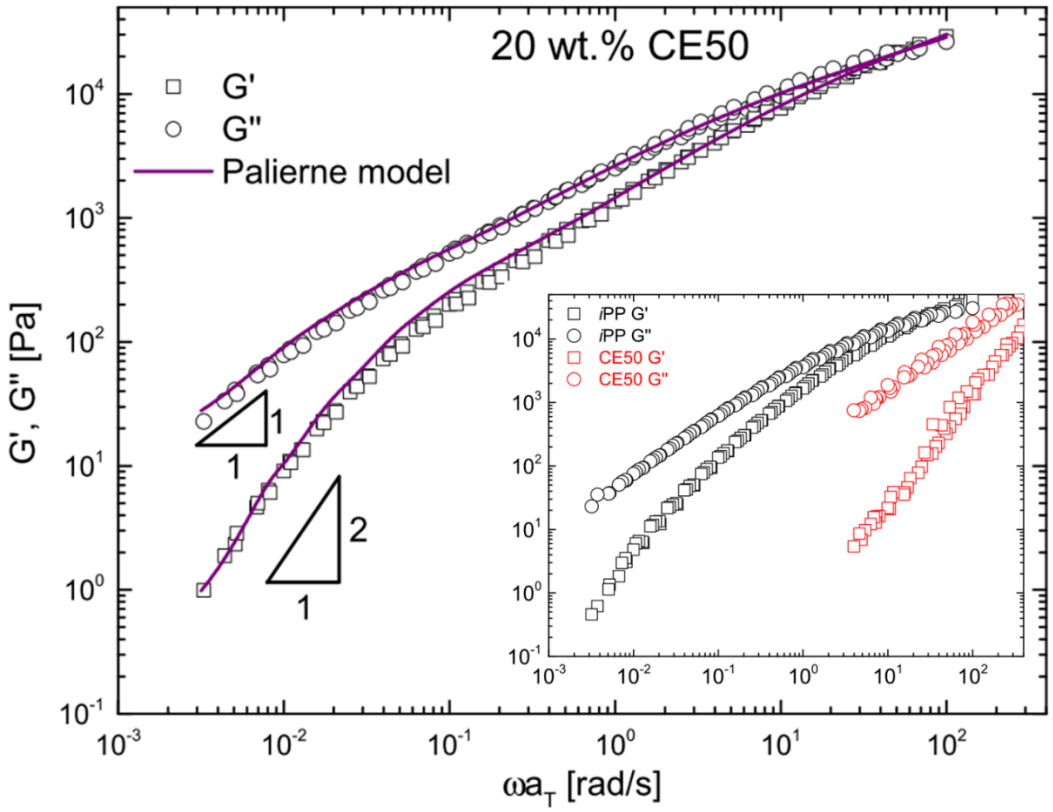

Figure 3.10 Storage and loss moduli versus frequency for the 20 wt.% CE50/*i*PP blend at 180 °C. The solid curves show the fit to the Palierne model with the interfacial tension set to 0.5 mN/m. The inset provides the storage and loss moduli versus frequency of the pure components, CE50 and *i*PP.

We have employed the Palierne model[121, 122] to interpret the rheological behavior of the blends. With knowledge of the complex moduli for the pure components, the complex shear modulus of the blend can be predicted using the interfacial tension and droplet diameter:

$$G_b^*(\omega) = G_m^*(\omega)\frac{1+3\sum_i \phi_i H_i(\omega)}{1-2\sum_i \phi_i H_i(\omega)}$$

$$H_i(\omega) = \frac{(G_d^*(\omega)-G_m^*(\omega))(19G_d^*(\omega)+16G_m^*(\omega))+8\Gamma/d_i(5G_d^*(\omega)+2G_m^*(\omega))}{(2G_d^*(\omega)+3G_m^*(\omega))(19G_d^*(\omega)+16G_m^*(\omega))+80\Gamma/d_i(G_d^*(\omega)+G_m^*(\omega))} \quad (4)$$

where $G_d^*(\omega)$, $G_m^*(\omega)$ and $G_b^*(\omega)$ are the complex moduli of the dispersed phase, matrix and blend at frequency ω, respectively. Γ is the interfacial tension between the coexisting phases, and ϕ_i is the volume fraction of the droplet with diameter of d_i. Following Graebling *et al.*[122] and Bousmina *et al.*[123], we employ the Palierne model using the volume average diameter d_v and volume fraction of the dispersed phase ϕ; this simplified approach has been shown to be valid provided d_v/d_n is ≤ 2.3 (see Table 3.2). The best fit of the simplified Palierne model to the 20 wt.% CE50/*i*PP blend (d_v = 1.1 μm, d_v/d_n = 2.0, see Table 3.3) is shown by the solid curves in Figure 3.10, where the interfacial tension Γ = 0.5 mN/m was the only fitting parameter. The sensitivity of the theoretical moduli to variations in Γ is illustrated in Figure 3.11 and the values extracted for all the blends are listed in Table 3.5. The rheological behavior of the blends is sufficiently sensitive to the interfacial tension between the particles and matrix polymer to provide meaningful estimates of this parameter for the *i*PP/CE and *i*PP/PE blends. Owing to the dominant role of $H(\omega)$ in Equation 4 and the reduced moduli and relatively large size of the PCHE particles (see inset of Figure 3.10), we were not able to estimate the interfacial tension between *i*PP and PCHE using this approach.

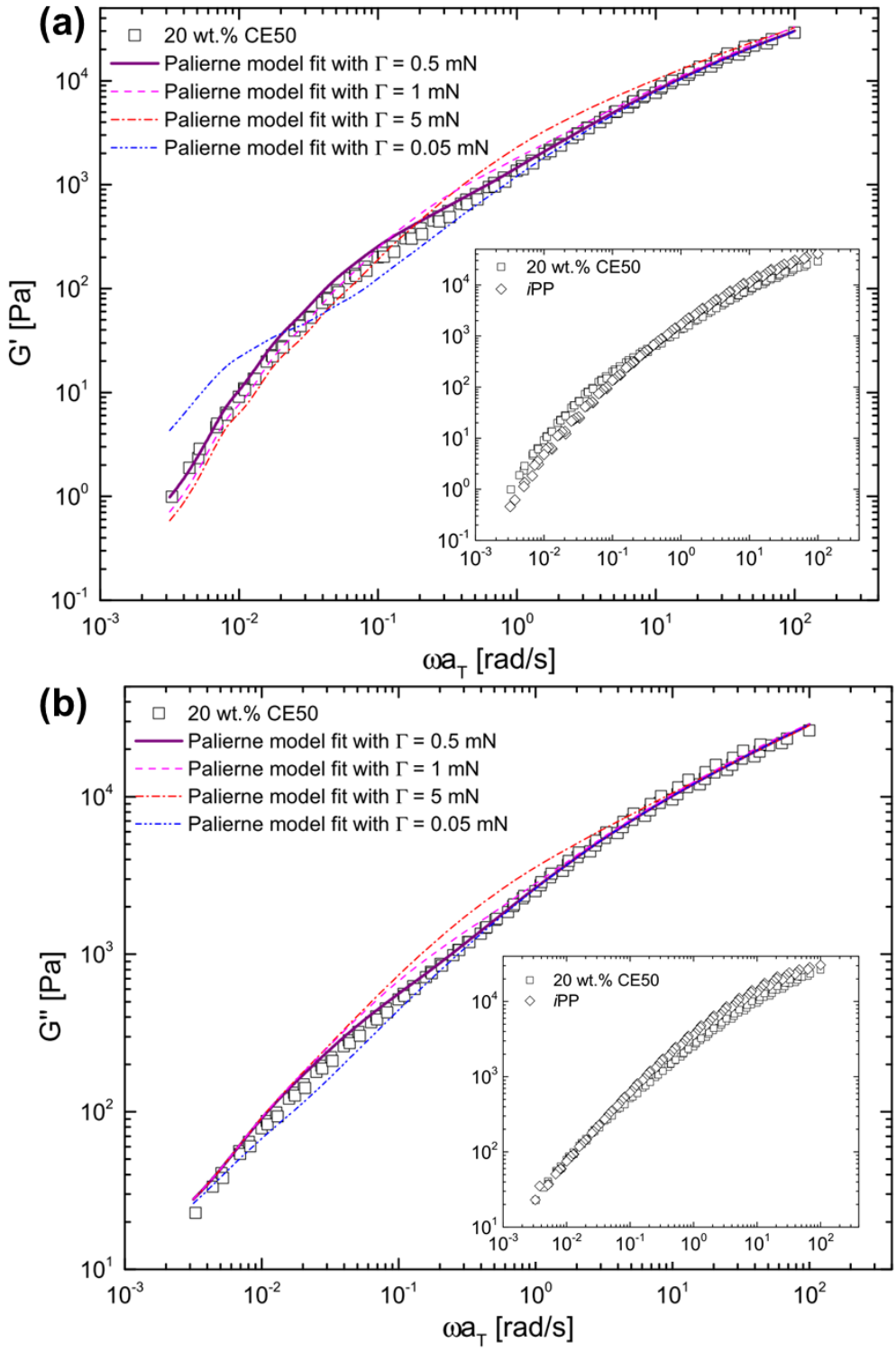

Figure 3.11 Comparison of the Palierne model predictions with experimental data for 20 wt.% CE50/*i*PP blends at 180 °C using different interfacial tensions; (a) storage modulus, (b) loss modulus. The insets show the storage and loss moduli of 20 wt.% CE50/*i*PP blends and *i*PP.

We also estimated the interfacial tensions using Wu's equation,[119]

$$d_n = \frac{4\Gamma\eta_r^{\pm 0.84}}{\dot{\gamma}\eta_m} \quad (5)$$

where η_r is the viscosity ratio, $\dot{\gamma}$ is the shear rate, η_m is the matrix viscosity; the minus (plus) sign signifies $\eta_r < 1$ (> 1). These calculations, summarized in Table 3.5, where made using the averages of the diameters d_n determined at 10 wt.% and 20 wt.% loadings, in order to be consistent with the 15 wt% condition associated with the derivation of equation 5. Both Palierne's and Wu's methods, yield reasonably consistent estimates of Γ. The interfacial tensions for PE, CE50, CE60, CE70 and CE80 with *i*PP are substantially smaller than that for PCHE, consistent with the formation of the smaller droplets as summarized in Figure 3.6.

Table 3.5 Estimation of interfacial tension with *i*PP at 180 °C using Palierne model and Wu's equation

Polymer	Fitting parameter Γ/d_v [Pa]	d_v [μm]	Interfacial tension Γ [mN/m]	Γ using Wu's equation
PE	660	1.94	1.28	1.82-4.44
CE50	450	1.10	0.50	0.7-1.3
CE60	425	1.04	0.44	0.7-1.2
CE70	335	1.00	0.34	0.3-0.6
CE80	380	1.18	0.45	0.6-1.7
PCHE	-	20.1	-	5.6-5.8

3.3.5 Blend transparency

Along with producing improved mechanical properties, the CE copolymers also provide equivalent or greater transparency to the blends than is found in the unmodified semicrystalline *i*PP material, which is significant for applications in the packaging business.

The 20 wt.% blends and pure *i*PP were pressed into 0.9 mm thick discs and transparencies were measured using 570.8 nm wavelength light. Figure 3.12 shows the measured light transmission values normalized with respect to pure *i*PP. Within experimental error the transparency of the CE modified *i*PP specimens is unaffected, or even slightly improved, by the presence of the toughening agents. However, adding PE and PCHE leads to significant deterioration of the transparency due to the scattering of light caused by the semi-crystalline nature of PE and the large size and higher density of the PCHE droplets, respectively.

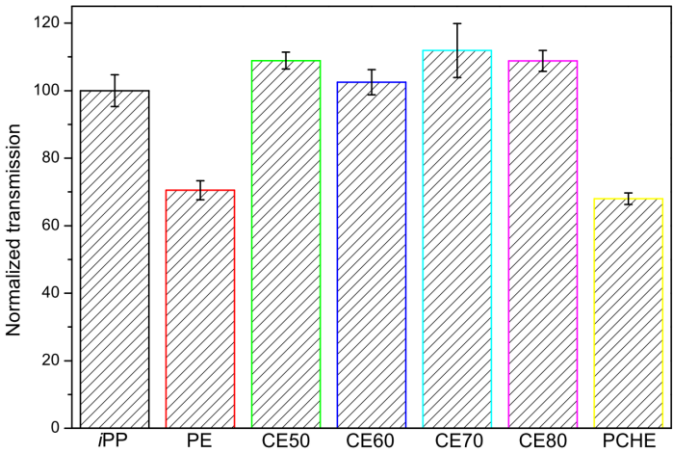

Figure 3.12 Normalized transmission at 570.8 nm of 0.9 mm thick specimens for 20 wt.% PE, PCHE and CE/*i*PP blends with respect to pure *i*PP. Error bars represent standard deviation based on 5 measurements.

So-called contact transparency experiments, performed by placing the disc on a texted background (See Figure 3.13) reveal that the PCHE/*i*PP blends are noticeably blurrier than the CE/*i*PP blends, consistent with the light transmission results. We attribute these optical results to a combination of three factors. Firstly, the particle sizes are significantly smaller than the wavelength of light, minimizing form factor scattering.

Secondly, the mechanically most effective CE copolymers (CE50, CE60 and CE70) have a density that is close to that of *i*PP at room temperature (see Table 3.1), leading to near contrast matching of the refractive index between the particles and the matrix. Thirdly, the incorporation of amorphous CE copolymers reduces the volume fraction of crystalline materials in the blends, which leads to less scattering from the crystal spherulites.

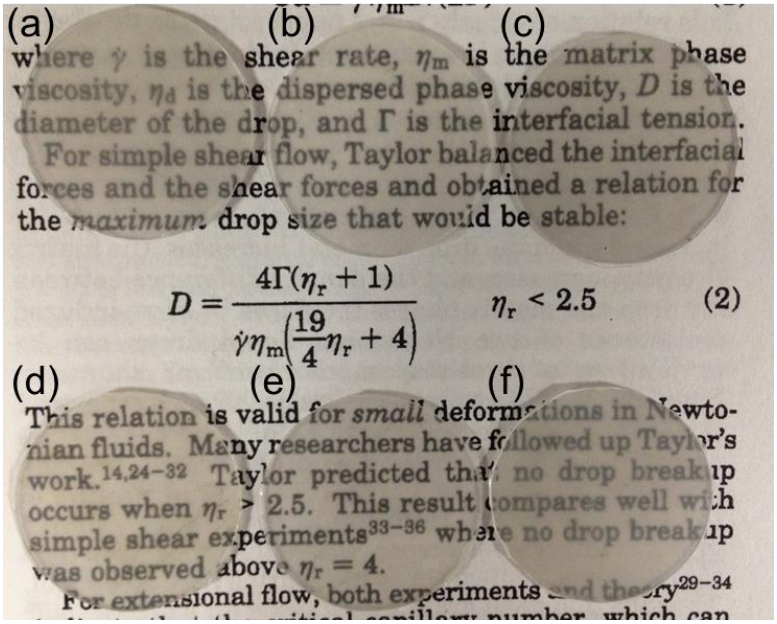

Figure 3.13 Transparency of 0.9 mm thick discs of (a) pure *i*PP, and 20 wt.% CE copolymers/*i*PP blends of (b) CE50, (c) CE60, (d) CE70, (e) CE80, and (f) PCHE.

3.4 Discussion

The original motivation for this study was to explore the possibility of developing *i*PP miscible polymers using random copolymers formed from cyclohexylethylene (C) and ethylene (E) repeat units based on statistical segment length asymmetry theory.[6, 7] In the course of blending the CE compounds with *i*PP, we came to realize that both the average

statistical segment length, b, and the density, ρ, of these random copolymers are impacted by the composition. Because saturated hydrocarbon polymers (polyolefins) interact through simple dispersion interactions, we propose that to a first approximation these two effects can be treated separately,

$$\chi = \chi_H + \chi_S \tag{6}$$

where χ_H accounts for the van der Waals interactions and χ_S scales with the magnitude of the conformational asymmetry. The statistical segment lengths of CE copolymers (b_{CE}) are estimated using the published b values of PCHE and PE homopolymers (b_C = 4.6 Å and b_E = 8.0 Å[29, 124]) weighted by the associated volume fraction ϕ_C, $b_{CE}^2 = \phi_C \cdot b_C^2 + (1-\phi_C) \cdot b_E^2$ as listed in Table 3.6. Matching with b_{iPP} = 5.6 ± 0.2Å,[27] which minimizes χ_S, occurs between CE70 and CE80. We note that all the b values correspond to a reference volume of 119.6 Å^3 at 180 °C, approximately a four-carbon repeat unit.

The enthalpic part of χ can be estimated using the solubility parameter approach based on group contribution schemes for estimating δ,[125]

$$\chi_H = \frac{V_{ref}}{kT}(\delta_1 - \delta_2)^2$$

$$\delta_i = \frac{F}{V_i} \tag{7}$$

where V_{ref} is the reference volume (119.6 Å^3 at 180 °C), k is the Boltzmann constant, F is the molar attraction constant, and δ_i and V_i are the solubility parameter and molar volume of pure components. We have estimated the group contributions to F using the method of Van Krevelen *et al.*[125] where the repeat unit molar mass has been determined based on the polymer densities. The densities of the CE copolymers measured at 23 °C (Table 3.1) were scaled to 180 °C using the empirical thermal expansion coefficient $\alpha T_g \approx 0.16$[126]. The

densities of PE and PCHE are 0.784 g/cm^3 at 140 °C and 0.900 g/cm^3 at 180 °C as reported by Fetters *et al.*[127] and Krishnamoorti *et al.*[124], respectively.

Alternatively, the overall χ parameters for *i*PP and the CE copolymers can be calculated from the estimated interfacial tension as shown by Helfand *et al.*,[128, 129]

$$\Gamma = \frac{kT}{b^2}\left(\frac{\chi}{6}\right)^{0.5} \tag{8}$$

where b is the statistical segment length; we have used the geometric mean $b = (b_i b_j)^{1/2}$ of the two components for these calculations. The χ values obtained using the solubility parameter (equation 7) and interfacial tension (equation 8) approaches are summarized in Table 3.6. All these values anticipate phase separation between PE, PCHE and the CE copolymers with *i*PP based on Flory-Huggins theory ($\chi N > 2$) at the melt blending temperature since $N > 10^3$ in all cases.

Table 3.6 The χ parameters of CE copolymers and *i*PP calculated from interfacial tensions and solubility parameters

Polymer	b [Å]	χ at 180 °C [×10^{-3}]	
		Γ approach	δ approach
PE[a]	7.7	46.7	0.77
CE50	6.7	5.40	1.29
CE60	6.4	3.15	2.63
CE70	5.9	1.93	6.23
CE80	5.4	2.84	7.86
PCHE	4.6	473	35.5

a. PE in this study is composed of 13% ethylethylene and 87% ethylene units.

Qualitative differences between the χ values estimated with the two approaches for the limiting cases of PE/*i*PP and PCHE/*i*PP blends can be attributed to the relative importance of χ_S and χ_H. The solubility parameter approach does not include the effects of

conformational asymmetry, which dominates the overall value of χ in PE/*i*PP; these isomeric components have nearly identical melt density resulting in a small χ_H. Conversely, a rather large (> 10%) density difference between PCHE and *i*PP at 180 °C makes χ_H a non-negligible factor in PCHE/*i*PP. Both limiting cases have non-trivial contributions from χ_S (see Table 3.6) based on conformational asymmetry theory.[7]

At intermediate CE compositions, particularly CE70 and CE80, χ_S is minimized due to the matching of the statistical segment length with *i*PP, hence χ_H emerges as the dominant term in χ primarily due to the density mismatch. This reflects a special feature associated using the C repeat units: PCHE has an unusually large melt density, resulting in a large group contribution to δ relative to other saturated hydrocarbon polymers. Independent control over these two factors, χ_H and χ_S, affords a unique ability to manipulate the interfacial tension and consequently particle size at tractable molecular weights resulting in optimized toughening agents.

We have attributed the enhanced toughness evidenced in Figure 3.8 to the uniformly dispersed small particles in the *i*PP matrix. The possible influences of changes in the crystal form or the extent of crystallinity caused by the CE copolymers, significant factors in other studies,[130, 131] have been ruled out based on DSC results (See Figure 3.14 and Table 3.7).

Table 3.7 Crystallization behavior of *i*PP and *i*PP/CE blends

Blends	CE copolymer weight percentage [%]	The onset crystallization temperature T_{on}[a] [°C]	The peak crystallization temperature T_{peak} [°C]	Crystallinity[b] X_c [%]
***i*PP**	0	129.6	128.8	52
***i*PP/PE**	5	129.2	127.4	53
	10	129.1	127.1	53
	20	129.0	126.8	53
***i*PP/CE50**	5	128.3	126.9	48
	10	128.8	126.9	52
	20	129.0	126.4	51
***i*PP/CE60**	5	128.4	126.6	49
	10	128.1	126.6	51
	20	127.8	124.7	50
***i*PP/CE70**	5	128.1	126.4	49
	10	127.3	125.1	52
	20	126.9	124.4	51
***i*PP/CE80**	5	127.7	126.0	46
	10	127.4	124.8	55
	20	127.0	124.2	52
***i*PP/PCHE**	5	129.0	127.2	51
	10	128.8	127.1	50
	20	128.0	126.1	53

a. T_{on} is defined as the temperature as the intercept of the tangents at the baseline and the high temperature side of the exotherm.

b. Crystallinity is calculated using $X_c = \frac{\Delta H_{melt}}{\omega \cdot \Delta H_{fusion}}$ where ΔH_{melt} is the measured enthalpy of melting, ω is the weight fraction of *i*PP in the blend and ΔH_{fusion} = 207 J/g is the heat of fusion for pure crystalline *i*PP.

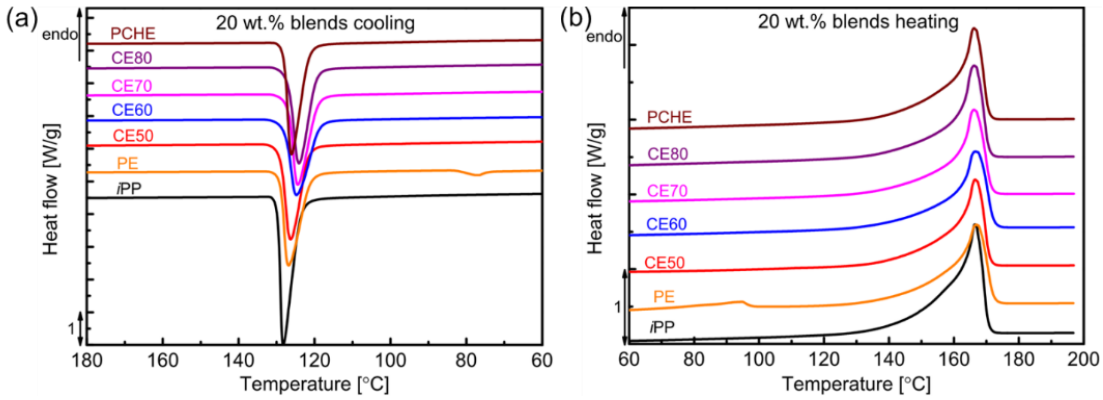

Figure 3.14 DSC traces of 20wt.% *i*PP/CE copolymers blends and pure *i*PP obtained while (a) cooling from 200 °C at a rate of 10 °C/min, and (b) heating at 10 °C/min following the cooling cycle. Curves were shifted vertically for clarity.

SEM images obtained from 5 wt.% CE60/*i*PP blend specimens deformed up to the yield point (see Figure 3.15a) reveal cavities due to rupture of the rubber particles and/or debonding at the particle/matrix interface. Parallel shear bands oriented 45 degrees relative to the tensile direction appeared immediately upon yielding and remain after specimen failure (See Figure 3.16). An SEM micrograph shown in Figure 3.15b reveals large cavities and fibrous structures along the tensile direction providing further evidence of shear yielding of the matrix. Cavitation induced shear yielding is identified as the most probable toughening mechanism in these nanostructured blend materials, similar to what has been reported in other rubber toughening systems[73, 104-107]. Consistent with this proposed mechanism, glassy CE80 and PCHE, and semi-crystalline PE, which are less prone to cavitation, do not perform like the CE50, CE60 and CE 70 (Figure 3.8).

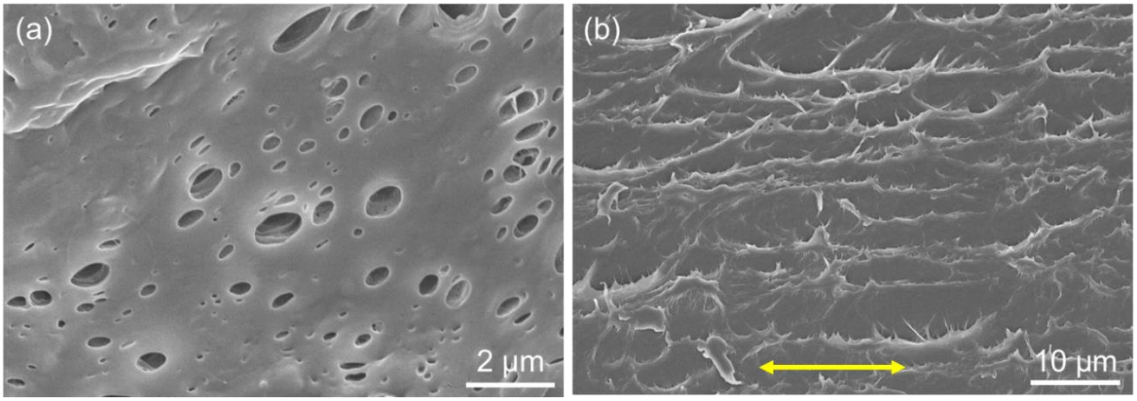

Figure 3.15 Representative SEM images of 5 wt.% CE60/*i*PP blends surfaces: (a) at yield point perpendicular to the tensile direction; (b) after failure along the tensile direction. The yellow arrow identifies the tensile direction. Larger cavities and fibrous structures of the matrix can be observed in (b) due to shear yielding.

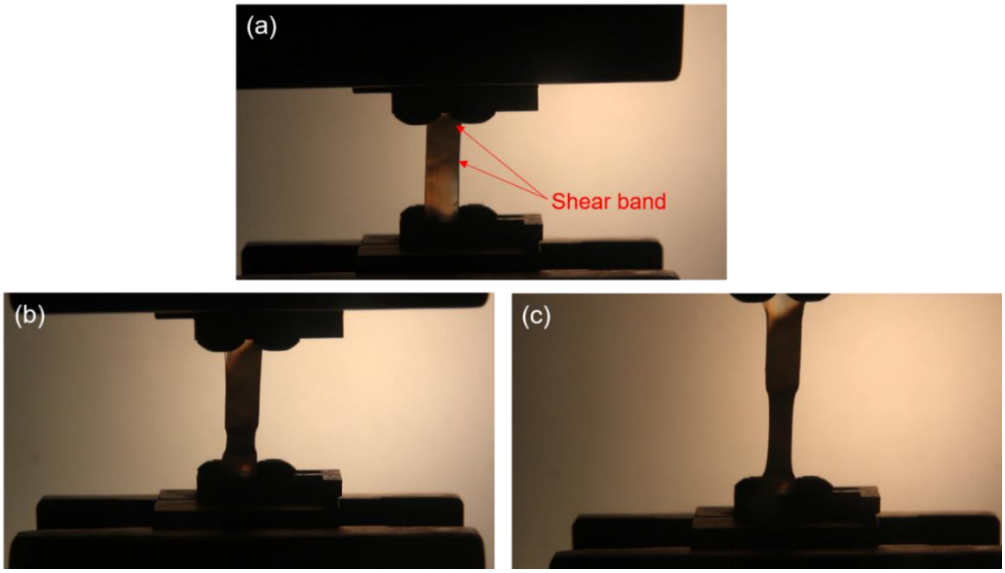

Figure 3.16 Representative images of three dumbbell shape specimens containing 5 wt.% CE50 taken between polarizers at (a) the yield point, (b) 20% strain, and (c) 50% strain. The red arrows denote the formation of shear bands right after the yield point.

The efficiency of the CE copolymers appears to be enhanced by the uniformly dispersed small droplets in the *i*PP matrix. The percolation model proposed by Wu *at al.*[108, 109] establishes a criterion for rubber toughening with regards to the interparticle distance *l*,

$$l = d\left[\left(\frac{\pi}{6V_r}\right)^{1/3} - 1\right] \quad (9)$$

where d is the number average diameter of rubber particles and V_r is the volume fraction of rubber. When l is below a critical value l_c, which depends on the properties of the matrix, toughness enhancement can be achieved.[39, 111] The interparticle distances for the CE copolymers at all loadings studied are relatively close to or smaller than 0.2 μm[39, 111, 132] which is the critical value for *i*PP at room temperature (See Table 3.8).

Table 3.8 The interparticle distance l of CE copolymer/*i*PP blends with different compositions

Blends	CE copolymer volume fraction φ	Average diameter d_n [μm]	Interparticle distance l [μm]
***i*PP/PE**	5.0	0.19	0.23
	10	0.34	0.25
	20	0.83	0.31
***i*PP/CE50**	5.0	0.24	0.29
	9.9	0.28	0.21
	20	0.55	0.20
***i*PP/CE60**	4.9	0.19	0.23
	9.8	0.30	0.22
	20	0.56	0.22
***i*PP/CE70**	4.9	0.18	0.22
	9.7	0.20	0.15
	20	0.44	0.17
***i*PP/CE80**	4.8	0.15	0.17
	9.6	0.16	0.12
	19	0.52	0.20
***i*PP/PCHE**	4.8	2.5	3.1
	9.5	4.2	3.2
	19	4.6	1.7

3.5 Conclusions

We have utilized the conformational asymmetry concepts to design a new class of polyolefin copolymers (CE) with 50-80 wt.% cyclohexylethylene units by anionic random copolymerization of styrene and butadiene followed by catalytic hydrogenation. Melt mixed blends of *i*PP and CE copolymers with uniformly dispersed sub-micron size droplets, as small as 200 nm in diameter at 5 wt.% loading, exhibit superior tensile properties, owing to enhanced shear yielding of the matrix induced by particle cavitation. Control over the phase-separated morphology is attributed to the reduced interfacial tension between the CE copolymer and *i*PP matrix as revealed by blend rheological measurements. This work demonstrates a practical approach to preparing polypropylene blends with controlled particle sizes and improved mechanical and desirable optical properties by tuning the entropic (χ_S) and enthalpic (χ_H) contributions to the overall segment-segment interaction parameter based on statistical segment length and density mismatches, respectively.

4. Chapter 4: Toughen isotactic polypropylene (*i*PP) with rubbery PEP-PEE$_E$ block copolymer micelles*

4.1 Introduction

This chapter presents the successful application of 'amphiphilic' block copolymer (BCP) micelles towards the goal of toughening semicrystalline isotactic poly(propylene) (*i*PP). Strategically designed BCPs comprised of *i*PP-miscible and *i*PP-immiscible blocks where developed with the guidance of concepts that describe polyolefin mixing thermodynamics. This work has opened new avenues to brittle thermoplastic toughening and provided valuable insights on the toughening mechanism.

The importance of *i*PP cannot be overemphasized. This plastic has become an indispensable product, found everywhere from common packaging and textile products to components in cutting-edge automobiles and aircraft (e.g., the Tesla and Boeing Dreamliner) due to its excellent processability and low cost. However, brittleness at high strain rates and low temperatures hinders some applications as a high-performance engineering plastic. Extensive research has been conducted to develop blends with improved toughness via incorporation of rigid particles[41, 44, 46], rubbers[40, 107, 133, 134] and

* Reproduced in part with permission from (Xu, J.; Howard, M. J.; Mittal, V.; Bates, F. S. "Block Copolymer Micelle Toughened Isotactic Polypropylene", *Macromolecules,* American Chemical Society)

hybrid core-shell structures[49, 102]. Among all these studies rubbers are recognized as the most effective toughening agents, more so than rigid particles. Nevertheless, high rubber contents (> 20 wt%) are generally required to obtain adequate toughness, significantly reducing the modulus and strength of the *i*PP material. Highly effective toughness modifiers that offer sufficient toughness at low contents are in great demand.

We begin this chapter with a brief review of well-accepted concepts regarding the toughening of plastics. Cavitation of rubber particles, observed by electron microscopy, has been recognized for many years as a significant phenomenon in various rubber toughened thermosets[68, 70, 71] and thermoplastics[74, 133]. A state of triaxial stress in the hard plastic (e.g. generated under plane strain at the tip of a sharp crack) leads to dilation of the soft rubber particles, resulting in fracture of the bulk rubber or debonding at the particle-matrix interface, which relieves the volume strain imposed by the surrounding matrix. This promotes extensive shear yielding and/or multiple crazing leading to improved toughness. Bucknall *et al.*[54, 55, 62] evaluated the cavitation process from a thermodynamic perspective by balancing the strain energy release and energy of newly formed surfaces in rubber modified nylon blends. They found that small particles (diameter << 100 nm) are unable to cavitate because the energy penalty for forming the void surface is larger than the associated release of strain energy. They also demonstrated that cavitated particles can reduce the stress levels required for matrix shear yielding based on a classical yield criteria analysis. On the other hand, they argue that the material tends to deform by crazing when the particles are too large, resulting in unstable crack growth and early failure. Bucknall and Paul concluded that there is an optimal range of particle diameter for toughening, which is 0.2-0.4 μm for nylon blends.[57, 58]

The particle sizes in current rubber toughened *i*PP blends are generally in the range 0.5-5 μm depending on the rubber content and processing conditions, usually with a large portion of particles having a diameter larger than 1 μm.[52, 135, 136] We aim to utilize block copolymers (BCPs) that can self-assemble into relatively uniformly sized nano-scale micelle structures [75], which have been shown to be effective in toughening epoxy [66, 67, 71] and recently extended to glassy polylactide (PLA)[74]. 'Amphiphilic' block copolymers with both *i*PP-philic (i.e., *i*PP-miscible) and *i*PP-phobic (i.e., *i*PP-immiscible) blocks need to be strategically designed for this purpose, requiring a consideration of polyolefin mixing thermodynamics.

We have reviewed progress in understanding polyolefin blend mixing thermodynamics in Chapter 1. The most relevant one is the conformational asymmetry theory established by Bates and Fredrickson in the 1990s.[6, 7] Consistent with their theory, it was found that random copolymers referred to as PEE_E containing 70 to 90% ethyl ethylene (E_E) and 10 to 30% ethylene (E) repeat units are melt-miscible with *i*PP due to closely matched *b* values and similar densities in the melt state as shown by Weimann *et al.*[27]. Motivated by these results, we designed a series of diblock copolymers each containing a PEE_E block with around 73% E_E units and a poly(ethylene-*alt*-propylene) (PEP) block to explore the possibility of micelle-based toughening of *i*PP. These compounds were obtained by hydrogenation of anionically polymerized poly(1,4-isoprene)-*b*-poly(1,2/1,4-butadiene) (PI-PB). PEP was employed as the *i*PP-phobic block because of the similar chemical structure to ethylene-propylene (EPR) rubber, which is widely used in toughening *i*PP. In this work, we demonstrate that blends with well-dispersed BCP micelles of around 100 nm in diameter can be prepared by properly tuning

the molecular weight of the BCP. Furthermore, these micelles are shown to be very effective toughening agents, leading to superior tensile properties with concentrations as low as 1 wt% and greatly improved impact strength, exceeding 10 times that of the pure *i*PP with 10 wt% BCP. Blend toughness is attributable to cavitation induced matrix shear yielding and multiple-crazing. Blends of *i*PP and PEP homopolymer also have been prepared, resulting in larger particle sizes (≈ 0.5 μm) characterized by more marginal improvement in tensile and impact toughness. A review of established cavitation, shear yielding and crazing criteria shed light on the design of tough *i*PP blends with an emphasis on the rubber particle size and associated effects on the matrix plastic deformation.

4.2 Experimental

4.2.1 Materials

A commercially available *i*PP (HD915CF) with a melt flow rate (MFR) of 8.0 g/10min (230 °C/2.16 kg) was provided by Borouge (Abu Dhabi, United Arab Emirates) and used as received. The number-average and weight-average molecular weights are 28 and 211 kg/mol, respectively, based on high-temperature SEC measurements using universal calibration with PE standards (see Figure 4.1). As mentioned, the PEP-PEEE block copolymers were synthesized by sequential anionic polymerization of isoprene and butadiene followed by catalytic hydrogenation. The synthetic scheme is provided in Figure 2.2. The block copolymers were characterized using SEC, ^{1}H NMR, DSC and rheology as described in Chapter 2.

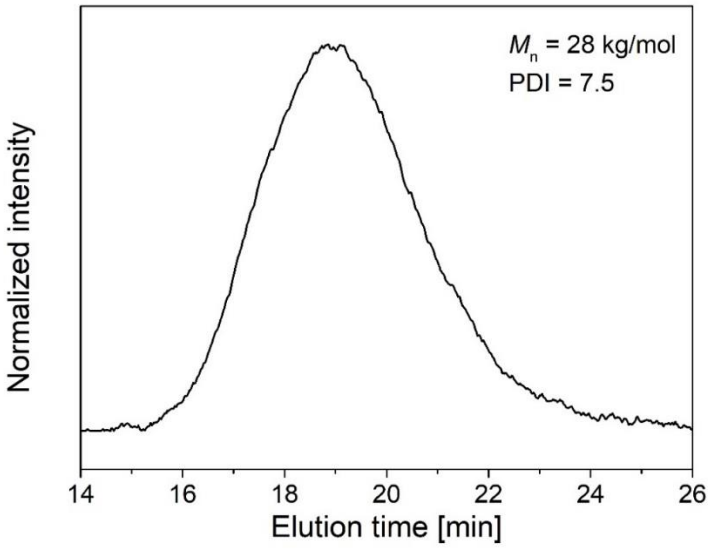

Figure 4.1 High temperature SEC trace of *i*PP HD915CF. Molecular weights (M_n and M_w) and polydispersity (PDI) were determined by size exclusion chromatography (SEC) with a 2 mg/mL 1,2,4-trichlorobenzene (TCB) solution at 150 °C using an Agilent PL-220 equipped with a RI detector. The column set (three Agilent PL-Gel Mixed B columns and one PL-Gel Mixed B guard column) was operated with 1,2,4-trichlorobenzene (TCB) containing 0.01 wt% 3,5-di-tert-butyl-4-hydroxytoluene (BHT) at 1.0 mL/min at 150 °C. Data were evaluated using a polyethylene calibration curve (Varian and Polymer Standards Service).

4.2.2 Sample preparation and mechanical testing

As described in Chapter 2, blends of *i*PP and PEP-PEE$_E$ diblock copolymers for tensile testing were prepared using a recirculating DSM Xplore twin screw micro-compounder. Larger batches of blends for Izod impact testing were prepared with a 16-mm twin-screw extruder followed by water cooling, air drying and pelletizing. The tensile testing and Izod impact testing specimens were compression and injection molded according to ASTM D1708 and D256.

4.3 Results

4.3.1 PEP-PEE$_E$ diblock copolymer

The molecular characteristics of the five polymers used in this study including three symmetric PEP-PEE$_E$ diblock copolymers, and PEP and PEE$_E$ homopolymers are summarized in Table 4.1.

Table 4.1 Molecular Characteristics

Polymer	[a] $M_{n,PEP}$ [kDa]	[a] $Đ_{PEP}$	[b] $M_{n,total}$ [kDa]	[c] $Đ_{total}$	[d] f_{PEP} [%]	[d] E_E in PEE_E [%]	[e] T_g [°C]
PEP	185	1.04	-	-	100	-	-58
PEE_E	-	-	121	1.04	0	73	-49
PEP-PEE_E-50	25	1.04	49	1.07	51	78	-54
PEP-PEE_E-100	52	1.04	104	1.07	50	73	-55
PEP-PEE_E-240	120	1.04	240	1.08	50	70	-57

a. Determined based on SEC from poly(isoprene) aliquot using universal calibration where $Đ = M_w/M_n$
b. From polyisoprene molecular weights and the composition based on ^{1}H NMR obtained on PI-PB
c. Based on SEC measurements with the PEP-PEE$_E$ diblock copolymers
d. Volume fraction calculated based on ^{1}H NMR analysis of PI-PB and assuming equal block densities in PEP-PEE$_E$
e. Based on DSC measurements

SEC traces of the three diblock copolymers and a representative NMR trace that demonstrate low dispersity and complete saturation are provided in Figure 4.2 and Figure 4.3 respectively. Molecular weights and dispersity ($Đ_{PI}$) of PI aliquot and dispersity of PEP-PEE$_E$ ($Đ_{total}$) were determined using room temperature size exclusion chromatography (SEC) at a concentration of 1-2 mg/mL with THF as the mobile phase and calibrated with polystyrene standards. The Mark-Houwink parameters used for the universal calibration are: $K_{1,4\text{-PI}} = 15.7 \times 10^{-3}$ mL/g and $\alpha_{1,4\text{-PI}} = 0.731$, and $K_{PS} = 8.63 \times 10^{-3}$ mL/g and $\alpha_{PS} = 0.736$.[116] The microstructure of the PI and PB blocks were determined by integration of

characteristic peaks in ^{1}H NMR spectra obtained from 10% (w/w) $CDCl_3$ solutions using a Bruker HD500 spectrometer. All the PI blocks contain 94% 1,4 and 6% 3,4 repeat units based on these measurements. The compositions in PI-PB block copolymers were also determined using ^{1}H NMR and the molecular weights of PI-PB and PEP-PEE$_E$ block copolymers were calculated based on the compositions and PI molecular weight determined with SEC.

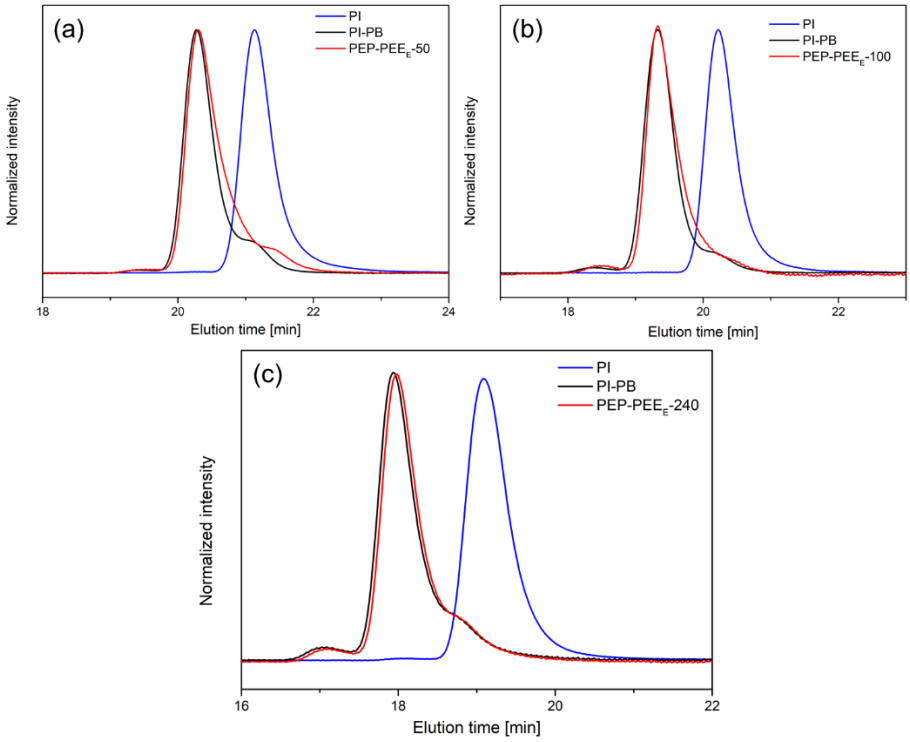

Figure 4.2 SEC traces of (a) PEP-PEE$_E$-50 , (b) PEP-PEE$_E$-100 and (c) PEP-PEE$_E$-240 along with the unhydrogenated PI-PB counterparts (black) and PI aliquots prior to the addition of second block (blue). The higher elution time shoulders in the diblock copolymer traces are due to a small amount of termination of living anions prior to addition of the second block.

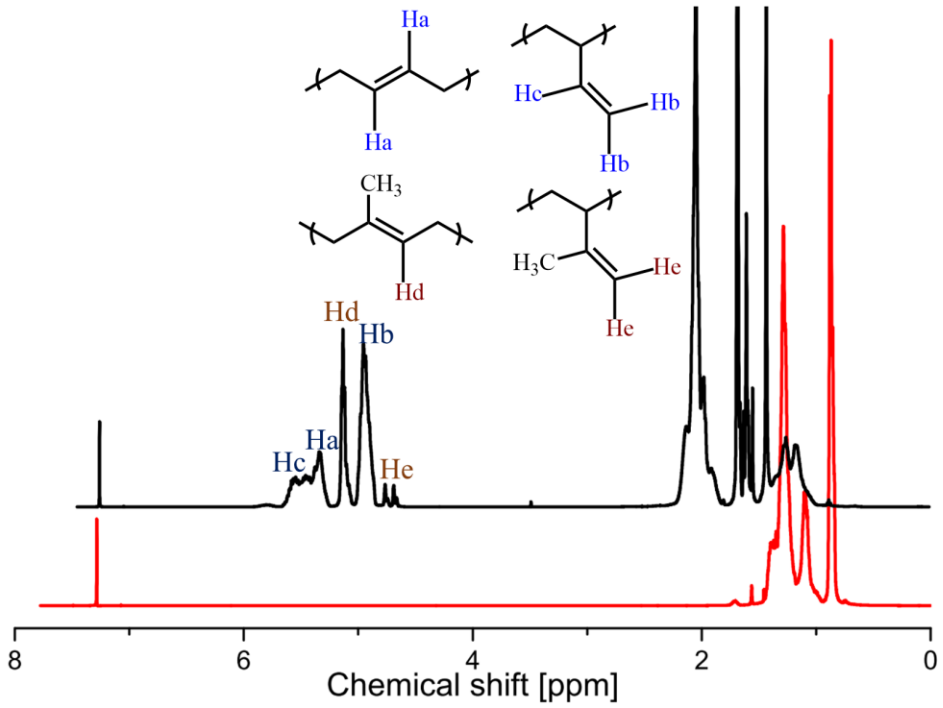

Figure 4.3 ^{1}H NMR traces of PEP-PEE$_E$-50 (red) and unsaturated counterpart PI-PB (black). The disappearance of peaks associated with carbon-carbon double bonds in the NMR spectrum and an invariant SEC trace indicate complete hydrogenation without degradation.

The Glass transition temperatures (T_g) were measured by DSC. PEP-PEE$_E$ block copolymers exhibit a single T_g that lies between those of the two homopolymer counterparts (See Figure 4.4). All three diblock copolymers are disordered at room temperature, exhibiting liquid-like terminal behavior (i.e. $G' \sim \omega^2$, $G'' \sim \omega$) in the rheological spectra, exemplified by the master curve for PEP-PEE$_E$-240 shown in Figure 4.5.

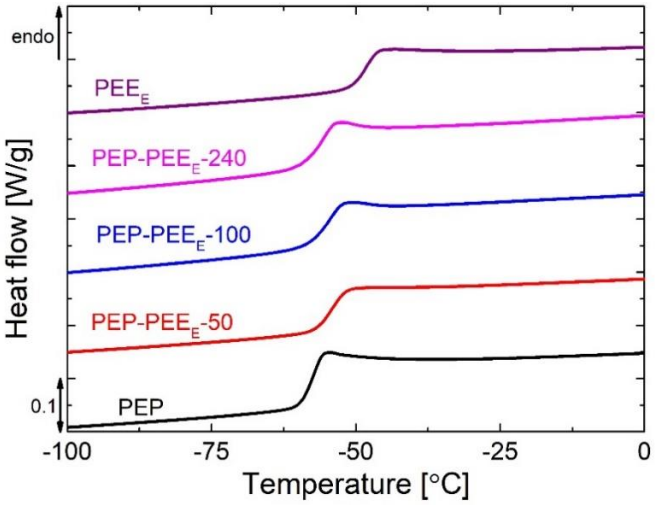

Figure 4.4 DSC traces of PEP, PEP-PEE$_E$-50, PEP-PEE$_E$-100, PEP-PEE$_E$-240 and PEE$_E$ obtained during heating at 10 °C/min. Curves are shifted vertically for clarity. The single glass transition temperatures of the PEP-PEE$_E$ diblock copolymers are consistent with disordered homogeneous material.

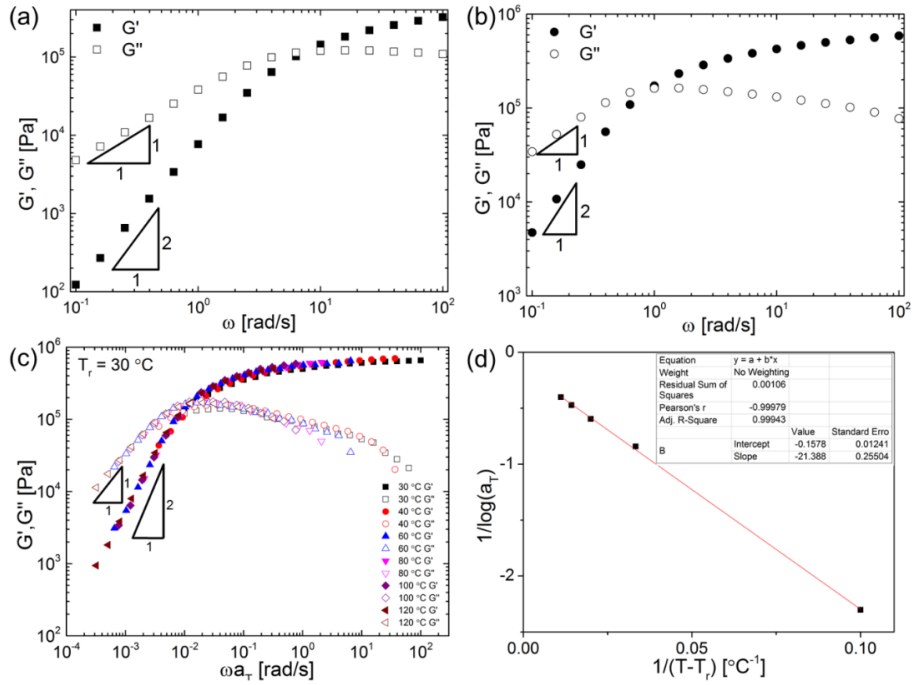

Figure 4.5 Dynamic mechanical storage (G´) and loss (G´´) moduli of (a) PEP-PEE$_E$-50 and (b) PEP-PEE$_E$-100 at 30 °C, and (c) a master curve of PEP-PEE$_E$-240 constructed using frequency sweep data obtained from 30 °C to 120 °C with a reference temperature 30 °C. The shift factors used in (c) are plotted in (d). Low frequency terminal behavior (G´ ~ ω^2 and G´´ ~ ω) indicates that all the PEP-PEE$_E$ diblock copolymers are disordered at room temperature.

4.3.2 Blend morphology

Representative TEM micrographs obtained from *i*PP/PEE_E and *i*PP/PEP blends containing 5 wt% additive are presented in Figure 4.6. The PEE_E used in our work is melt-miscible with *i*PP as evidenced by the lack of any segregated domain structure in Figure 4.6a; Yamaguchi *et al.*[137] reported similar behavior for *i*PP/ethylene-butene rubber (EBR) blends. On the other hand, the 5 wt% *i*PP/PEP blend shows a macrophase separated structure as often observed in rubber toughened *i*PP blends containing EPR rubber with a mixture of particles sizes up to about 1μm in diameter.

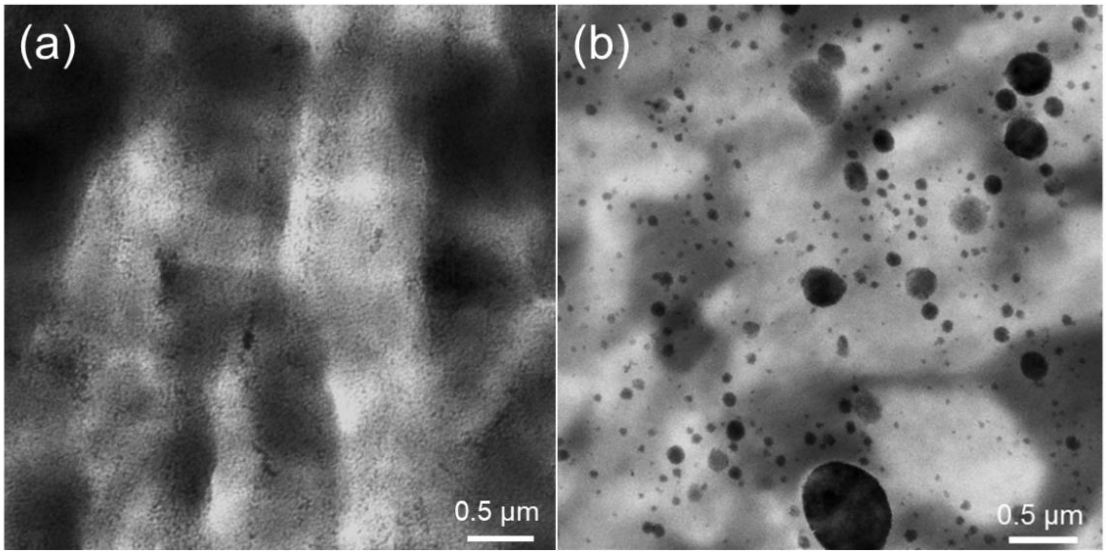

Figure 4.6 Representative TEM micrographs of 5 wt% (a) PEE_E and (b) PEP in *i*PP.

TEM images of the three *i*PP/PEP-PEE_E blends with 5 wt% concentrations are shown in Figure 4.7. Interestingly, the 5 wt% *i*PP/PEP-PEE_E-50 blend (Figure 4.7a) is essentially featureless, similar to Figure 4.6a, suggesting that PEP-PEE_E-50 is miscible with the *i*PP in the melt state. The 5 wt% *i*PP/PEP-PEE_E-100 blend shows discrete micelles

with an average size of approximately 80 nm in diameter while the 5 wt% *i*PP/PEP-PEE$_E$-240 blend displays somewhat larger particles and a larger distribution of particle diameters.

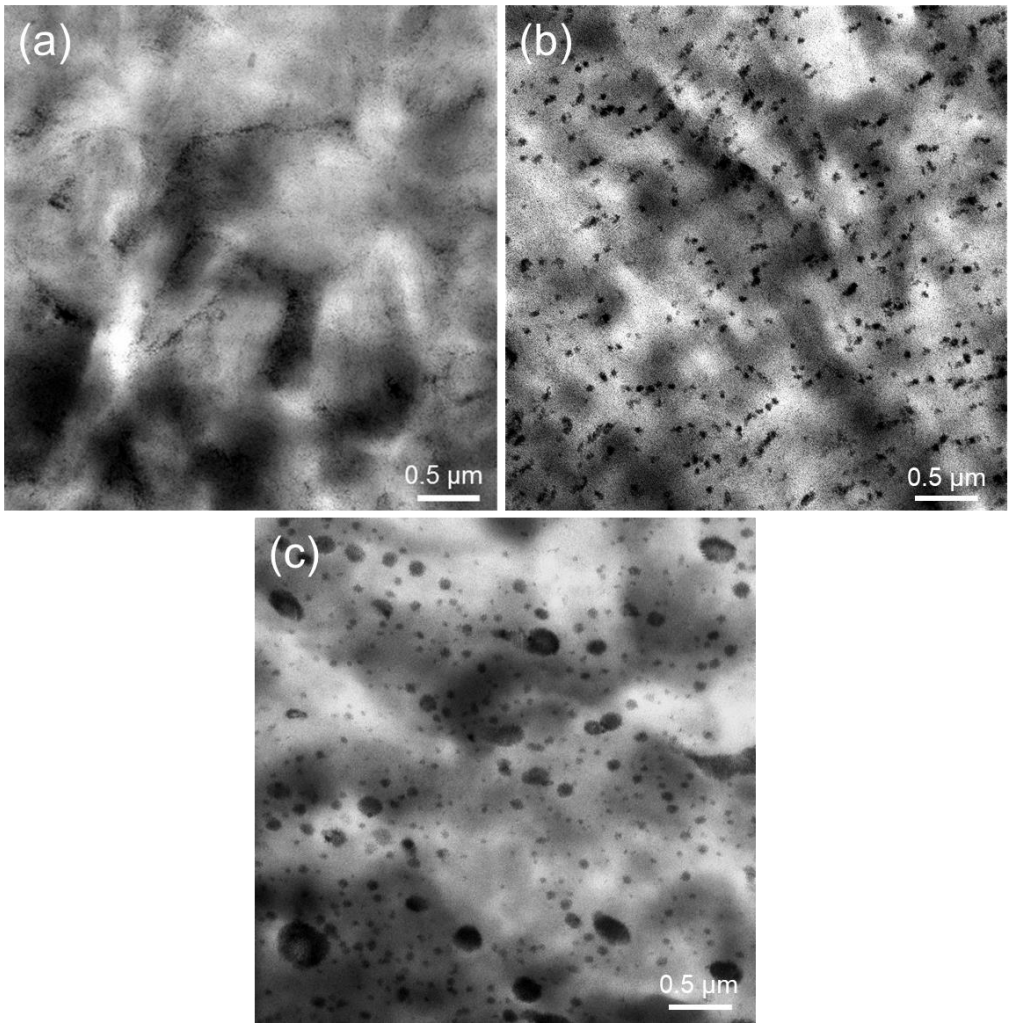

Figure 4.7 Representative TEM micrographs of 5 wt% (a) PEP-PEE$_E$-50, (b) PEP-PEE$_E$-100 and (c) PEP-PEE$_E$-240 in *i*PP.

Blend morphologies associated with the injection molded samples were also studied using TEM, which displayed very similar structures to the ones found in the compression molded blends (See Figure 4.8).

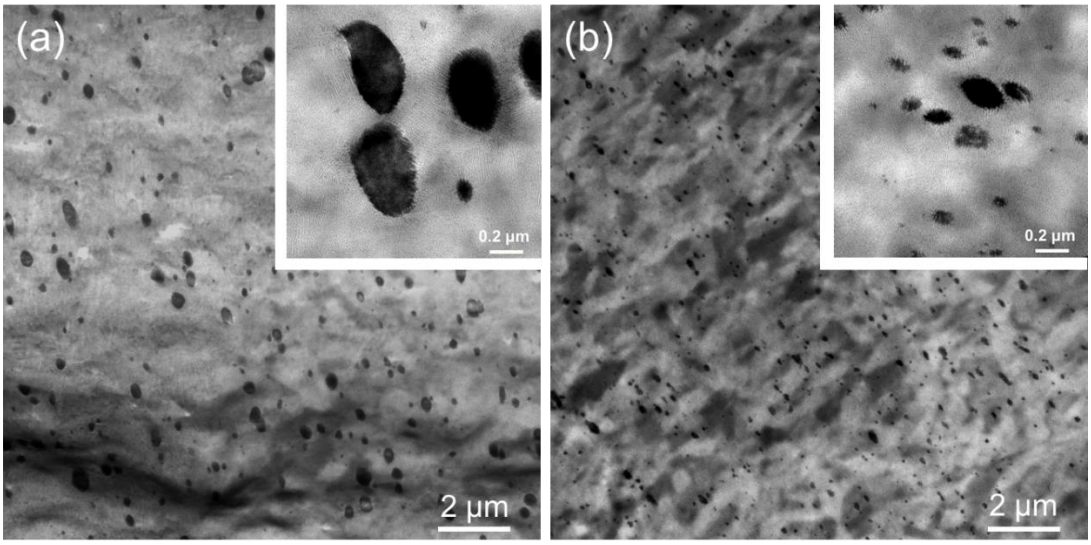

Figure 4.8 TEM micrographs of injection molded (a) 5 wt% *i*PP/PEP and (b) 5 wt% *i*PP/PEP-PEE$_E$-240. Larger magnification images are provided in insets. The morphology in blends prepared by injection molding is similar to those prepared by compression molding in Figure 4.6 and Figure 4.7.

SEM micrographs of the solvent extracted *i*PP/PEP-PEE$_E$-100, *i*PP/PEP-PEE$_E$-240 and *i*PP/PEP blends with 5 wt% concentrations are shown along with the corresponding droplet size distributions in Figure 4.9. These images are consistent with the TEM micrographs shown in Figure 4.6 and Figure 4.7. The diameters of at least 300 droplets were calculated for each blend based on $d = 2\sqrt{\frac{A_i}{\pi}}$ where A_i is the area of an individual droplet that is measured with ImageJ. The average droplet size for the PEP-PEE$_E$ diblock copolymers is about 5 times smaller than that obtained with PEP, demonstrating that the *i*PP-miscible PEE$_E$ block plays a significant role in dispersing the *i*PP-immiscible PEP blocks at a length scale of approximately 100 nm. As shown in Figure 4.10, the average particle size in *i*PP/PEP-PEE$_E$-100 somewhat depends on block copolymer concentration, and increases to d_n = 141 nm at 10 wt%.

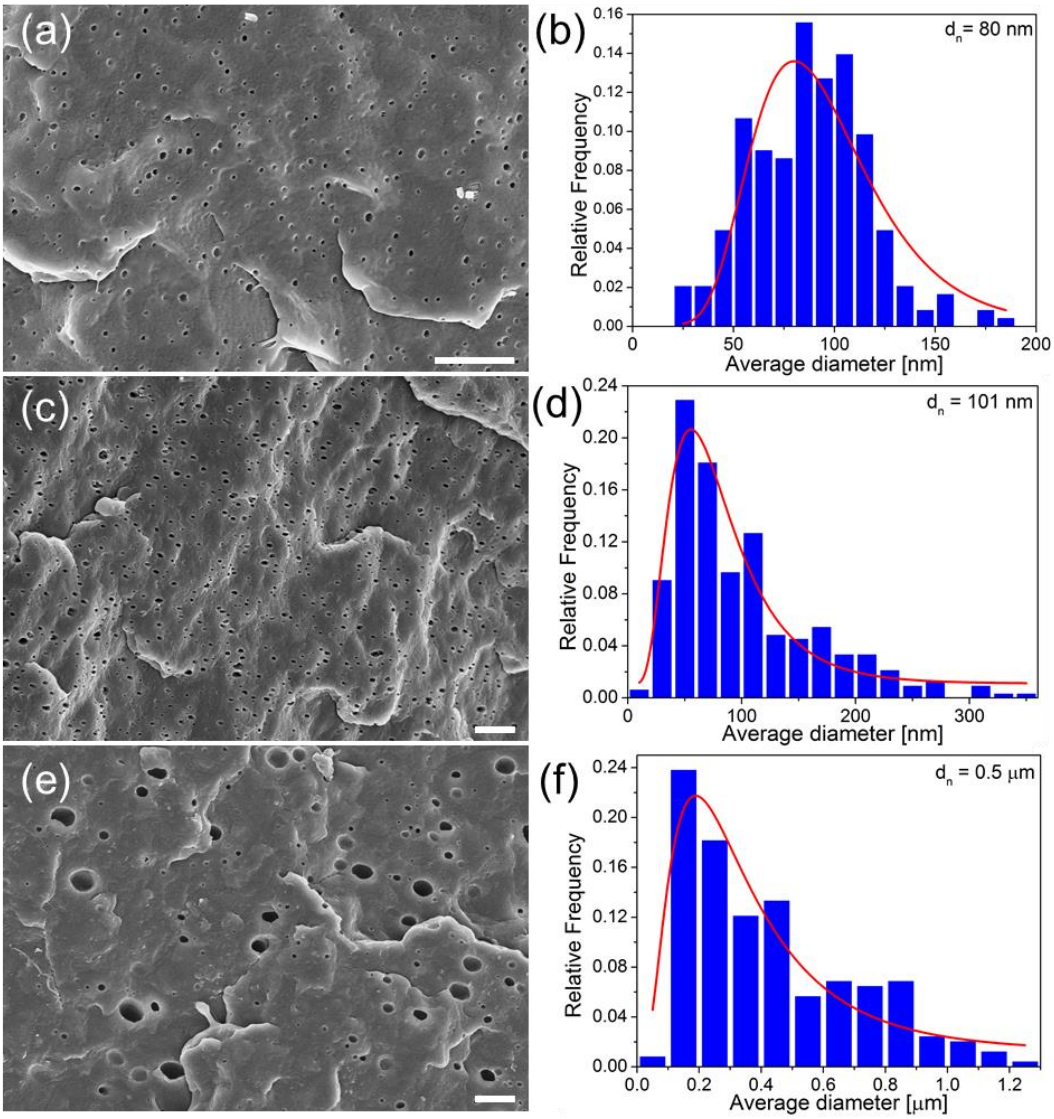

Figure 4.9 SEM micrographs and corresponding particle size distributions of (a, b) 5 wt% PEP-PEE$_E$-100; (c, d) PEP-PEE$_E$-240; and (e, f) PEP in *i*PP respectively after THF etching. Scale bars are 2 μm.

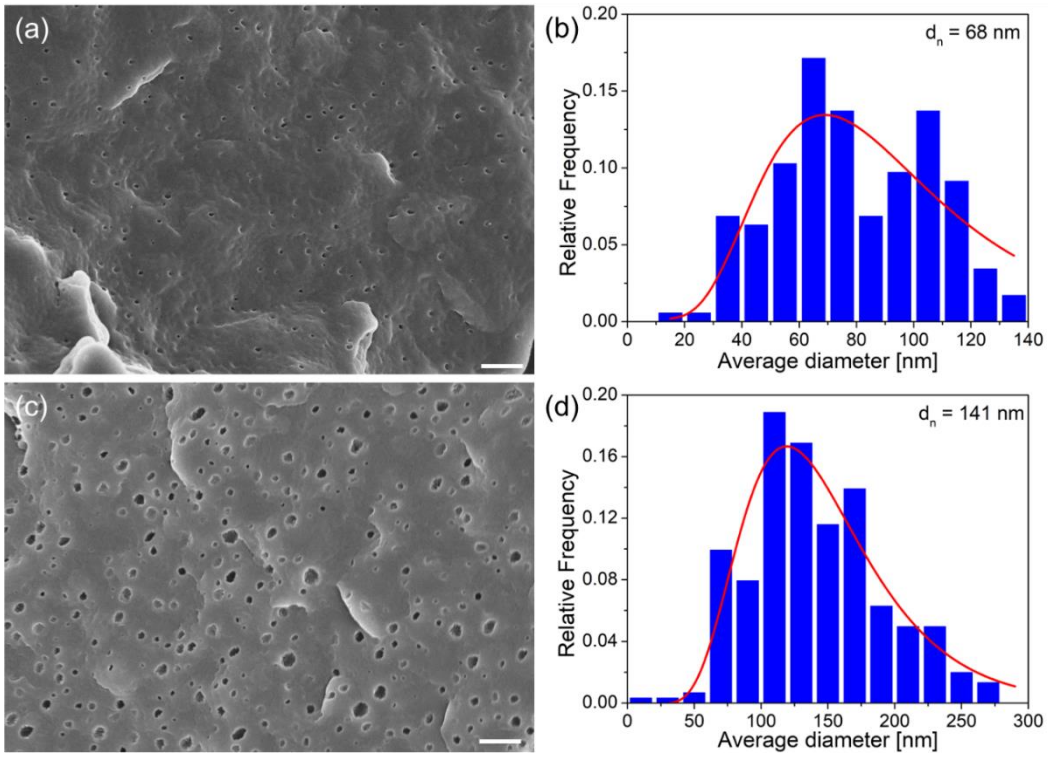

Figure 4.10 SEM micrographs and histograms of size distributions of *i*PP/PEP-PEE$_E$-100 blends with loadings of (a,b) 2.5 wt% and (c,d) 10 wt%. Scale bars are 2 μm. The droplet size somewhat depends on the loadings, increasing from 70 nm (2.5 wt% loading) to 140 nm (10 wt% loading).

4.3.3 Tensile properties

Representative stress-strain curves for all the 5 wt% blends along with the unmodified *i*PP are presented in Figure 4.11a. The pristine *i*PP material breaks at about 20% strain. We note that the break strain value of this particular *i*PP is relatively low compared to those of other commercial *i*PPs possibly due to processing condition (i.e. cooling rate) and physical aging but similar values have been reported by other researchers at ambient temperature and comparable strain rates.[138, 139] The addition of PEP homopolymer increases the strain at break to 100%. Incorporation of discrete 80 to 100 nm size PEP-PEE$_E$ droplets results in a very tough material, raising the strain at break to 500%. Images

of tensile specimens of 5 wt% *i*PP/PEP-PEE$_E$-100 blends at different stages during the tensile experiments (yield point (4-6%), 20%, 100% and 500% strain) are provided along with the stress-strain curve in Figure 4.11b. It is interesting that the whole gauge region is whitened at the yield point, likely due to cavitation of the uniformly dispersed micelles, which will be considered in the discussion section.

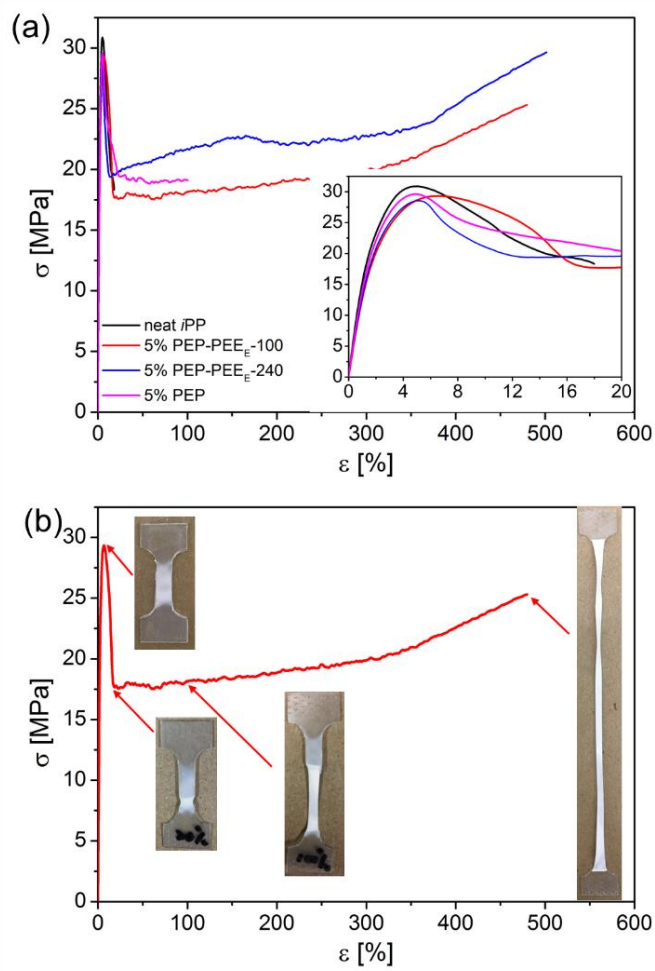

Figure 4.11 (a) Stress-strain curves from *i*PP blends with 5 wt% PEP homopolymer and PEP-PEE$_E$ block copolymers. The inset shows the small strain region. (b) Images of *i*PP/PEP-PEE$_E$-100 tensile specimens at different stages of deformation. The image at 500% strain has been scaled down by a factor of 0.6 relative to the other photographs.

Stress-strain curves obtained as a function of concentration between 1.25 and 20 wt% PEP-PEE$_E$-100 are displayed in Figure 4.12a; at least ten independently fabricated specimens were tested for each blend composition. Two key parameters, elastic modulus and tensile toughness (area under stress-strain curve prior to failure) are plotted against the weight fraction of PEP-PEE$_E$-100 in Figure 4.12b. Merely 2.5 wt% BCP, produces optimal toughness with little deterioration in the elastic modulus. A full set of mechanical properties for all the blends studied in this work is presented in Table 4.2.

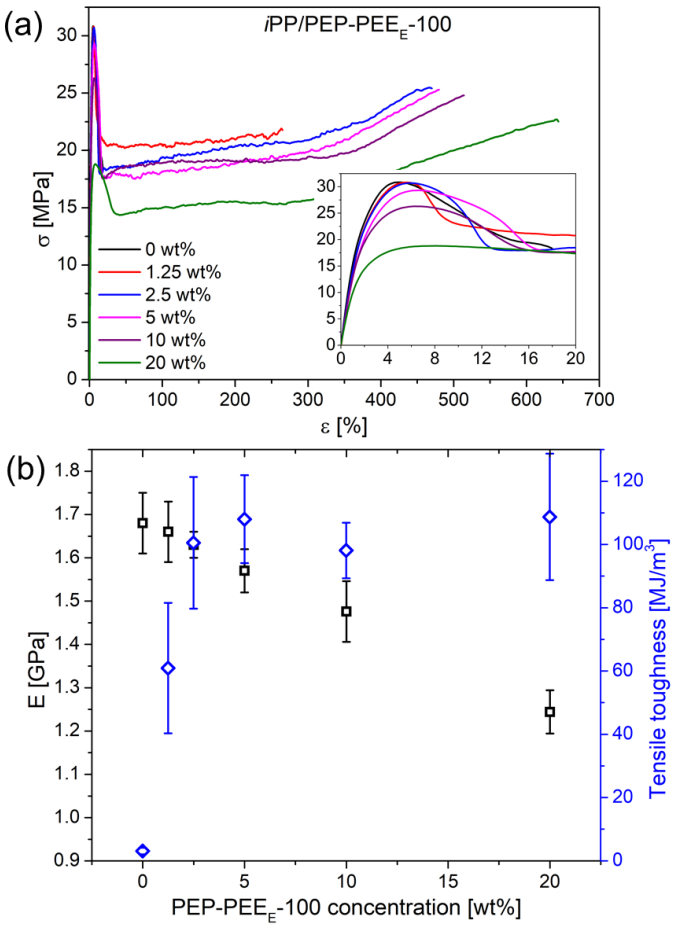

Figure 4.12 (a) Stress-strain curves of *i*PP/PEP-PEE$_E$-100 blends with concentrations of 1.25-20 wt%. Small strain limit is shown in the inset. (b) Elastic modulus (*E*) and tensile toughness as a function of PEP-PEE$_E$-100 concentration. The error bars represent standard deviations based on at least 10 measurements.

Table 4.2 Summary of tensile properties of the *i*PP/PEP and *i*PP/PEP-PEE$_E$ blends

Blends	BCP concentration [%]	E [GPa]	σ_y [Mpa]	ε_b [%]	Tensile toughness [MJ/m^3]
***i*PP**	0	1.68 ± 0.07	31 ± 1	14 ± 5	3 ± 1
***i*PP/PEP**	5	1.53 ± 0.05	30 ± 1	106 ± 68	25 ± 14
***i*PP/ PEP-PEE$_E$-100**	1.25	1.66 ± 0.07	31 ± 2	278 ± 188	61 ± 20
	2.5	1.63 ± 0.03	30 ± 2	464 ± 73	101 ± 21
	5	1.57 ± 0.05	30 ± 1	457 ± 50	108 ± 14
	10	1.48 ± 0.07	25 ± 1	506 ± 19	98 ± 9
	20	1.24 ± 0.05	19 ± 1	616 ± 105	109 ± 20
***i*PP/ PEP-PEE$_E$-240**	1.25	1.64 ± 0.02	32 ± 1	278 ± 186	73 ± 29
	2.5	1.57 ± 0.06	31 ± 1	425 ± 33	108 ± 19
	5	1.55 ± 0.03	30 ± 1	507 ± 22	122 ± 8
	10	1.37 ± 0.08	28 ± 1	553 ± 75	130 ± 20
	20	1.21 ± 0.09	25 ± 1	511 ± 49	102 ± 13

4.3.4 Impact properties

The effects of PEP-PEE$_E$ diblock copolymers and PEP homopolymer on the room-temperature impact strength of *i*PP are illustrated in Figure 4.13. Pure *i*PP is brittle with an Izod impact strength of 24 J/m, which is consistent with the value reported by other researchers[44, 140, 141]. The addition of 5 wt% and 10 wt% PEP leads to a modest and nearly invariant improvement in impact toughness. Adding 5 wt% of PEP-PEE$_E$-100 or PEP-PEE$_E$-240 increases the impact strength by a factor of 5 and 10 wt% of the higher molecular weight diblock results in a 12-fold enhancement in the Izod impact strength. The inset in Figure 4.13b presents the images of specimens after testing, offering qualitative evidence of the failure modes. Pure *i*PP fails by brittle fracture with no stress whitening. The 10 wt% *i*PP/PEP blend produces a little stress whitening near the tip of the notch. 'Shear lips' were observed in both specimens, indicating a stress state that is close to plane stress near the free surface. Adding 10 wt% *i*PP/PEP-PEE$_E$-240, on the other hand, leads to extensive

stress whitening in the entire area of failure and beneath the fracture surface, indicating a large plastic zone and a tough fracture mode.

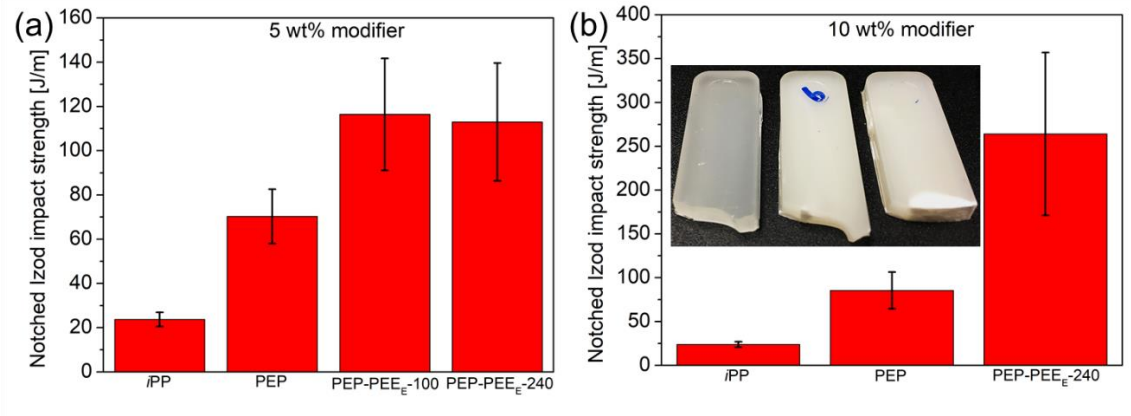

Figure 4.13 Notched Izod impact strength of blends with concentrations of (a) 5 wt% and (b) 10 wt%. The error bars represent standard deviations based on at least 10 measurements. The inset in (b) shows the side view of the specimens after fracture (from left to right are pure *i*PP, 10 wt% PEP and 10 wt% PEP-PEE$_E$-240).

To put our Izod impact strength in some context, we compared our results with literature as shown in Figure 4.14, including three different commercial olefin block copolymers (OBCs), two types of styrene-butadiene-styrene (SBS) block copolymer and ethylene-propylene-monomer (EPDM) rubber benchmarks. It is obvious that the *i*PP modified with PEP-PEE$_E$ BCPs offer comparable impact toughness to some of the best performers while fewer modifiers are required.

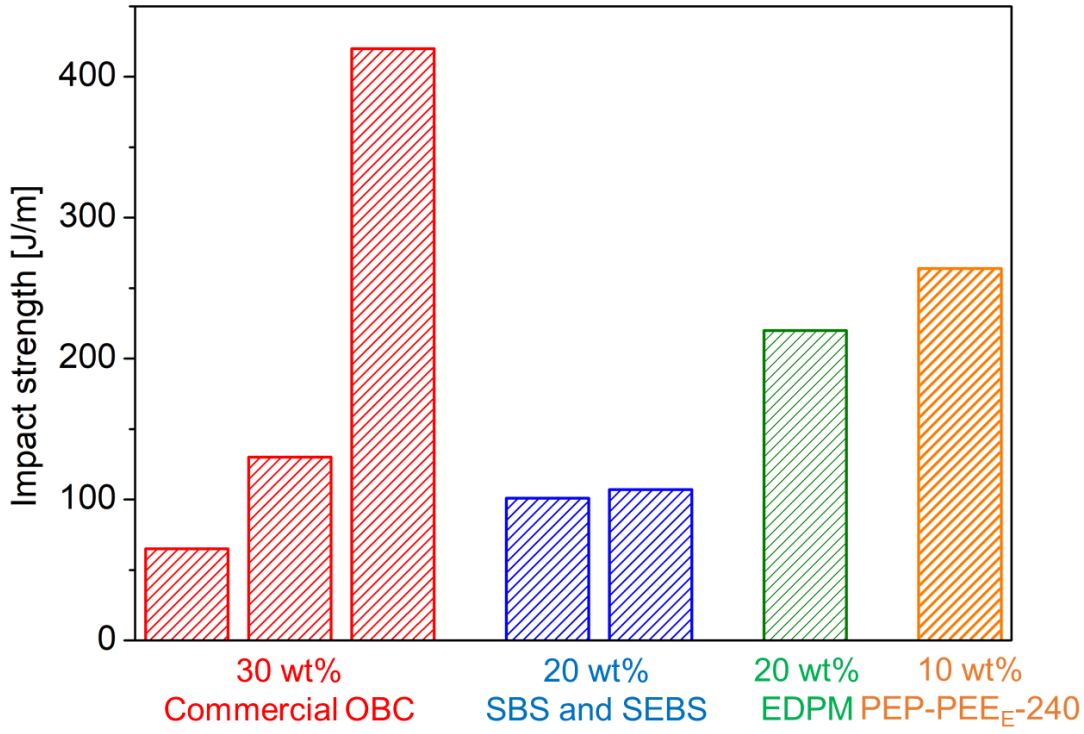

Figure 4.14 Notched Izod impact strength of *i*PP blends modified with commercial OBC, SBS, EPDM benchmarks and PEP-PEE$_E$-240. (Results were replotted from studies by Liu *et al.*[53], Abreu *et al.*[51] and Van der Wal *et al.*[142])

4.3.5 Fractography

SEM micrographs comparing the fracture surfaces of pure *i*PP, 10 wt% *i*PP/PEP and 10 wt% *i*PP/PEP-PEE$_E$-240 blend are presented in Figure 4.15, demonstrating different fracture behaviors during the Izod impact testing. The fracture surface of pure *i*PP is smooth with almost no distinguishable small features associated with energy absorption. The surface of the failed 10 wt% *i*PP/PEP blend is rougher and the higher-magnification image in the inset reveals voids that are spherical in shape, indicating particle pull-out likely due to poor adhesion between PEP and the *i*PP matrix. The fracture surface of the 10 wt% *i*PP/PEP-PEE$_E$-240 specimen is very rough with grossly deformed and thick features. Wave-like terraces with strips aligning perpendicular to the impact fracture

direction are evident in the inset possibly due to matrix shear yielding. To gain a better idea of the microstructures under the fracture surface, the specimen was cut and viewed using SEM. Characteristic multiple-crazing structures were observed 2mm under the fracture surface, as seen in Figure 4.15d, which accounts for the stress-whitened zone found under the fracture surface and seen in the specimen image in Figure 4.13b. Hence, shear yielding and multiple-crazing are both operative in the *i*PP/PEP-PEE$_E$-240 blend during impact testing.

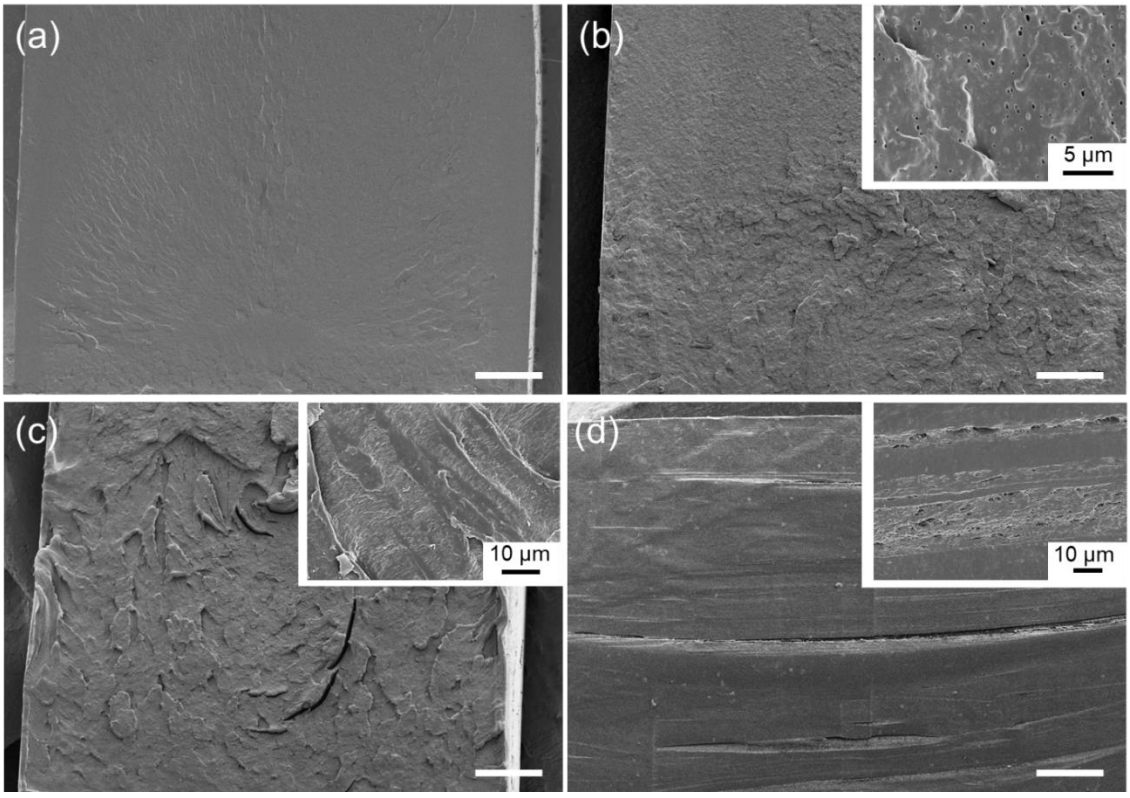

Figure 4.15 SEM micrographs of fracture surfaces of (a) pure *i*PP, (b) 10 wt% *i*PP/PEP blend and (c) 10 wt% *i*PP/PEP-PEE$_E$-240 blend after the notched Izod impact testing. (d) Whitened zone underneath the fracture surface of the 10 wt% *i*PP/PEP-PEE$_E$-240 blend. Insets provide microscopic views of the surfaces. Scale bars are 0.5 mm unless specified otherwise.

4.4 Discussion

4.4.1 Diblock copolymer phase behavior and micelle formation

The three PEP-PEE$_E$ diblock copolymers are all disordered at room temperature, which is clearly demonstrated by the DSC (Figure 4.4) and rheological measurements (Figure 4.5). The χ parameter for PEP and PEE$_{E78}$ (78% E$_E$ units) was estimated by Graessley *et al.*[143] to be 3.64×10^{-3} at 167 °C with a reference volume of 1.0×10^{-22} cm^3 using the solubility parameter approach. This translates into a segregation strength that ranges from $\chi N = 2$ for PEP-PEE$_E$-50 to $\chi N = 9.6$ for PEP-PEE$_E$-240, where both values are below the mean-field criterion for ordering in symmetric diblock copolymers, $(\chi N)_{ODT} = 10.5$. At room temperature, the segregation strength will be higher, but fluctuation effects will increase $(\chi N)_{ODT}$, hence we conclude that the state of disorder documented in Figure 4.5 for PEP-PEE$_E$-240 is consistent, within reasonable experimental uncertainty, with expectation based on previous work. Also, χ between *i*PP and EPR (47 mol% ethylene) was reported by Matsushita *et al.*[144] to be 5.8×10^{-3} at 205 °C with a reference volume of 1.0×10^{-22} cm^3. The result shown in Figure 4.5a indicates that the molecular weight of PEP-PEE$_E$-50 does not meet the threshold in segregation strength necessary to segregate the PEP blocks into micelle cores when mixed with the *i*PP. Owing to the disperse nature of the *i*PP ($Đ$ = 7.5) we cannot make a quantitative assessment of this finding. Nevertheless, doubling the molecular weight, hence doubling the segregation strength drives the formation of well-dispersed 80 nm micelles in the *i*PP/PEP-PEE$_E$-100 blend (Figure 4.7b).

Intuitively, we would expect the micelle diameter to be considerably smaller than what we observed based on a simple estimate of the radius of gyration $R_g^2 = \frac{1}{6}Nb^2$ for PEP-PEE$_E$-100. Taking $N \approx 2000$ and b = 0.65 nm yields R_g =12 nm, which roughly

corresponds to a micelle diameter of $d \approx 3R_g = 36$ nm, less than half what is found in Figure 4.7b and 4.7c. We postulate that the discrepancy derives from two possible sources. Firstly, because the block copolymers are inherently homogeneous (i.e. disordered), the particle size is not constrained by the dimension of the coils. Preferential mixing between PEE_E and *i*PP ($\chi \approx 0$)[27] suggests that the outer surface of the micelles are comprised of a PEE_E corona. However, since the bulk diblock is homogeneous (see Figure 4.5) the core can be swollen with the disordered diblock copolymer. Secondly, the micelles may be swollen with *i*PP, especially the PEE_E-rich corona. Here we note that the low molecular weight fraction of the matrix material places the corona in the so-called 'wet brush' regime since the PEE_E block molecular weight in PEP-PEE_E-100 (M_n = 52 kg/mol) is roughly twice the molecular weight of the *i*PP (M_n = 21 kg/mol).[145] Thus the lower molecular weight *i*PP chains can penetrate deeply into the micelle corona swelling the micelle outer layer. Furthermore, the possibility of *i*PP chains swelling the micelle cores cannot be excluded since the repulsion between *i*PP and PEP is not significant. We believe that the first mechanism is dominant since swelling with homopolymer alone would result in roughly an 8-fold increase in the volume fraction of particles, which is not supported by the TEM and SEM images in Figure 4.7 and Figure 4.9.

4.4.2 Toughening mechanism

DSC has been employed to study the crystallization and melting behavior of the *i*PP/PEP-PEE_E blends. It was found that the presence of diblock copolymers does not alter the crystallinity or the crystal form of the *i*PP (See Figure 4.16), ruling this out as a contributing factor to the enhanced toughness.

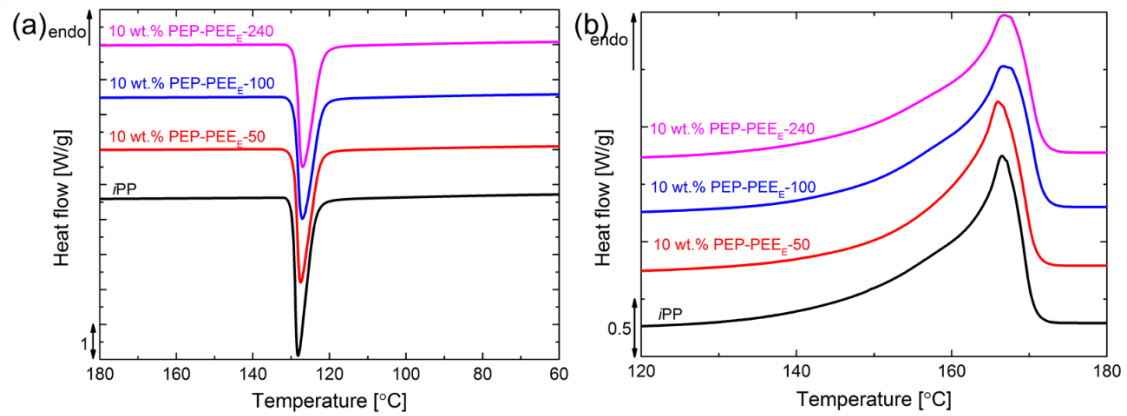

Figure 4.16 DSC traces of 10 wt% *i*PP/PEP-PEE$_E$ blends and pure *i*PP obtained while (a) cooling from 200 °C, and (b) heating following the cooling cycle both at a rate of 10 °C/min. Curves are shifted vertically for clarity. The crystallization and melting temperatures of *i*PP are not changed with the presence of the PEP-PEE$_E$ block copolymer modifiers.

We attribute the significantly improved toughness seen in tensile and notched Izod impact testing to matrix shear yielding and multiple-crazing induced by the particle cavitation. TEM micrographs of the whitened gauge area of the 10 wt% *i*PP/PEP-PEE$_E$-240 and 5 wt% *i*PP/PEP blends taken at the yield point are presented in Figure 4.17. The voids seen in the *i*PP/PEP blend are very large (~ 1 μm in diameter) and localized, and crazing structures are seen near the ends of the voids. A craze that started to emerge from a large particle is shown in the inset consistent with preferential initiation of crazing from larger particles due to higher volumetric strain energy release. We suspect that the large voids and localized crazing structures will lead to unstable crack growth and eventually the failure at $\varepsilon_b \approx 100\%$ seen in Figure 4.11a. In the 10 wt% *i*PP/PEP-PEE$_E$-240 blend, voids are nano-sized and uniformly dispersed in the entire area as marked by the yellow arrows. Shear banding structures were identified in a higher magnification image, which is consistent with a shear yielding mechanism[62].

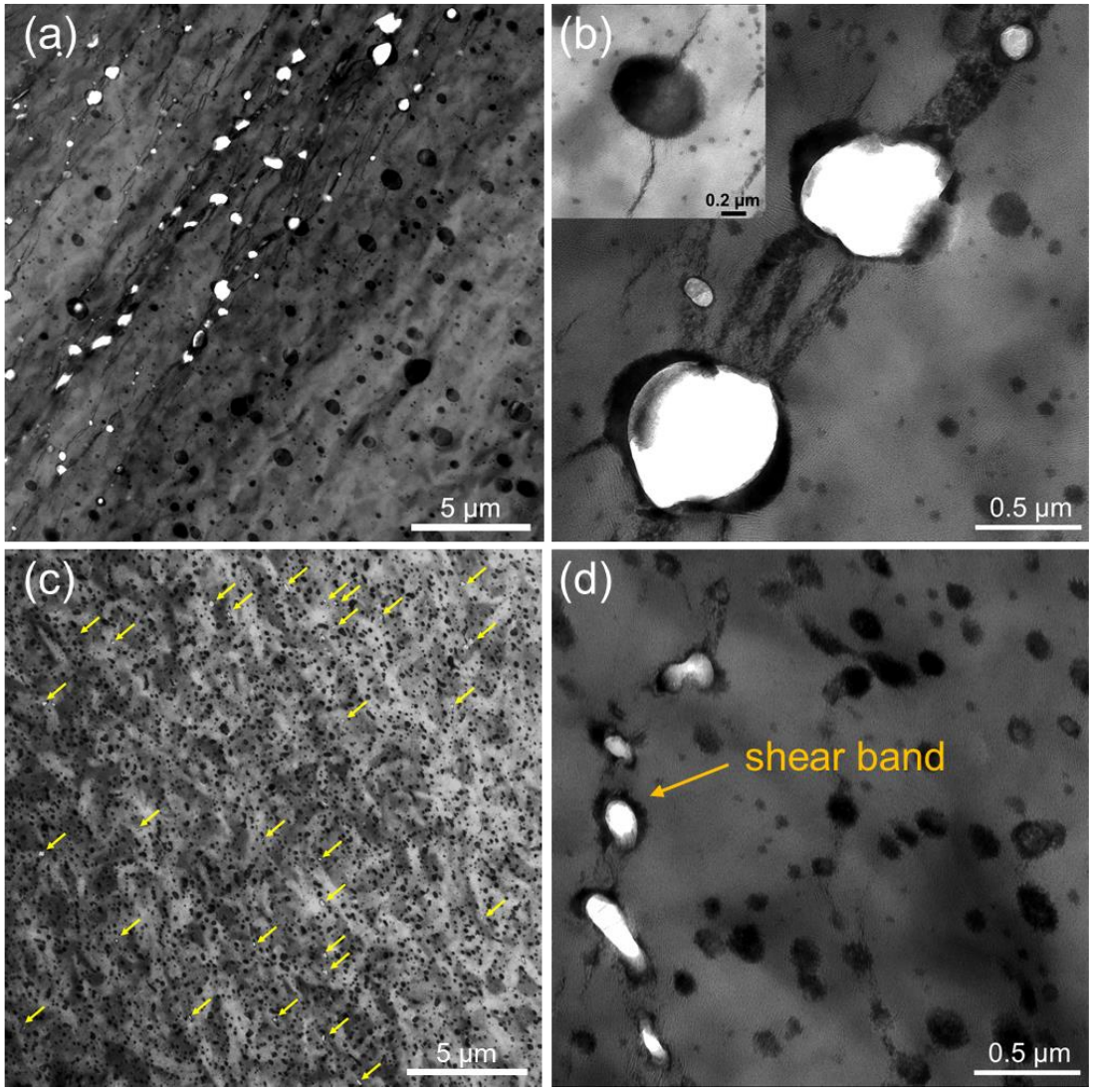

Figure 4.17 TEM images of (a, b) 5 wt% *i*PP/PEP blends at the yield point and (c, d) 10 wt% *i*PP/ PEP-PEE$_E$-240 blends at the yield point. The inset of (b) demonstrates the formation of a craze around a PEP particle. The yellow arrows in (c) indicate the locations of small cavitated rubber particles.

In-situ videos were shot during the tensile testing to gain a macroscopic view of the specimen during the process (See Figure 4.18). Stretching the pure *i*PP specimens produced localized high strains in a small region of the gauge section for the pure *i*PP at the yield point, resulting in crack growth and failure at that location. Conversely, the overall strain was distributed evenly throughout the entire gauge region in the 5 wt% *i*PP/PEP-PEE$_E$-100

blend and several 45-degree shear bands developed at the yield point, consistent with the TEM evidence and the entirely stress-whitened gauge section shown in Figure 4.11b.

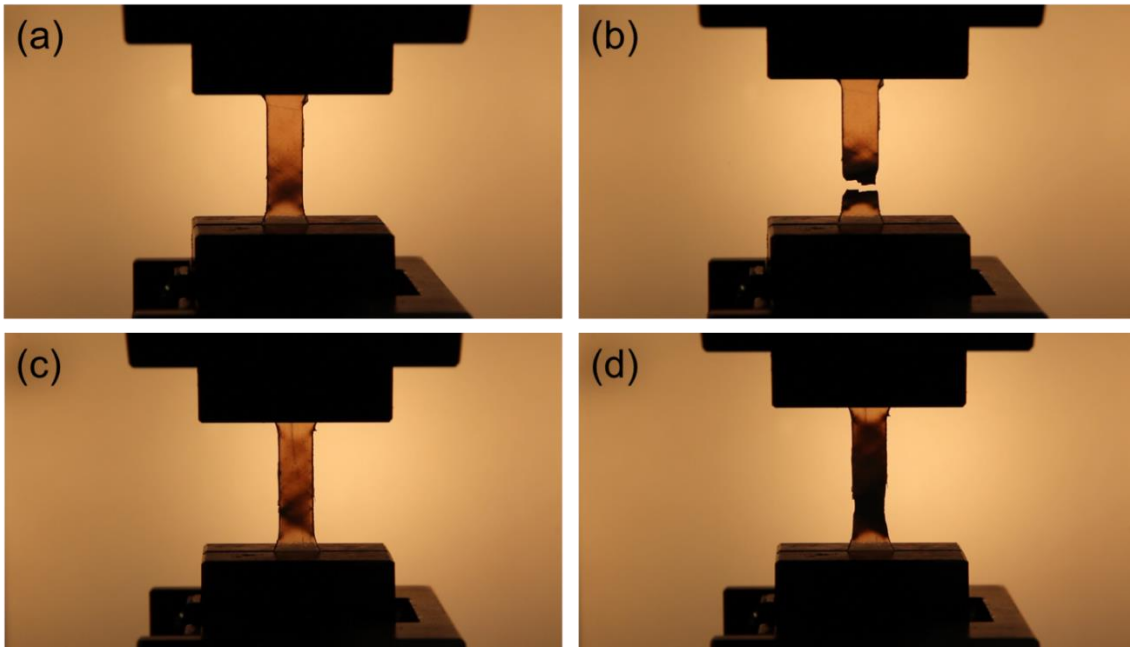

Figure 4.18 Images of (a) pure *i*PP at the yield point and (b) at 20% strain; (c) 5 wt% *i*PP/PEP-PEE$_E$-100 at the yield point and (d) at 20% strain during tensile testing with a polarized light source. The crosshead speed is 5 mm/min.

To help explain the role played by particle cavitation in the *i*PP/PEP-PEE$_E$ and *i*PP/PEP blends, we applied a model developed by Bucknall and Paul,[57, 58] which accounts for the change in energy before and after a voiding event. The elastic energy stored in the rubber particle before cavitation and the energy of the cavitated rubber are given by,

$$U_{\text{rubber}} = \frac{2\pi R^3 K^*}{3}\varepsilon_{\text{vR0}}^2 \quad (1)$$

$$U_{\text{cavitated rubber}} = \frac{2\pi R^3 K^*}{3}(\varepsilon_{\text{vR0}} - \frac{r_{\text{void}}^3}{R^3})^2 + 4\pi r_{\text{void}}^2 \Gamma + 2\pi r_{\text{void}}^2 G_{\text{r}} f(\lambda_{\text{f}}) \quad (2)$$

where R is the radius of the rubber particle, K^* is the effective bulk modulus, ε_{vR0} is the initial strain the rubber particle is subjected to, r_{void} is the radius of the void, Γ is the rubber-void surface energy, G_r is the rubber shear modulus, and λ_f is the rubber extension ratio. K^* takes the energy release of both the matrix and rubber particle into account and is a function of the bulk modulus of the rubber (K_r), bulk and shear moduli of the matrix (K_m and G_m), and the volume fraction of the rubber (ϕ_r). Significantly, ε_{vR0} is different from the average volume strain ε_v imposed on the blend as a whole, which is a function of K_m, G_m, ϕ_r and ε_v. The last term in Eqn. 2 is neglected since the shear modulus of the rubber (G_r < 1 MPa) is much lower than that of the matrix (G_m ~ 1 GPa). Thus, the energy change associated with the cavitation process is given by:

$$\Delta U = \frac{2\pi R^3 K^*}{3}\left(\varepsilon_{vR0} - \frac{r_{void}^3}{R^3}\right)^2 + 4\pi r_{void}^2 \Gamma - \frac{2\pi R^3 K^*}{3}\varepsilon_{vR0}^2 \qquad (3)$$

The driving force for rubber cavitation is strain energy release counterbalanced by an energy penalty for creating a new surface between the rubber and void.

A plot of ΔU for rubber particles of various sizes at 5 wt% rubber content is presented in Figure 4.19. The shear modulus G_m and bulk modulus K_m are estimated to be 0.6 GPa and 3.5 GPa, respectively, from the elastic modulus 1.68 GPa and an assumed Poisson ratio v = 0.42[146]. A typical value for the bulk modulus of the rubber is K_r = 2.0 GPa at room temperature[147], which gives an effective modulus of K^* = 0.69 GPa. The sample calculation is available in Appendix D. The surface energy Γ is approximately 35 mJ/m^2 for an olefinic rubber[147] and the average initial strain ε_v experienced by the whole specimen is arbitrarily set to 0.5% (see below). The critical particle size at a given initial strain can be obtained by solving $\Delta U = 0$ and $\frac{\partial \Delta U}{\partial R} = 0$ simultaneously, which gives 42 nm

in this example. Particles with a radius smaller than 42nm will not cavitate because $\Delta U > 0$ as shown by the dotted curves in Figure 4.19. Larger particles may cavitate because there is a negative minimum in ΔU at a finite void size; this activated process involves surmounting the small energy barrier evident in Figure 4.19. The majority of the rubbers particles in the micelle containing *i*PP/PEP-PEE$_E$ and *i*PP/PEP blends can cavitate with an initial strain of 0.5%, and we also note that the critical particle size for cavitation is inversely related to the initial strain value. Since the rubber particles are constrained by the surrounding rigid matrix polymer and subjected to substantial triaxial tensile stress states, a relatively large volume strain (ca. 1%) within the rubber particles can be achieved at an overall elongation of 5% in a blend.[54] The onset of yielding in *i*PP blend occurs at approximately 5% elongation so we expect the initial volumetric strain of 0.5% assumed in the calculations is appropriate for the present purpose.

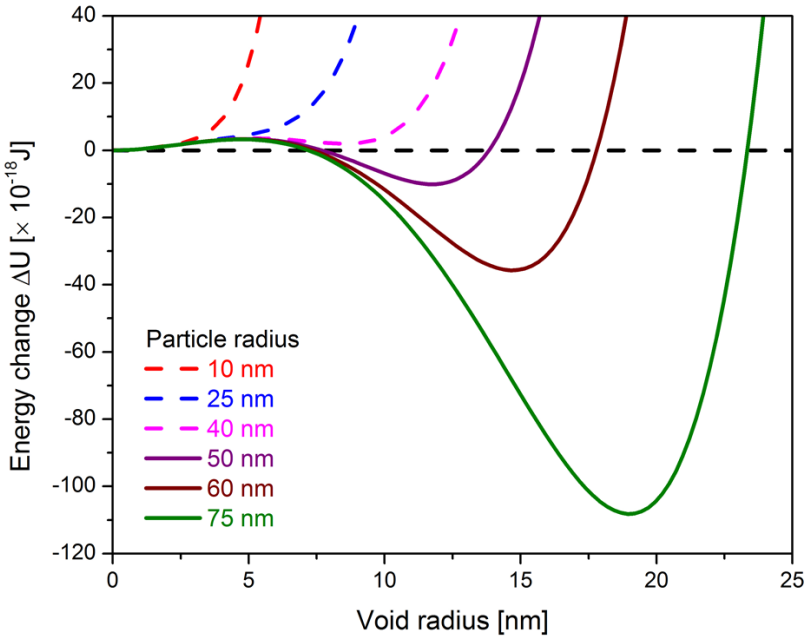

Figure 4.19 Energy change ΔU after cavitation as a function of incorporated particle size in *i*PP matrix at 5 wt% rubber with initial volumetric strain ε_v set to 0.5%.

Bucknall and Paul used the pressure-modified versions of the Von Mises' criterion and Gurson's criterion to estimate the point of shear yielding in the void free and porous polymer materials, respectively. The two criteria are described by the following set of equations,

Von Mises: $$\sigma_e \geq \sigma_{y0} - \mu\sigma_m \quad (4)$$

Gurson: $$\sigma_e \geq (\sigma_{y0} - \mu\sigma_m)(1 - 2\phi_{void}\cosh(\frac{1.5\sigma_m}{\sigma_{y0} - \mu\sigma_m}) + \phi_{void}^2)^{0.5} \quad (5)$$

In these relationships σ_{y0} is the yield stress under zero hydrostatic pressure ($\sigma_m = 0$), μ is the pressure coefficient of the matrix material, ϕ_{void} is the volume fraction of the voids, and the effective stress σ_e and mean stress σ_m are given by,

$$\sigma_e = \sqrt{\frac{(\sigma_1 - \sigma_2)^2 + (\sigma_1 - \sigma_3)^2 + (\sigma_2 - \sigma_3)^2}{2}} \quad (6)$$

$$\sigma_m = \frac{\sigma_1 + \sigma_2 + \sigma_3}{3} \quad (7)$$

where σ_is are the principal stresses.

The effective stress σ_e is plotted against the mean stress σ_m in Figure 4.20 using equations 4 (Von Mises) and 5 (Gurson) for a 5 wt% *i*PP/rubber blend with ϕ_{void} = 5.4%, which is assumed to be equal to the volume fraction of rubber ϕ_r, prior to cavitation, calculated using a rubber concentration of 5 wt% and the densities of the matrix and rubber (ρ_{iPP} = 0.91 g/cm^3 according to the manufacturer and ρ_{PEP} = 0.85 g/cm^3.[148]). Mears *et al.* [55] and Fasce *et al.*[56] measured the yield stress of *i*PP at various pressures and report the pressure coefficient μ = 0.22.[149, 150] The average tensile yield stress of the 5 wt% *i*PP/rubber blends in our study is σ_y = 30.2 MPa, which corresponds to σ_{y0} = 32.4 MPa given by σ_{y0} =

$(1+1/3\mu)\sigma_y$ using equations 4, 6 and 7. Also shown in Figure 4.20 are the solutions to equations 7 and 8 under uniaxial and plane strain stress states with the principal stresses taking the form of (σ, 0, 0) and (σ, σ, $2\nu\sigma$) respectively.

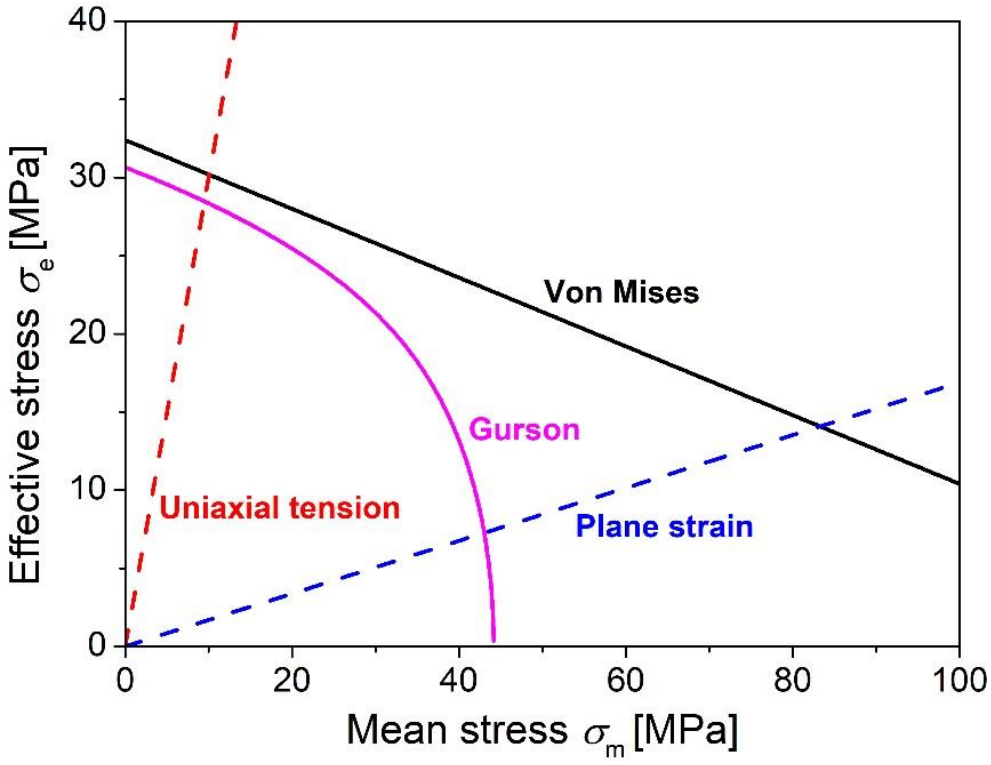

Figure 4.20 Plot of effective stress σ_e against mean stress σ_m for Von Mises (black) and Gurson (magenta) criteria for the void-free and fully cavitated 5 wt% *i*PP/rubber blends given by equations 4 and 5, and under uniaxial tension (red) and plane strain (blue) stress states given by equations 6 and 7.

A so-called 'stress map'[57, 58, 151] was constructed based on the cavitation model and shear yielding criteria (equation 5 and 6) for the 5 wt% *i*PP/rubber blends as shown in Figure 4.21. The horizontal black lines represent two limiting conditions: (*i*) the critical tensile stress σ_{1c} for matrix yielding without cavitation under plane strain, and (*ii*) σ_{1c} for yielding with full cavitation under uniaxial tension. These correspond to the stress levels

in Figure 4.20 where (*i*) the plane strain branch (dashed blue line) intersects the Von Mises branch (black curve) at σ_m = 83 MPa, which corresponds to σ_{1c} = 89 MPa, and (*ii*) the uniaxial branch (red dashed line) intersects the Gurson branch (magenta curve) at σ_m = 9.5 MPa, which corresponds to σ_{1c} = 28.5 MPa. The blue and red dashed curves represent the cavitation criteria under plane strain and uniaxial tension. Based on this stress map particles less than 10 nm in diameter will not cavitate prior to the matrix yielding since the stress required for cavitation to occur under either stress state is higher than the maximum attainable stress level (i.e. matrix yield stress without cavitation under plane strain). Conversely, particles larger than 200 nm in diameter will cavitate before the matrix yields because the stress required for cavitation to occur under either stress state is lower than stress level corresponding to matrix yielding with full cavitation under uniaxial tension. Within the shaded area in Figure 4.21, cavitation and matrix shear yielding are predicted to occur simultaneously. The diblock copolymer particles formed by PEP-PEE_E-100 and PEP-PEE_E-240 both fall within the window, while the larger PEP particles place the associated blend outside this regime. This analysis appears to be consistent with our experimental results, i.e. TEM evidence of cavitation and uniform stress whitening throughout the gauge portion of the specimen.

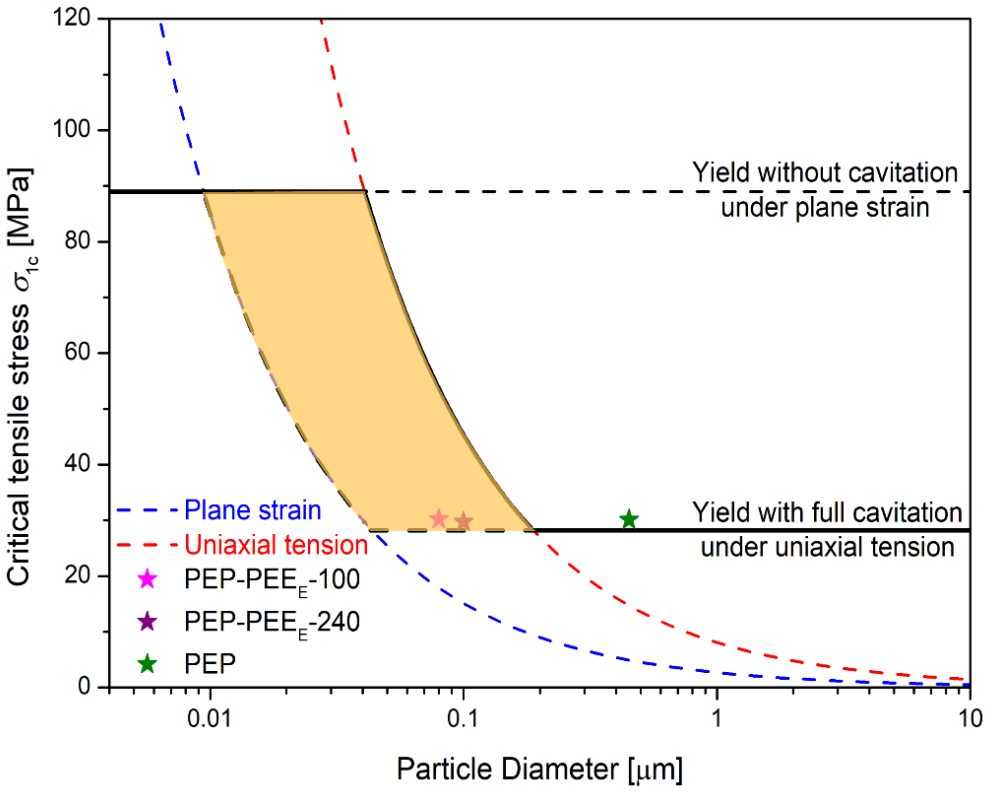

Figure 4.21 Stress map for 5 wt% *i*PP/PEP-PEE$_E$ blends. The horizontal black lines represent matrix yield stresses without cavitation under plane strain and with full cavitation under uniaxial tension conditions. The dashed red and blue curves represent the cavitation criteria under plane strain and uniaxial tension stress states respectively. The shaded region indicates the conditions for cavitation and matrix yielding to occur simultaneously. The stars represent the particle diameters and tensile yield stress of 5 wt% *i*PP/PEP-PEE$_E$-100, *i*PP/PEP-PEE$_E$-240 and *i*PP/PEP blends measured in the experiments.

With the specimen geometry and materials employed in this work, a state of pure plane strain is not achieved in the notched Izod impact tests. Accordingly, the stress state during testing will reflect an intermediate state between plane strain and uniaxial tension. From Figure 4.20, the highest principal stress (σ_1) for matrix yielding under plane strain assuming full cavitation is calculated to be 45 MPa. Therefore, the matrix yield stress σ_{1y} associated with the impact test lies between 45 MPa (plane strain) and 28 MPa (uniaxial tension). We can estimate the stress for crazing in a rubber toughened blend[58]:

$$\sigma_{\text{crazing}} = \sqrt{\frac{\pi E G_{crazing}}{2(1-\nu^2)d}} \tag{8}$$

where E is the elastic modulus, d is the rubber particle diameter and $G_{\text{crazing}} \cong 40$ mJ/m^2 is the energy per unit area for a new craze to form[152]. The value of σ_{crazing} for the 10 wt% *i*PP/PEP-PEE$_E$-240 blends is approximately 33MPa (d = 100 nm) and this value is close to the matrix yield stress σ_{1y} so that both shear yielding and multiple crazing can occur, consistent with what is observed in the SEM images of the *i*PP/PEP-PEE$_E$-240 blend fracture surface (Figure 4.15). On the other hand, the stress required to initiate crazing during tensile experiments with the 5 wt% *i*PP/PEP blend (d = 0.5 μm) (at a much lower effective strain rate than that during impact testing) is estimated to be σ_{crazing} = 16 MPa, which is lower than the ultimate tensile strength. Therefore, crazing, followed by crack formation, is probably the dominant failure mechanism in the 5 wt% *i*PP/PEP blend during tensile testing. Furthermore, Paul and Bucknall[57] suggest that when $\sigma_{\text{crazing}} << \sigma_{1y}$, the extent of shear yielding is minimal and the cavitated large particles will act as effective flaws, inducing failure of crazes and brittle fracture, which was likely the case during impact testing of the *i*PP/PEP blend.

4.5 Conclusion

We prepared a series of rubbery PEP-PEE$_E$ diblock copolymers by sequential anionic polymerization of isoprene and butadiene followed by catalytic hydrogenation. Composed of *i*PP-miscible and *i*PP-immiscible blocks, the diblock copolymers with M_n = 100 and 240 kg/mol form uniformly dispersed micelles with average diameters of 80 and

100 nm, respectively, when melt blended with *i*PP during melt blending. A block copolymer content as low as 2.5 wt% was sufficient to significantly improve the tensile toughness in the semicrystalline state at room temperature without reducing the elastic modulus or tensile strength of the *i*PP material. Addition of 10 wt% of the diblock copolymer led to a dramatic enhancement in the Izod impact strength. These blends have been studied using TEM, resulting in the identification of shear yielding and multiple crazing of the *i*PP matrix induced by particle cavitation as the most probable mechanism. In contrast, blends prepared with PEP homopolymer containing much larger particles (0.5 μm average diameter) exhibit inferior tensile and impact toughness. The effects of rubber particle size on the susceptibility to cavitation and shear yielding have been evaluated with a well-established model proposed by Bucknall and Paul. Optimal particle size was determined to be in the range of 50-200 nm, consistent with the extraordinary toughness associated with the micelle forming diblock copolymers.

5. Chapter 5: Compatibilization of isotactic polypropylene (*i*PP) and high density polyethylene (HDPE) with *i*PP-PE multiblock copolymers*

5.1 Introduction

More than 70 million metric tons (MMT) of polyethylene (PE) and 50 MMT of isotactic polypropylene (*i*PP) are produced annually in the world, which accounts for approximately two thirds of the global plastics market.[153, 154] Applications of these remarkable materials span packaging and textile products to cutting-edge automotive and aircraft components. They have brought great convenience to people's lives, but have also caused significant environmental pressures due to the combined effects of chemical stability and difficulty in separating these plastics in recycling streams. A recent article in Chemical Engineering News showed that less than 1% of *i*PP and approximately 7% of PE are recycled and most of these plastics end up in landfills or other natural environments.[155] An attractive strategy to increase reuse of these materials is to combine them in a melt compounder and then mold recycled products. However, despite similar chemical

* Reproduced in part with permission from (Xu, J.; Eagan, M. J.; Kim, S.-S.; Pan, S.; Lee, B.; Klimovica, K.; Jin, K.; Lin, T.-W.; Howard, M. J.; Ellison, C. J.; Laponite, A. M.; Coates, G. W.; Bates, F. S. "Compatibilization of isotactic polypropylene (*i*PP) and high density polyethylene (HDPE)with *i*PP-PE multiblock copolymers", *Macromolecules*, American Chemical Society)

structures, *i*PP and PE are thermodynamically incompatible and phase separate at all commercially relevant molecular weights, resulting in products with poor mechanical properties.

Polyolefin compatibilization has drawn tremendous attention in the last three decades,[76-94] with approaches typically divided into two main categories, reactive and nonreactive compatibilization. Reactive compatibilization is conducted by introducing chemically reactive functional groups[76-79, 81-83] that promote grafting or crosslinking reactions with *i*PP and PE, thus stitching together the interfaces between phase separated domains and enhancing the mechanical properties of the blends. Many strategies have been developed for incorporating chemically reactive functional groups in polyolefins. However, this approach has a host of drawbacks, including: (*i*) the reactions must be completed faster than the residence time in blending, greatly limiting the set of viable chemical reactions; (*ii*) the formed chemical bonds need to be stable under processing conditions, i.e. relatively high temperature and high shear; (*iii*) hazardous catalysts with heavy metal components are often needed to promote the reactions, posing health and safety issues; (*iv*) uncontrolled degradation can occur through chain scission; and (*iv*) crosslinking often complicates control over morphology during processing. Furthermore, most reactive compatibilization technologies rely on the formation of irreversible covalent bonds, which compromises recycling of mixed polyolefin waste streams by subsequent blending.

Nonreactive compatibilization, which relies solely on physical processes occurring in the melt compounder, offers numerous advantages over reactive compatibilization. Mixing is conducted by adding premade compatibilizers along with *i*PP and PE in the blending procedure. Ideally the compatibilizers migrate to and stay at the interfaces

separating the separate phases, 'emulsifying' the blend and facilitating the formation of finer dispersions of the minor phase[84, 85]. The compatibilized interfacial layer can also act as a steric barrier in the melt state, preventing domain coalescence and coarsening. Furthermore, this layer can enhance interfacial strength leading to stress transfer from the matrix to the dispersed phase, ideally eliminating interfacial failure, a principal source of macroscopic fracture. [93]. Common compatibilizers include premade block[156-158], tapered block[159] and random copolymers[160]. Random copolymers are generally not superior compatibilizers since they tend to encapsulate the dispersed phase and the morphologies become unstable upon annealing due to a lack of steric hindrance as shown by Lee *et al.*[160]. Molecular weights play a key role in the compatibilization performance of block copolymers (BCPs). Low molecular weight BCPs can diffuse quickly to the immiscible interfaces but may not offer sufficient static stability to prevent coalescence. High molecular weight BCPs, on the other hand, have a very low critical micellization concentration (CMC), resulting in much slower diffusion and compromising the interfacial activity due to micelle formation. The interfacial thickness, $d_I = 2b(6\chi)^{-1/2}$, is rather small in most immiscible polymer blend systems (ca. $d_I < 1$ nm), where b and χ are the statistical segment length and Flory-Huggins interaction parameter, respectively.[161] Relatively small χ parameters are associated with polyolefin mixtures leading to considerably thicker interfaces (ca. 3-5 nm) which can result in melt state entanglements within the mixed interfacial region.

Ethylene-propylene rubber (EPR) [84, 85, 90] and ethylene-propylene-diene monomer (EPDM) rubber[86, 91, 95] are the most widely used compatibilizers for *i*PP and HDPE driven primarily by cheap prices. However, it was found that these additives can form

interpenetrating structures with the minor phase or even phase separate rather than encapsulate the minor phase depending on processing conditions.[162] Moreover, generally more than 10 wt% EPR or EPDM are required to have desirable compatibilization performance, compromising the tensile strength of the materials.

Block copolymers composed of *i*PP-miscible and PE-miscible blocks are more attractive and effective compatibilizers than EPR and EPDM since BCPs are thermodynamically driven to immiscible interfaces as shown by theories[163, 164] and experiments[157, 165, 166] in various blend systems. Earlier works in this field focused on using readily available block copolymers, such as polystyrene-polybutadiene-polystyrene (SBS)[167, 168] and polystyrene-poly(ethylene/butylene)-polystyrene (SEBS)[169] triblock copolymers. Zhang *et al.*[167, 168] found that PE and SBS formed particle, network or combined morphologies in the *i*PP matrix depending on the blending conditions. Although high blend impact toughness can be achieved with certain processing conditions, SBS and SEBS are not ideal compatibilizers due to very limited miscibility with the blend constituents[169]. Olefin block copolymers (OBCs) developed with chain shuttling catalysis[170] are reported to be good compatibilizers for *i*PP/PE. Lin *et al.*[94] carried out a systematic study with a series of *i*PP/PE compatibilizers including a multiblock ethylene-octene copolymer, two random ethylene–octene copolymers, two propylene-ethylene copolymers, and a styrene based block copolymer. They found that the low temperature tensile properties of the blends were greatly improved with 10 wt% OBC, which they attributed to enhanced adhesion between *i*PP and PE domains. But due to the nature of this chain shutting chemistry, the detailed chemical structures of OBCs are quite complicated with various block lengths and different numbers of blocks per chain, which hinders

establishing a fundamental understanding of how molecular structures affect performance with respect to compatibilizer design. The synthesis of *i*PP-PE block copolymers with well-defined molecular weight and architecture has been very challenging. To the best of our knowledge, there is only one report prior to our work[134] by Busico *et al.*[171] describing the synthesis of such BCPs. However, the associated molecular weights were too low for these materials to be used as compatibilizers.

Our recent work demonstrates that -(*i*PP-PE)- block copolymers with well-defined and tunable molecular weights and architectures can be synthesized with a pyridylamidohafnium catalyst,[134] where the notation -(*i*PP-PE)- refers to multiblocks containing 2 or more alternating blocks. This chemistry leads to highly stereoregular *i*PP and linear PE blocks that are both semi-crystalline. These materials display superior interfacial activity, effectively compatibilizing *i*PP/HDPE blends and dramatically improving the blend tensile properties for certain combinations of block molecular weights and molecular architectures. Morphology studies and model peel testing indicate that the improved blend mechanical properties are attributable to enhanced interfacial adhesion between the two phases. In the present study, we expand our preliminary work with pure and melt blended -(*i*PP-PE)- block copolymers focusing on the morphology and tensile and impact mechanical properties in blends containing 1 wt% or less BCP. High temperature spin coating enabled us to prepare very thin (ca. < 100 nm thick) block copolymer films, which were melt molded between commercial *i*PP and HDPE homopolymers in the form of trilayer laminates, imaged by TEM, and characterized for adhesive strength using T-peel test measurements. These experiments reinforce our earlier conclusions regarding the

remarkable interfacial activity of -(*i*PP-PE)- block copolymers in these melt blended plastics.

5.2 Experimental

5.2.1 Materials

As described in Chapter 2, isotactic polypropylene (H314-02Z, MFI = 2.0 g/10 min at 230 °C with 2.16 kg) and high density polyethylene (HDPE) (DMDA8904, MFI = 4.4 g/10 min at 190 °C with 2.16 kg) used in this work were both obtained from the Dow Chemical company. *i*PP-PE diblock, *i*PP-PE-*i*PP-PE tetrablock, and *i*PP-PE-*i*PP-PE-*i*PP-PE hexablock copolymers, referred to collectively as -(*i*PP-PE)-, were synthesized using procedures reported in a previous publication[134]. The synthetic scheme is provided in Figure 5.1 to remind the readers of this powerful chemistry tool to make multiblock copolymers with well controlled molecular weights and tunable architectures.

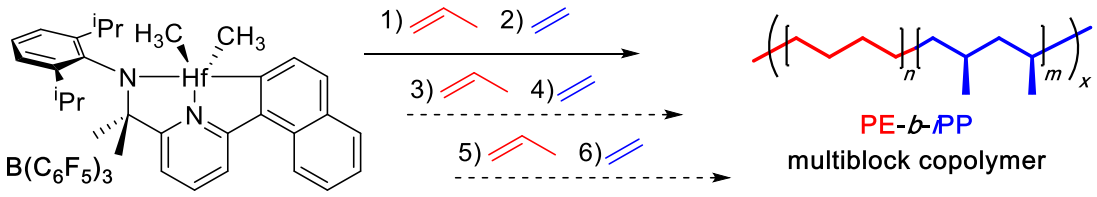

Figure 5.1 Synthetic scheme for the preparation of -(*i*PP-PE)- block copolymers.

5.2.2 Peel testing sample preparation

Preparation of *i*PP and PE Films Polymer pellets of *i*PP and HDPE were compression molded in a 3 cm × 7.5 cm × 0.35 mm stainless steel mold between two Teflon sheets at

180 °C for 5 min under a pressure of 3 MPa followed by water cooling. The film surfaces were subsequently wiped with a Kim-wipe soaked with $CHCl_3$ and air dried for 24 h.

Block Copolymer Thin Film Preparation and Lamination A 4-step thin film fabrication procedure is shown in Figure 5.2. The 1 wt% block copolymer/xylene solution, a freshly cleaved mica substrate (2.5 cm × 2.5 cm) and a glass pipette were held at 120 °C for 1h prior to spin coating. Then the preheated mica substrate was put on the spinner chuck and solution was immediately transferred to the substrate followed by spin coating at 4000 rpm. The resulting block copolymer thin film was carefully floated on distilled water and collected with a HDPE sheet. The film was subsequently dried in air and then in a vacuum oven at 40 °C overnight. For the lamination step, the HDPE/-(*i*PP-PE)- bilayer film was placed in a 3 cm × 7.5 cm × 0.7 mm stainless mold with the BCP side facing up. The *i*PP sheet was placed on top, thereby sandwiching the block copolymer thin film between the HDPE and *i*PP. This trilayer was pressed at 180 °C for 5 minutes under a minimum pressure using a Carver hot press before cooling with water circulation. Once at room temperature, the laminate was removed from the mold and trimmed into 2 cm x 6 cm rectangular samples for peel testing. The control samples, i.e. laminates without a middle adhesive layer, were prepared with the same procedure.

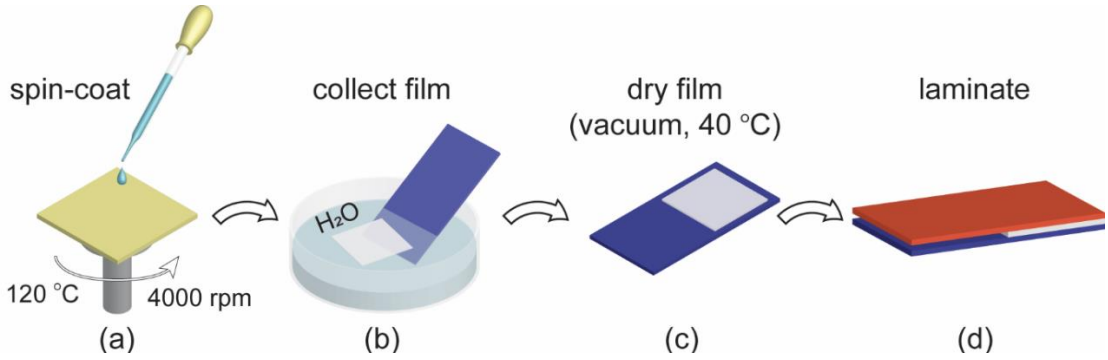

Figure 5.2 Schematic of hot spin coating and lamination of T-peel test specimens (a) Spin coating on a mica substrate with 1 wt% BCP xylene solution. (b) Float BCP thin film on DI water and collect with HDPE film. (c) Dry the film. (d) Laminate *i*PP film onto BCP coated HDPE film with compression molding at 180 °C for 5 min. The tab devoid of BCP is used to load the trilayer laminate in the T-peel test apparatus.

5.2.3 Blend preparation

Pellets of *i*PP and HDPE, and block copolymer powder were compression molded to create a coherent film at 180 °C. The film was then fed into a twin-screw microcompounder operated at 190 °C and 130 rpm with a steady nitrogen purge and a residence time of 8 min. The material was then extruded through a 2.5 mm diameter die and air cooled. As an example, a batch of HDPE/*i*PP compatibilized with 1wt% BCP contains 2.8 g HDPE, 1.2 g *i*PP and 40 mg BCP.

5.2.4 Mechanical testing

Peel Testing A crack was initiated at the interface of the tab without the block copolymer adhesive layer (see Figure 5.2d) and the separated *i*PP and HDPE films were placed in a Shimadzu tensile tester and pulled apart at 10 mm/min while the peel force was measured as a function of peel displacement. The peel strength is reported as the peel force divided by the sample width.

Tensile Testing Extruded blends were compression molded into dumbbell shaped tensile bars (gauge length = 16 mm, gauge width = 3 mm, gauge thickness = 0.6 mm) on a Carver press under ~3MPa of pressure at 180 °C for 5 minutes followed by water cooling. Room temperature tensile tests were performed using a Zwick/Roell tensile tester elongated with a crosshead velocity of 16 mm/min (100% strain/min). Tensile bars were elongated until break and at least five tensile bars were tested for each set.

5.2.5 X-ray scattering

Small angle X-ray scattering (SAXS) and wide angle X-ray scattering (WAXS) were used to characterize the crystal structures of *i*PP and HDPE homopolymers, and -(*i*PP-PE)- block copolymers. Polymers were pressed into 0.5 mm thick films and placed on Kapton tapes after cooling. The room temperature measurements were conducted at Argonne National lab using beamline 5-ID-D with a 17 *keV* radiation energy (wavelength = 0.729 Å) and a sample-to-detector distance of 2 m (WAXS) and 8.5 m (SAXS). Data were collected on a CCD area detector with an exposure time of 1 s. 2-dimensional scattering patterns were reduced to the 1-dimensional form of intensity versus the magnitude of the scattering wavevector $q = 4\pi\lambda^{-1}\sin(\theta/2)$.

5.3 Results and discussion

5.3.1 Multiblock copolymer

The relevant parameters in the block copolymer synthesis and associated molecular characteristics are summarized in Table 5.1. The polypropylene block molecular weights

were controlled by the monomer to catalyst ratio and full conversion, while the ethylene block molecular weights were controlled by the reaction time t_{rxn} under a constant ethylene feed. The theoretical number average molecular weights M_n (*theo.*) were estimated by dividing the yield by the amount of catalyst, which were close to the values M_n (*tot.*) measured by GPC. Representative GPC traces of the aliquots and final block copolymer products are shown in Figure 5.3. With more blocks incorporated, the traces shifted to smaller retention time, i.e. higher molecular weight, and some broadening was observed due to the precipitation of the insoluble semi-crystalline polymers. The overall dispersity of the block copolymers is relatively narrow ($Đ \leq 1.6$) except for the hexablock $PP_{52}PE_{70}PP_{37}PE_{114}PP_{34}PE_{36}$. The first cooling and second heating DSC traces of the -(*i*PP-PE)- BCPs exhibit crystallization and melting behavior as shown in Figure 5.4 and summarized in Table 5.1. Entries 1-6 in Table 5.1 show single melting temperatures (T_m) around 130 °C, which is close to the T_m of commercial HDPE (131 °C) and lower than the T_m of *i*PP (163 °C). This is due to the regio- and stereoerrors in the polypropylene block as determined by ^{13}C NMR, where the stereoregular pentad content m^4 is 91%[134]. Entries 7-9 list another melting peak besides the one at 130 °C. We suspect that a small degree of tapering (i.e. ethylene incorporation in the propylene block or vice versa) is responsible for the lower melting temperatures. Additionally, multiblock copolymers can exhibit depressed melting temperatures of the crystallizable blocks due to the disturbed crystallization induced by the presence of other amorphous blocks as reported by other researchers[172, 173].

Table 5.1 Synthetic parameters and molecular characteristics of -(*i*PP-PE)- block copolymers. Cat., catalyst; $P_{ethylene}$, ethylene pressure; t_{rxn}, ethylene reaction time; *theo.*, theoretical; *tot.*, total.

Entry	Sample $PP_{kg/mol}PE_{kg/mol}$	Cat. (μmol)	propylene (g)	$P_{ethylene}$ (atm)	t_{rxn} (min)	Yield (g)	M_n (*theo.*) (kg/mol)	M_n (*tot.*) (kg/mol)	$Đ$ (M_w/M_n)	T_m (°C)
1	$PP_{24}PE_{31}$	75	1.5	2	3	3.3	44	55	1.32	132
2	$PP_{60}PE_{80}$	30	2	2.7	4	4	134	139	1.4	126
3	$PP_{73}PE_{50}$	30	2.3	2.7	5	3.9	130	123	1.29	131
4	$PP_{103}PE_{113}$	20	1.5	5.4	2	3.8	191	217	1.43	134
5	$PP_{36}PE_{20}PP_{34}PE_{24}$	25	1.0, 1.0	1.4	4, 4	3	120	113	1.38	124
6	$PP_{60}PE_{80}PP_{75}PE_{90}$	30	2.0, 2.0	2.7	4, 4	8.5	283	306	1.29	126
7	$PP_{73}PE_{120}PP_{167}PE_{141}$	50	4.0, 4.0	5.4	1.5	15.8	316	502	1.58	108, 129
8	$PP_{100}PE_{81}PP_{113}PE_{108}$	25	2.5, 2.5	2.7	4	9.2	368	402	1.64	104, 131
9	$PP_{52}PE_{70}PP_{37}PE_{114}PP_{34}PE_{36}$	30	1.0, 1.0, 1.0	5.4	1, 1, 1	6.2	207	345	1.84	74, 127

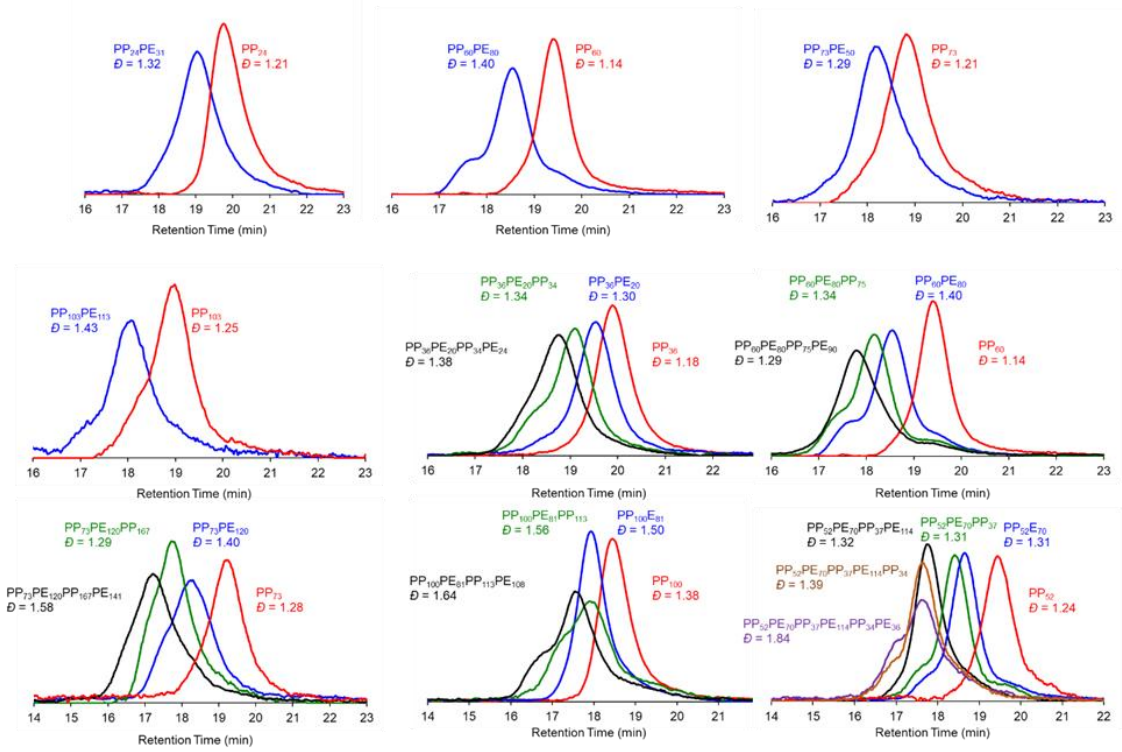

Figure 5.3 SEC traces of GPC aliquots and final PE/iPP block copolymer products presented in Table 5.1.

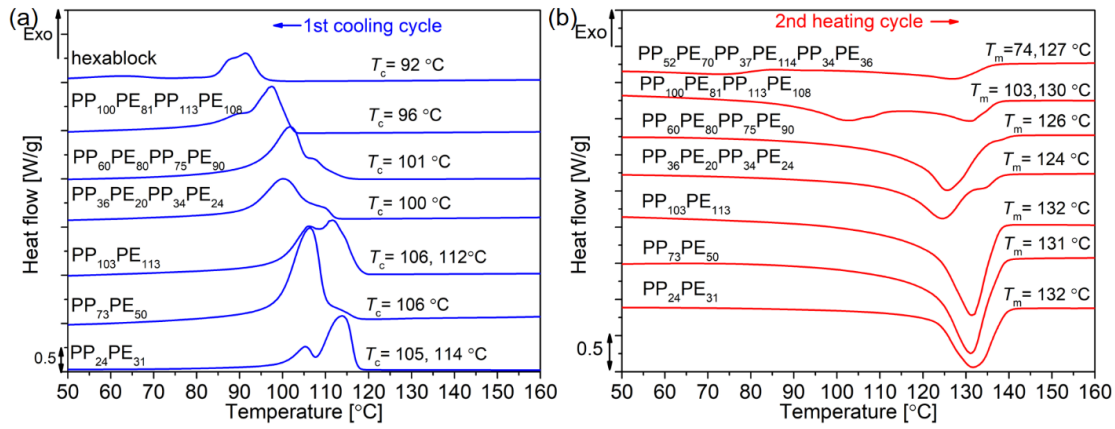

Figure 5.4 DSC traces of (a) the first cooling cycle and (b) the second heating cycle of *i*PP-PE block copolymers at a cooling/heating rate of 10 °C/min. The curves were shifted vertically for clarity.

To further probe the semi-crystalline nature of these BCPs, we conducted wide angle (WAXS) and small angle (SAXS) X-ray scattering experiments on two diblocks ($PP_{73}PE_{50}$ and $PP_{103}PE_{113}$), two tetrablocks ($PP_{36}PE_{20}PP_{34}PE_{24}$ and $PP_{100}PE_{81}PP_{113}PE_{108}$), and the commercial HDPE and *i*PP homopolymers as shown in Figure 5.5. In Figure 5.5(a), the characteristic Bragg peaks associated with the *i*PP monoclinic phase (i.e. (1 1 0), (0 4 0) and etc.)[174] and two dominant peaks due to the PE orthorhombic phase ((1 1 0) and (2 0 0))[175] are observed in the WAXS patterns from the homopolymers and the BCPs, demonstrating that both the polypropylene and polyethylene blocks crystallize. With increasing BCP molecular weight, the peak intensities decreased, which is consistent with our observations of suppressed crystallization in DSC. In the SAXS profile (Figure 5.5(b)), the commercial *i*PP and HDPE exhibit broad peaks with local maximum intensities at q_{max} corresponding to the interlamellar spacings. The average interlamellar spacings d_l for HDPE and *i*PP are calculated to be 25 and 16.4 nm respectively using the Bragg equation $d_1 = \frac{2\pi}{q_{max}}$. The diblock copolymers $PP_{73}PE_{50}$ and $PP_{103}PE_{113}$ show narrower peaks and

lower q_{max} values than those of the two homopolymers, indicating larger average interlamellar spacings (d_l = 34 and 43 nm, respectively). However, from our previous rheological studies[134], we know that the block copolymers are ordered at temperatures above the T_m. The q_{max} of $PP_{73}PE_{50}$ and $PP_{103}PE_{113}$ could be assigned as either the domain spacing d_s between the block copolymer lamellae or the interlamellar spacings d_l of the PP and PE crystals. That q_{max} of $PP_{103}PE_{113}$ is smaller than q_{max} for $PP_{73}PE_{50}$ suggests that the peak is associated with the domain spacing which would be expected to scale as $d_s \sim N^{2/3}$. However, crystallization and a lack of scattering contrast between *i*PP and PE prohibit us from drawing firm conclusions in this regard. The SAXS peaks from $PP_{36}PE_{20}PP_{34}PE_{24}$ and $PP_{100}PE_{81}PP_{113}PE_{108}$ are very broad, indicating a relatively dispersed set of crystal lamellae thicknesses probably due to the convolution of d_l and d_s, likely further complicated by morphological irregularity due to the tetrablock architecture. The melt and solid state microstructures of these block copolymers will be further investigated in the future by small-angle neutron scattering (SANS) after selectively deuterium labeling the PE blocks.[176, 177]

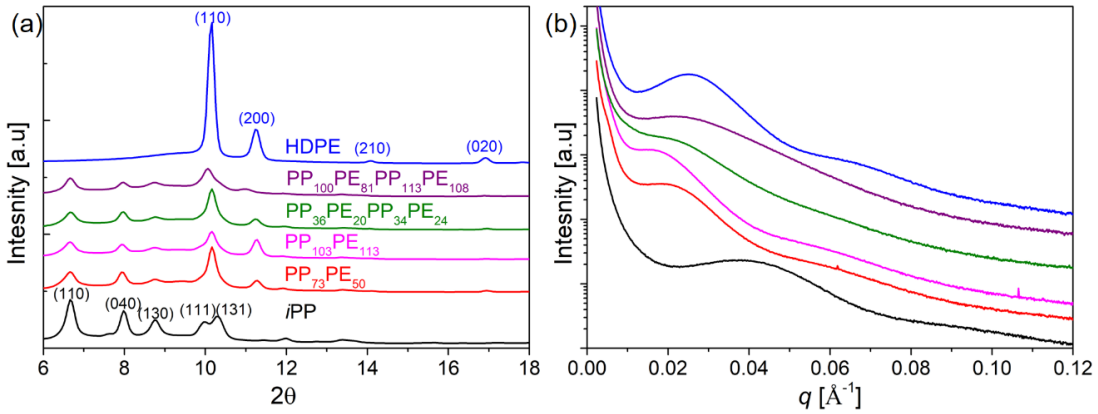

Figure 5.5 (a) wide angle X-ray scattering (WAXS) and (b) small angle X-ray scattering (SAXS) profiles of HDPE, *i*PP and -(*i*PP-PE)- BCPs. Curves are shifted vertically for clarity. The y-axis (intensity) for WAXS is a linear scale while that for SAXS is a log scale.

Representative TEM micrographs of the neat HDPE/*i*PP 70/30 blend and this composition mixture compatibilized with 1 wt% and 0.5 wt% $PP_{73}PE_{120}PP_{167}PE_{141}$ along with the corresponding histograms of size distribution fitted to log-normal distributions are displayed in Figure 5.6. In all cases, the darker continuous phase is HDPE while dispersed *i*PP appears as brighter droplet domains.

Size analysis was performed on at least 300 droplets for each blend by calculating the equivalent diameter of an individual droplet based on $d_i = 2(\frac{A_i}{\pi})^{1/2}$ where A_i is the area that is measured with ImageJ. With 1 and 0.5 wt% $PP_{73}PE_{120}PP_{167}PE_{141}$, the average diameter dropped from 2.2 to 1.1 and 1.6 μm respectively, and droplet shapes became less ellipsoidal compared to the neat blend. The morphologies of HDPE/*i*PP 70/30 blends compatibilized with other -(*i*PP-PE)- BCPs at 0.5 wt% loading were also studied using TEM as shown in Figure 5.7. $PP_{36}PE_{20}PP_{34}PE_{24}$ and $PP_{73}PE_{120}PP_{167}PE_{141}$ have very similar compatibilization performance, decreasing droplet size from 2.2 to approximately 1.7 μm while $PP_{60}PE_{80}PP_{75}PE_{90}$ and the hexablock $PP_{52}PE_{70}PP_{37}PE_{114}PP_{34}PE_{36}$ brought the size

down to around 1 μm. The blend morphologies and corresponding size distribution histograms with 0.2 wt% BCP are provided in Figure 5.8. At this lowest concentration, particle sizes were all close to that of the neat blend, and the sizes were too dispersed to be fitted to log-normal distributions.

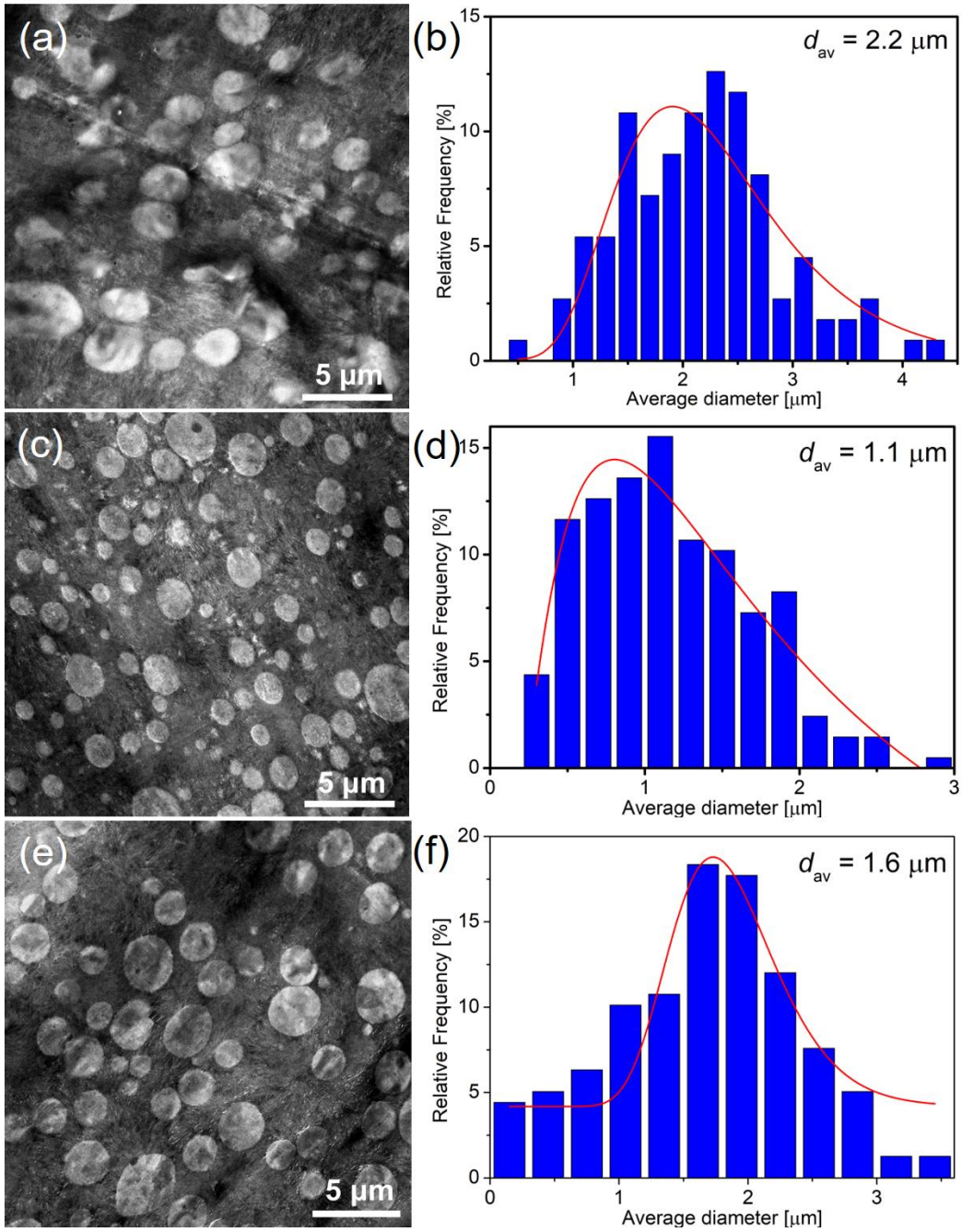

Figure 5.6 TEM images and corresponding droplet size distributions of (a, b) HDPE/*i*PP 70/30 uncompatibilized blend and HDPE/*i*PP 70/30 blend compatibilized with (c, d) 1 wt% and (e, f) 0.5% of $PP_{73}PE_{120}PP_{167}PE_{141}$.

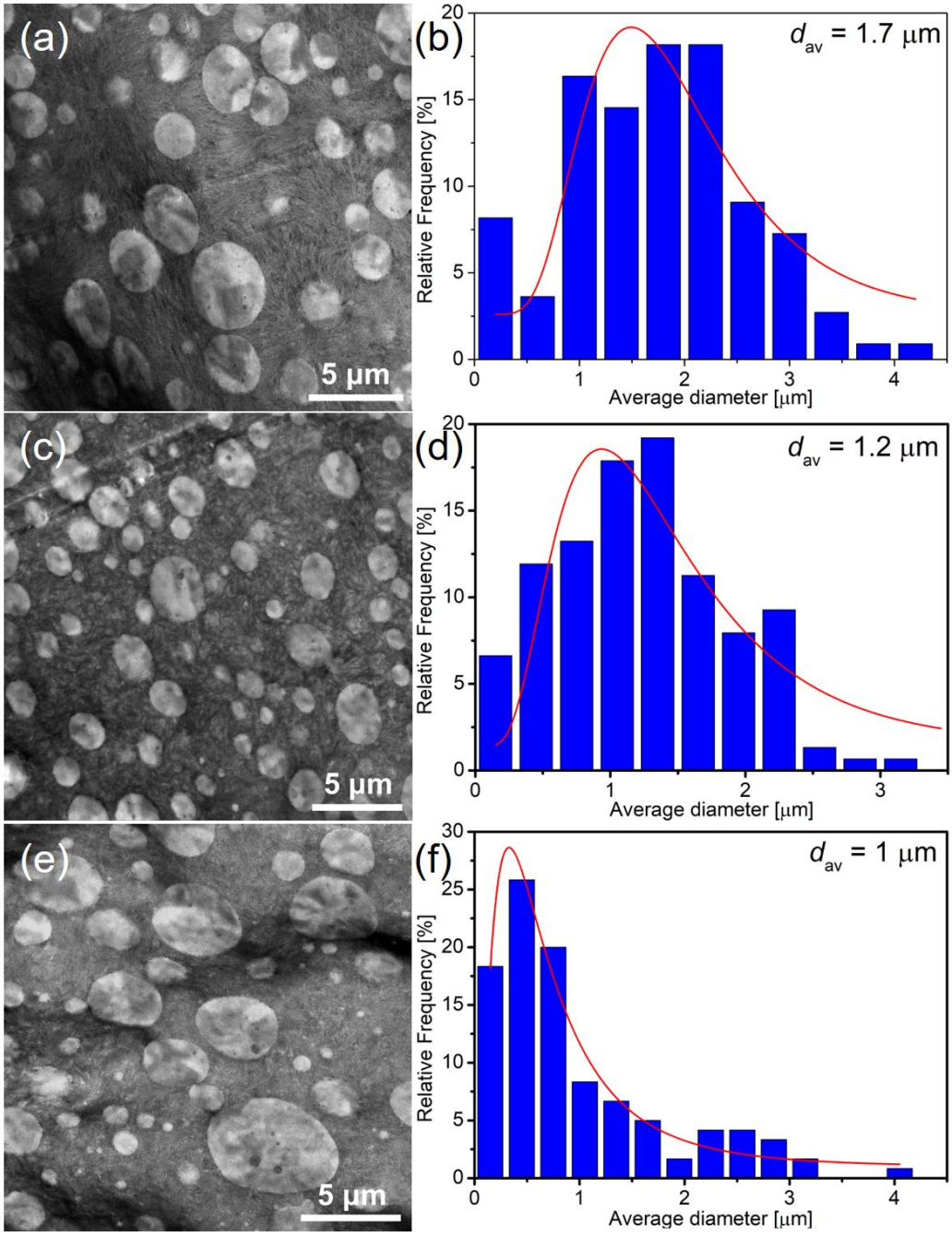

Figure 5.7 TEM images and corresponding droplet size distributions of PE/*i*PP 70/30 blend compatibilized with 0.5 wt% of (a, b) $PP_{36}PE_{20}PP_{34}PE_{24}$, (c, d) $PP_{60}PE_{80}PP_{75}PE_{90}$ and (e, f) $PP_{52}PE_{70}PP_{37}PE_{114}PP_{34}PE_{36}$.

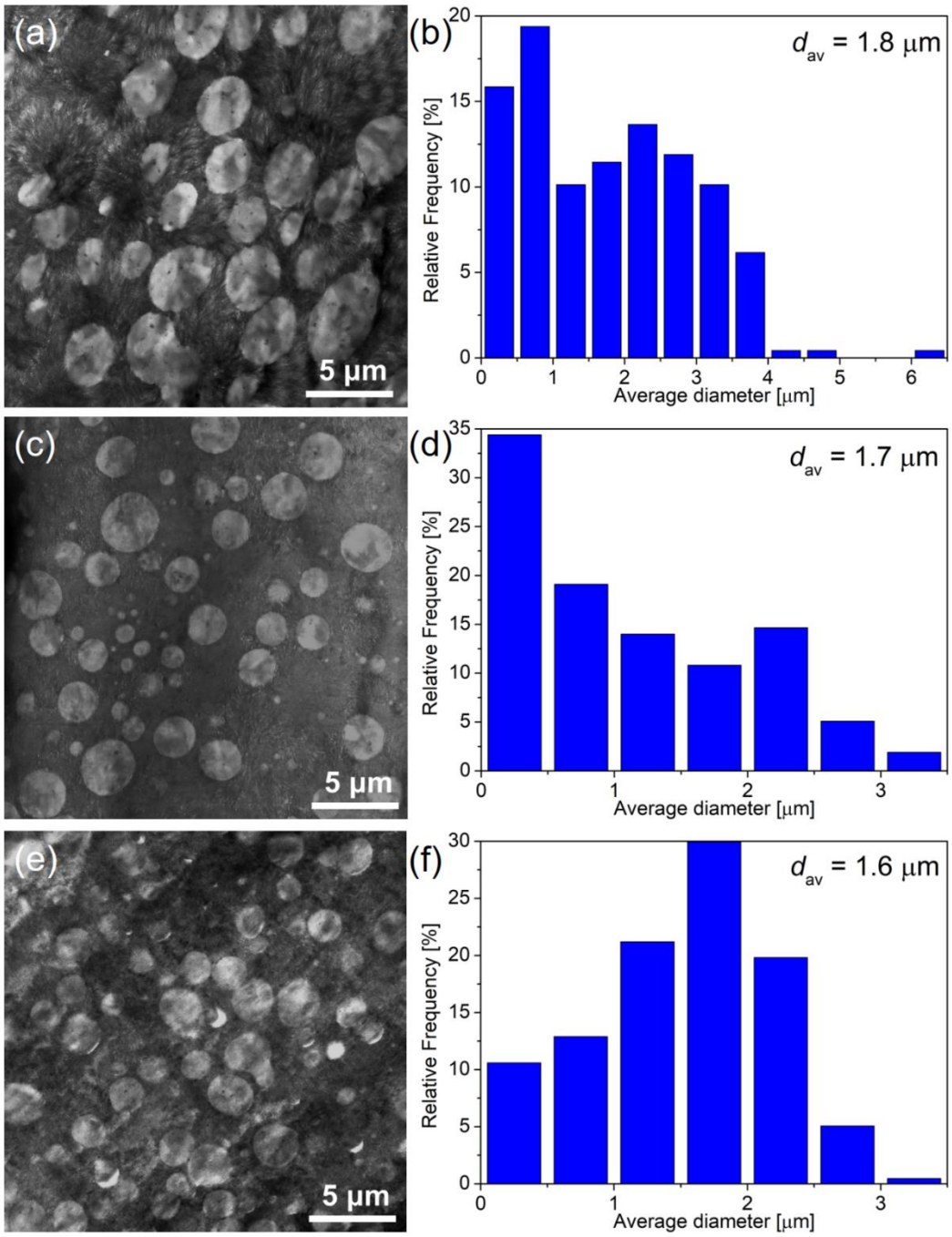

Figure 5.8 TEM images and corresponding droplet size distributions of PE/*i*PP 70/30 blend compatibilized with 0.2 wt% of (a),(b) $PP_{36}PE_{20}PP_{34}PE_{24}$, (c),(d) $PP_{60}PE_{80}PP_{75}PE_{90}$ and (e), (f) $PP_{52}PE_{70}PP_{37}PE_{114}PP_{34}PE_{36}$.

Droplet sizes are plotted versus block copolymer concentration in Figure 5.9. As expected, the droplet size decreases with increasing BCP concentration, reaching 0.5 μm

and 0.8 μm with 5 wt% $PP_{36}PE_{20}PP_{34}PE_{24}$ and $PP_{60}PE_{80}$ respectively as reported in our previous work[134]. This size reduction is attributable to reduced interfacial tension with the BCP layers 'emulsifying' dispersed droplets; steric barrier effects of these layers also effectively prevent coalescence as discussed in the Introduction. We interpret the bimodal-like particle size distributions for the 0.2 wt% tetrablock blends shown in Figure 5.8 as evidence of inhomogeneous coverage of the *i*PP droplets at this low concentration. Comparing different compatibilizers at 0.5% loading, the higher molecular weight tetrablock (and the hexablock) seems to perform better than the lower molecular weight one, as opposed to equivalent emulsification across all the multiblocks at 1 wt%, although we hesitate to draw general conclusions based on this limited set of BCP samples.

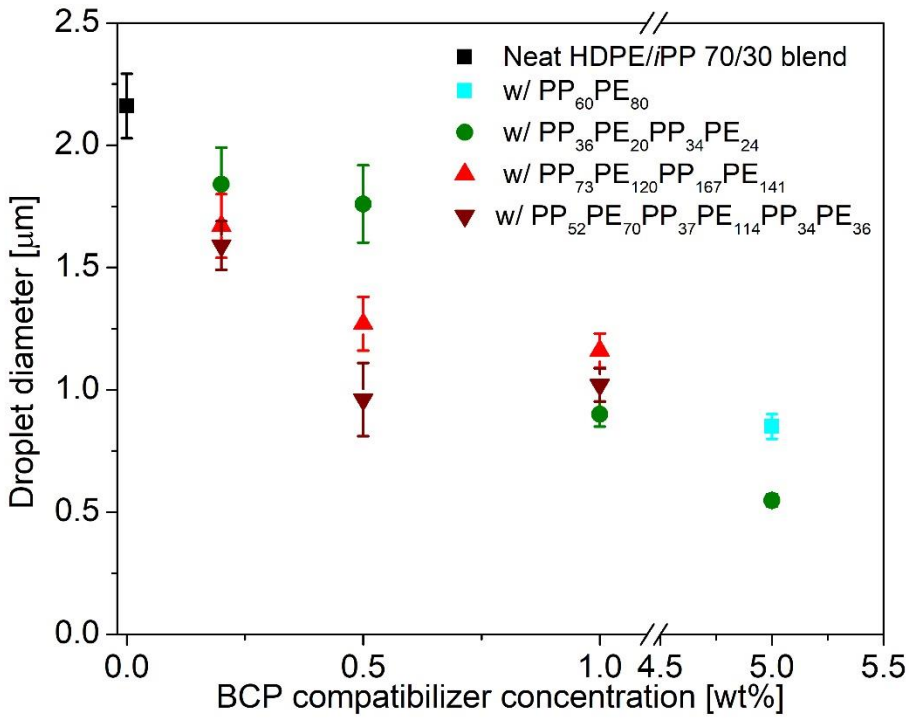

Figure 5.9 Droplet diameter of *i*PP in PE matrix in PE/*i*PP 70/30 blends as a function of block copolymer compatibilizer concentration (0.2-5 wt%). The error bars are 95% confidence intervals. Note the break on the x-axis from 1-4.5.

The average layer thickness l of the block copolymers present at the domain interfaces can be estimated using the following equation assuming that *i*PP, HDPE and -(*i*PP-PE)- have the same densities and all the BCPs go to the interface:

$$l = r\{[(\phi_{PP} + \phi_{BCP}) / \phi_{PP}]^{1/3} - 1\} \quad (1)$$

where r is the radius of the dispersed *i*PP particles, and ϕ_{PP} and ϕ_{BCP} are the volume fractions of *i*PP and BCP, respectively. In the case of 0.2 wt% BCP compatibilizer, the average radius r is approximately 1 μm resulting in l = 2.2 nm. Taking $PP_{36}PE_{20}PP_{34}PE_{24}$ as an example, the radius of gyration of the PE_{20} block is approximately 6.5 nm ($R_g = b(N/6)^{1/2}$ where N = 357 is the number of segments and b = 8.4 Å is the PE statistical segment length based on a statistical segment volume v = 118 $Å^3$)[29]. This is three times larger than the calculated layer thickness. From this we conclude that at 0.2 wt% BCP, the immiscible interfaces are not covered with a dense layer of BCP chains, consistent with our conjecture regarding the broad distribution of particle sizes. Nevertheless, as shown below, the 0.2 wt% blends exhibit much better mechanical properties than the unmodified *i*PP/HDPE blends indicative of some block copolymer at the interfaces.

The surface coverage of block copolymers can be investigated by calculating the number of BCP chains/nm^2 Σ using the equation described by Mackoso *et al.*[157] if we assume all the BCP goes to the interface:

$$\Sigma = \frac{\text{chains / vol}}{\text{interface area / vol}} = \frac{N_A \rho \phi}{M S_{SP}} \quad (2)$$

where ρ, ϕ, M are the density, volume fraction and molecular weight of the block copolymers, respectively, and N_A is Avogadro's number. S_{SP} is the interfacial area per unit volume which can be calculated from d_{vs} using the following set of equations:

$$d_{vs} = \sum^{N} d_i^3 / \sum^{N} d_i^2$$
$$S_{SP} = 6\phi_P / d_{vs} \quad (3)$$

where d_{vs} is a particle volume over surface area average diameter, d_i is the individual particle diameter, and ϕ_P is the volume fraction of the dispersed phase.

If we use HDPE/*i*PP 70/30 blend compatibilized with 1 wt% $PP_{73}PE_{120}PP_{167}PE_{141}$ as an example, d_{vs} and S_{SP} are calculated to be 1.6 μm and 1.13 μm^{-1}. This leads to Σ value of 8.5×10^{-3} chains/nm^2 ($\rho \approx 0.8$ g/cm^3 in the melt state). While for HDPE/*i*PP 70/30 blend compatibilized with 0.5 wt% $PP_{73}PE_{120}PP_{167}PE_{141}$, the Σ value is calculated to be 5.8×10^{-3} chains/nm^2.

Assuming a dense monolayer of BCP in the interface, we can then calculate the maximum block copolymer concentration Σ_m. If we only consider a symmetric diblock copolymer for example $PP_{103}PE_{113}$, the thickness of the monolayer is half of the lamellar spacing, $d_l/2$ in the ordered state.

$$\Sigma_m = \frac{\text{thickness of BCP monolayer}}{\text{volume of one BCP chain}} = \frac{d_l / 2}{M / \rho N_A} \quad (4)$$

And for $PP_{103}PE_{113}$, d_l = 43 nm, which gives a Σ_m value of 4.8×10^{-2} chains/nm^2. This further supports our argument of partial coverage due to insufficient BCP concentration.

5.3.2 Tensile properties

Representative stress-strain curves for the neat HDPE/*i*PP 70/30 blend and compatibilized blends with 1, 0.5 and 0.2 wt% BCPs are provided in Figure 5.10. The HDPE and *i*PP homopolymers are very tough, breaking at more than 800% and 300% strain, respectively, as shown in Figure 5.11. However, the 70/30 blend material is very brittle with an elongation at break of just 10% as illustrated in the inset of Figure 5.10(a). In this limit failure is driven by *i*PP particle debonding from the matrix due to poor interfacial adhesion as seen in SEM images of the surface of a fractured specimen (see the 'beehive' structure in Figure 5.12). This leads to rapid void growth to a critical size and subsequent macroscopic fracture. The blend compatibilized with the low molecular weight diblock copolymer $PP_{24}PE_{31}$ was as brittle as the neat blend indicative of poor interfacial adhesion as reported previously.[134] On the other hand, 1 wt% of the tetrablock and hexablock compatibilizers produced blends with extraordinary toughness, evidenced by strains at break of more than 400%. We attribute this behavior to a combination of good interfacial coverage and mechanically strong interfaces (see below) that provide for stress transfer between the matrix and particles. As the BCP concentrations were lowered, the strain at break of the compatibilized blends also dropped. Yet amazingly, just 0.2 wt% of multiblock polymer produced greater than 100% strain at break (Figure 5.10(c)), although the tensile properties were somewhat more scattered (see Figure 5.13), which we attribute to the aforementioned limited and possibly non-uniform interfacial coverage.

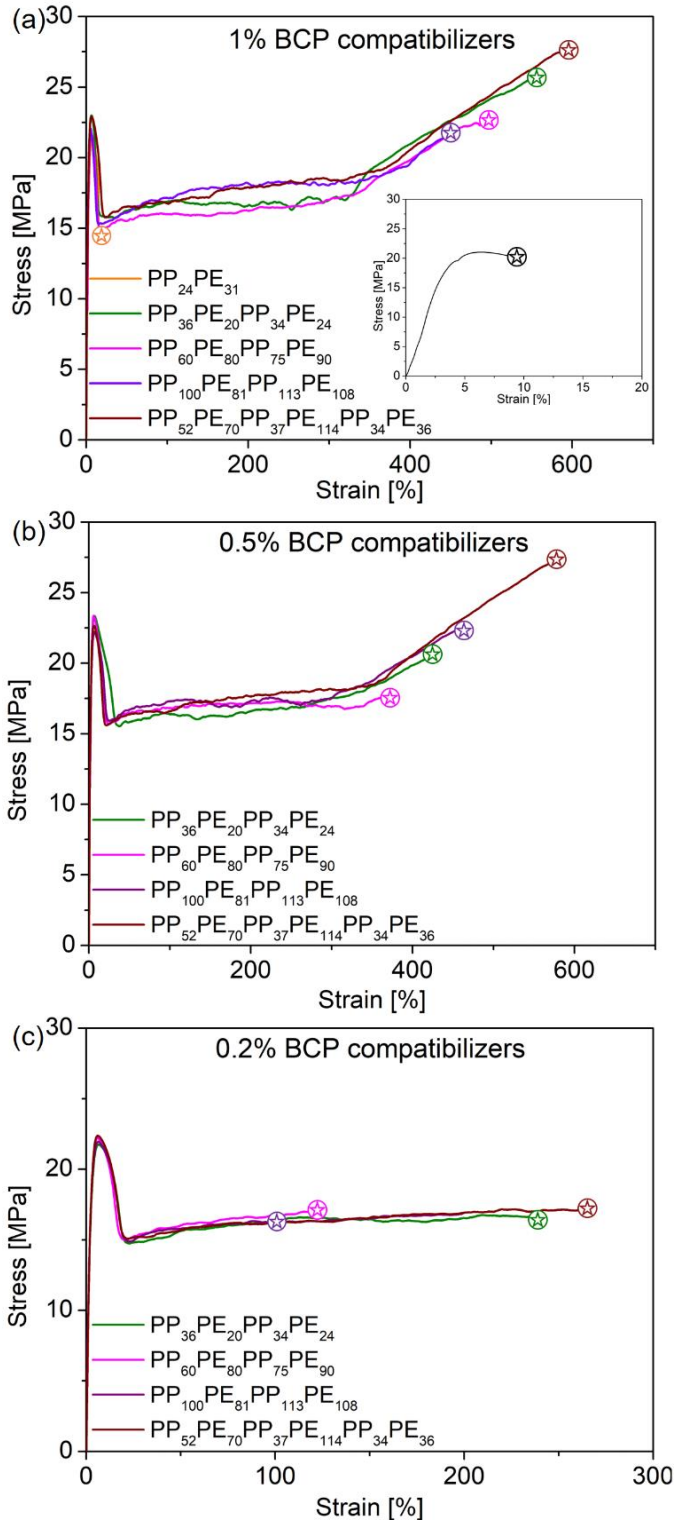

Figure 5.10 Representative stress-strain curves of PE/*i*PP 70/30 blends compatibilized with (a) 1 wt%, (b) 0.5 wt% and (c) 0.2 wt% block copolymers. The inset in (a) shows the stress-strain curve of the uncompatibilized blend.

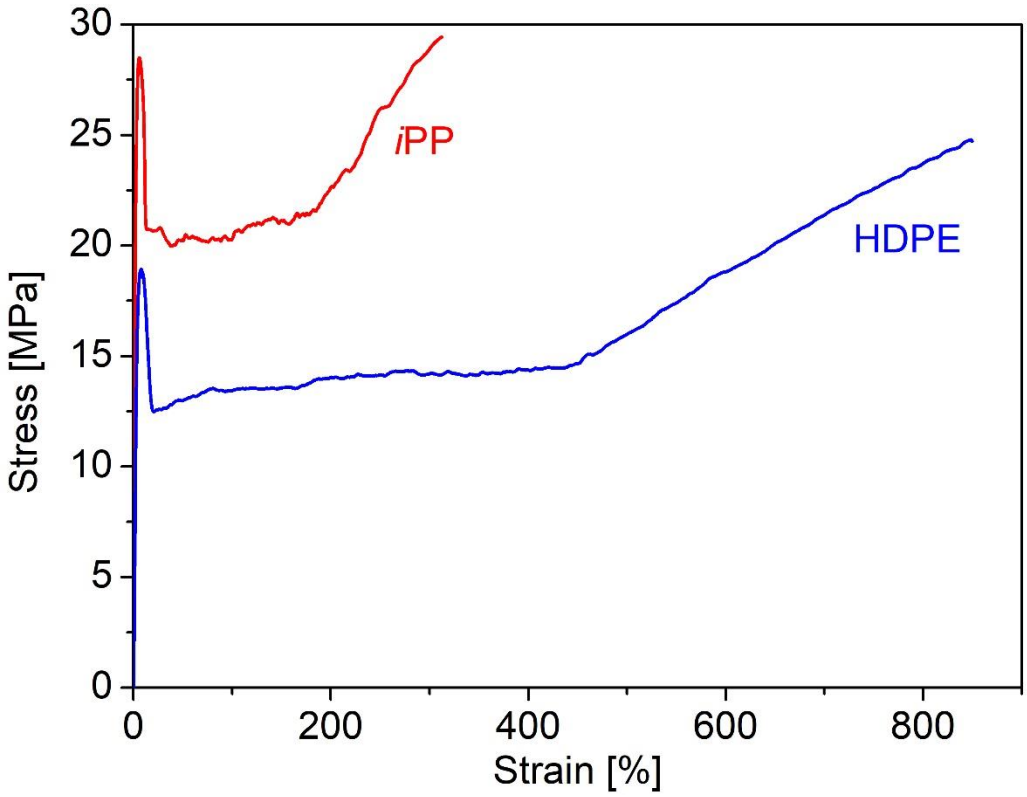

Figure 5.11 Representative stress-strain curves of *i*PP and PE homopolymers

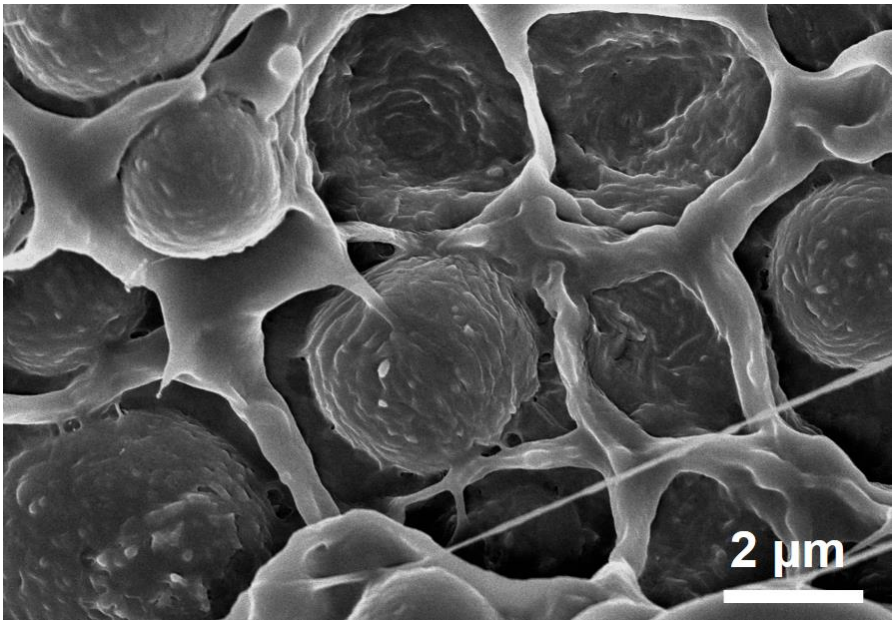

Figure 5.12 SEM image of fracture surface of neat PE/*i*PP 70/30 blend after tensile testing

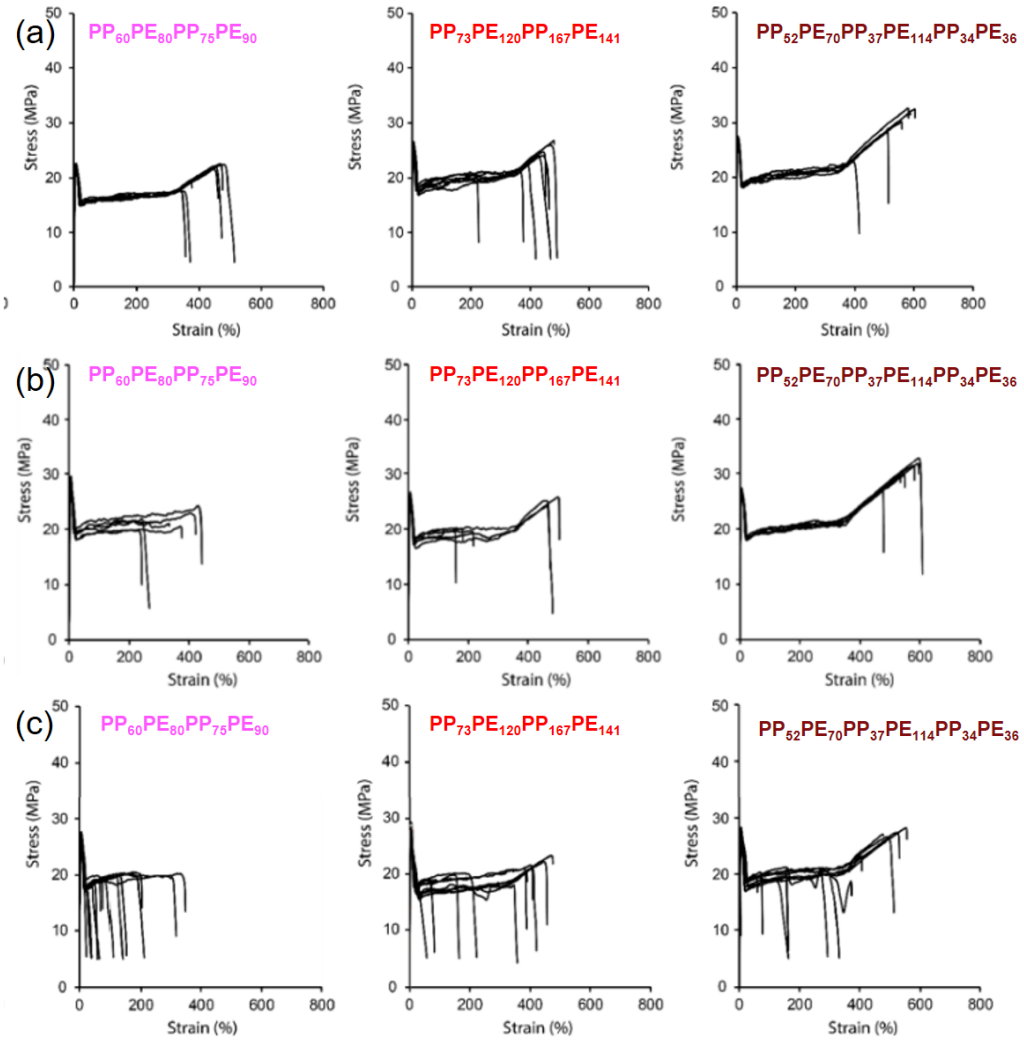

Figure 5.13 Individual stress-strain curves of PE/*i*PP 70/30 blends compatibilized with (a) 1 wt%, (b) 0.5 wt% and (c) 0.2 wt% of $PP_{60}PE_{80}PP_{75}PE_{90}$, $PP_{73}PE_{120}PP_{167}PE_{141}$ and $PP_{52}PE_{70}PP_{37}PE_{114}PP_{34}PE_{36}$ block copolymers.

Figure 5.14 compares a_b as a function of BCP concentration for several diblock and tetrablock copolymers, and a hexablock copolymer. The $PP_{24}PE_{31}$ diblock imparts little toughness at all concentrations, while $PP_{60}PE_{80}$ produces a marginally tough material at 1 wt% loading and a tough plastic at 5 wt%. All three multiblock copolymers result in a tough product with optimal strain at break realized with just 1 wt%, and significant ductility with as little as 0.2 wt% of the additive. The $PP_{52}PE_{70}PP_{37}PE_{114}$ $PP_{34}PE_{36}$ hexablock

copolymer is the most effective toughening agent achieving on average 550% strain at break at just 0.5 % loading.

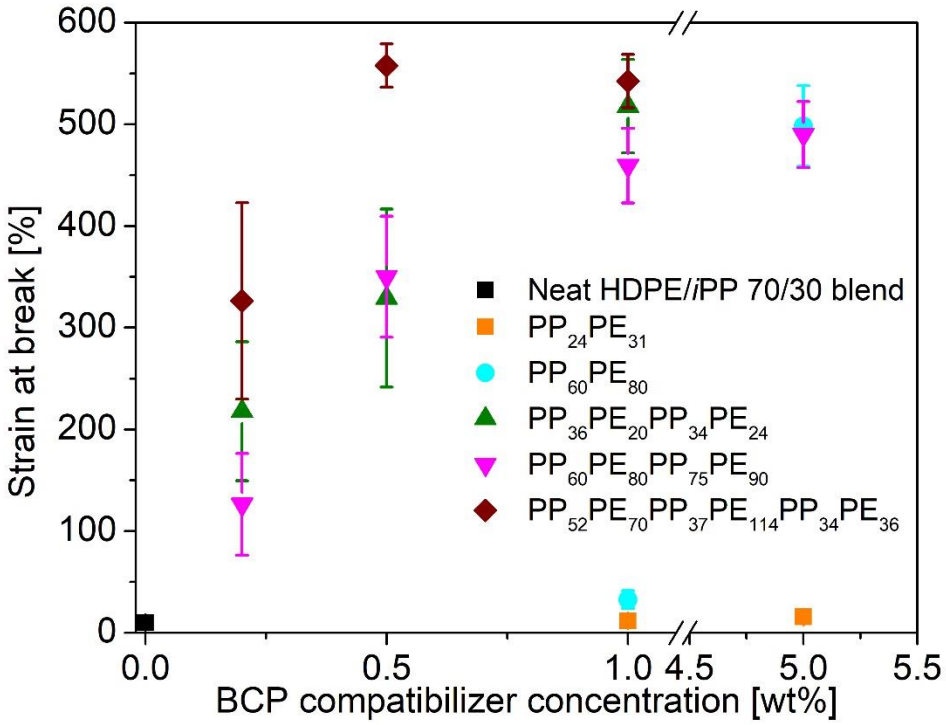

Figure 5.14 Strain at break of compatibilized PE/*i*PP 70/30 blends as a function of block copolymer compatibilizer concentration (0.2-5 wt%). The error bars are 95% confidence intervals. Note the break on the x-axis from 1-4.5.

5.3.3 Impact properties

Izod impact testing has been employed to further evaluate the mechanical properties of the BCP modified blends using the tetrablock copolymer $PP_{100}PE_{81}PP_{113}PE_{108}$ as a representative additive. The impact strengths of the HDPE and *i*PP homopolymers, neat 70/30 and 30/70 blends, and the corresponding compatibilized blends with 1 wt% BCP are displayed in Figure 5.15. The impact strengths of the homopolymers are very close to literature values.[178, 179] As seen in other studies, the impact strengths of the

uncompatibilized neat blends are lower than those of the matrices.[85, 180, 181] With merely 1 wt% BCP, we have recovered the impact strength of pure HDPE in the PE/*i*PP 70/30 blend, greatly outperforming the neat blend. D'Orazio *et al.*[85] reported a comparable impact performance with the addition of 10 wt% ethylene-propylene copolymers. Less improvement was achieved in the PE/*i*PP 30/70 blend although the BCP modified material does outperform the neat blend. This is not surprising as the more brittle *i*PP is the majority phase; as reported in various publications, improving the impact toughness of *i*PP requires greater amounts of compatibilizer.[182-184]

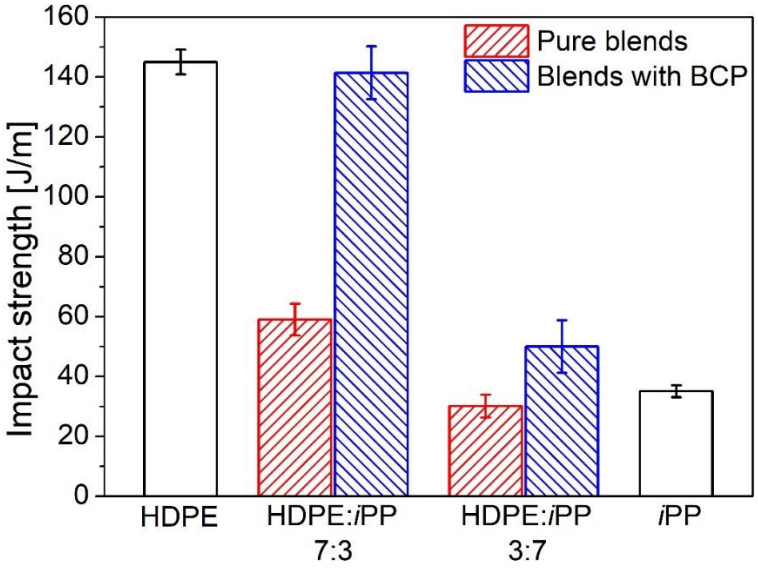

Figure 5.15 Notched Izod impact strength of HDPE, HDPE/*i*PP 70/30 blend, HDPE/*i*PP 70/30 blend, *i*PP and corresponding blends compatibilized with 1 wt% $PP_{100}PE_{81}PP_{113}PE_{108}$. The error bars are 95% confidence interval calculated from at least 5 specimens.

We investigated the failure modes of the neat and compatibilized PE/*i*PP 70/30 blend by imaging the fracture surface with SEM after impact testing, as shown in Figure 5.16. The fracture surface of the neat blend is much smoother than that of the

compatibilized one. At increased magnification, cavities formed by the *i*PP particles that detached from the matrix are clearly evident. Significantly, the detached particles are not deformed, consistent with our hypothesis of weak interfaces that do not transfer stress from the HDPE matrix to the *i*PP particles (also see Figure 5.12). We conclude that brittle behavior is due to the interfacial failure and subsequent large crack formation. Additional support for this conclusion is provided by wavelike structures in the low-magnification image in Figure 5.16 (c), and stretched fibrils emanating from the fracture surface in the high-magnification image in Figure 5.16(d) for the compatibilized blend, indicative of extensive plastic deformation of the HDPE matrix. Apparently, the strong interfaces prevent interfacial failure and allow the matrix material to deform in the same manner as the pure HDPE, which results in the same impact strength (Figure 5.15).

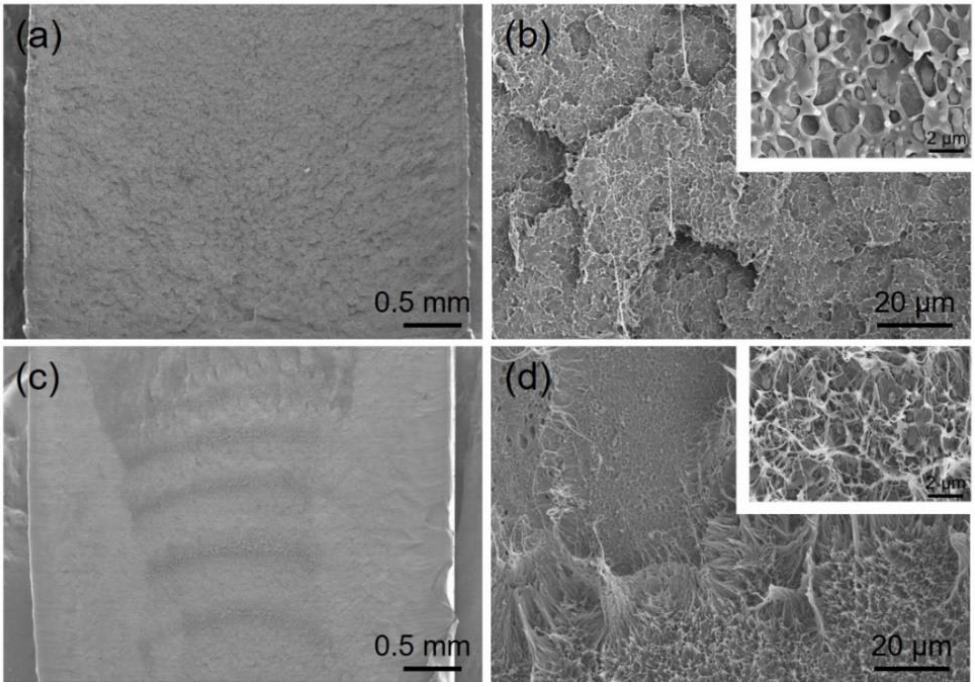

Figure 5.16 SEM micrographs of fracture surfaces after impact testing of (a), (b) uncompatibilized *i*PP/PE 30/70 blend and (c), (d) PE/*i*PP 70/30 blend compatibilized with 1 wt% $PP_{100}PE_{81}PP_{113}PE_{108}$.

5.3.4 Adhesion of HDPE/BCP/*i*PP laminates

In order to independently evaluate our conclusions regarding interfacial strength we performed T-peel adhesion tests with trilayer laminates containing a thin layer of the BCPs shown in Figure 5.5. Diblocks $PP_{73}PE_{50}$ and $PP_{103}PE_{113}$, and tetrablocks $PP_{36}PE_{20}PP_{34}PE_{24}$ and $PP_{100}PE_{81}P_{113}PE_{108}$ were fabricated into thin films using high temperature spin coating (See Figure 5.2 for the schematic and Figure 5.17 for images taken during spin coating). It is worth noting that we attempted to prepare thin films from $PP_{24}PE_{31}$ with the same method, however, the films easily broke into pieces in the transfer step, making it impossible to fabricate multilayer laminates. The average thickness of the thin film can be controlled by adjusting the spin casting conditions.[185] T-peel test measurements were performed using BCP film thicknesses between about 50 and 100 nm as determined by atomic force microscopy (AFM, see Figure 5.18). This represents more than one domain period for the microphase separated BCPs used in this study based on our analysis of the SAXS patterns shown in Figure 5.5.

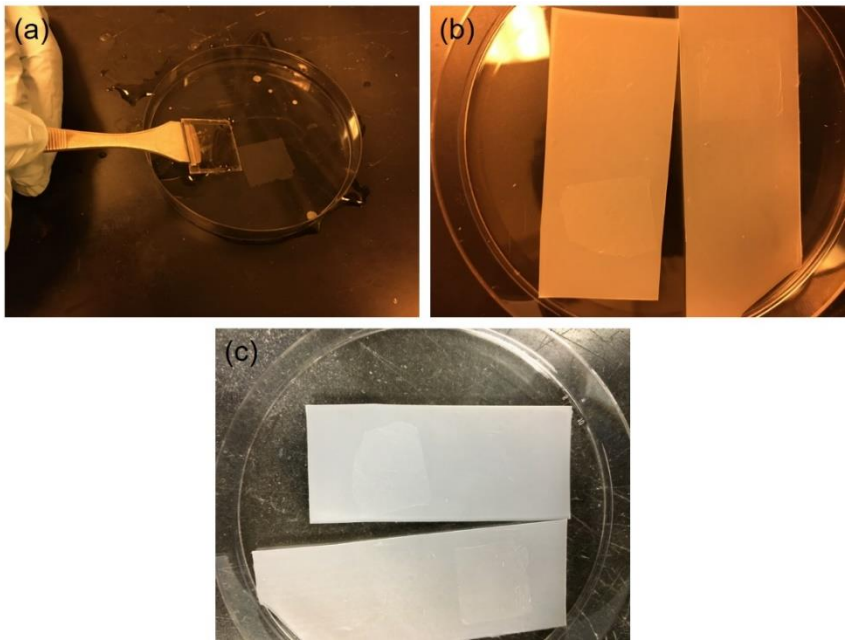

Figure 5.17 Pictures demonstrating the fabrication of block copolymer thin films composed of (a) spin coating and floating on DI water, (b) collection with a HDPE film and (c) drying in air and then vacuum oven.

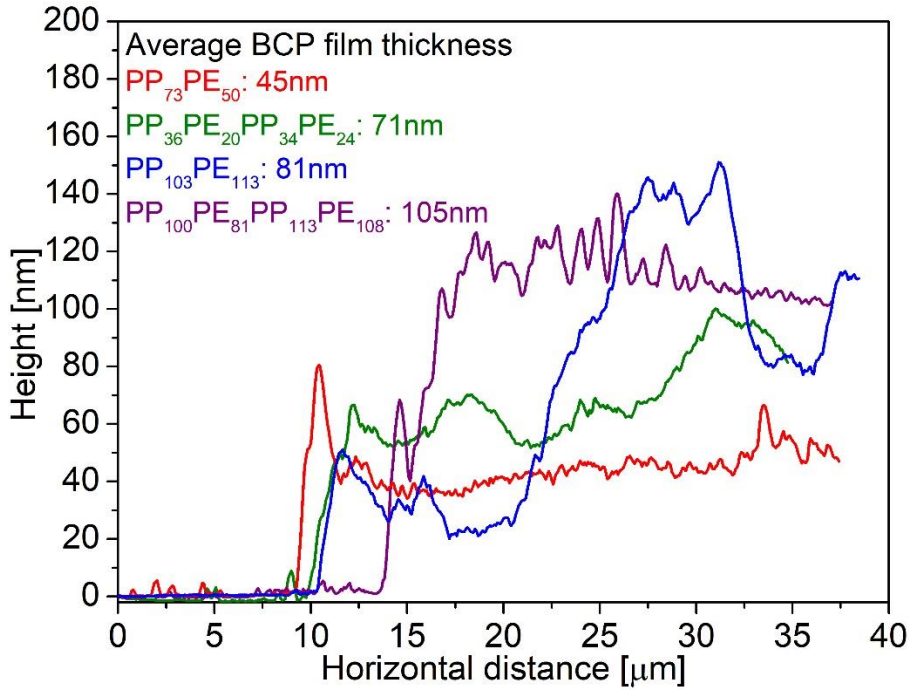

Figure 5.18 Height profile of spin-coated block copolymer thin films measured by AFM.

We employed TEM to probe the morphology of the trilayer laminates. Unfortunately, the thin (≤ 100 nm) BCP films could not be clearly resolved. Therefore laminates were prepared in the same manner as the ones employed in peel testing, but the block copolymer film was deliberately made about 10 times thicker by using a 2 wt% BCP solution and rotation speed of 1000 rpm in the spin casting process. Representative TEM images obtained from a HDPE/$PP_{103}PE_{113}$/*i*PP trilayer are presented in Figure 5.19. Based on the blend morphology images (Figure 5.6 and Figure 5.7), we know that HDPE takes up more RuO_4 and appears darker, which allows us to identify the homopolymer layers in Figure 5.19. Clearly $PP_{103}PE_{113}$ forms a distinct uniform layer between the HDPE and *i*PP films with an average thickness of about 700 nm, confirming the integrity of the process used to make the trilayer laminates. Crystallization at both the *i*PP/BCP and HDPE/BCP interfaces is evident in the higher magnification image, with some indication that the crystalline texture propagates through the interfaces, suggesting cocrystallization of the BCP and homopolymer.

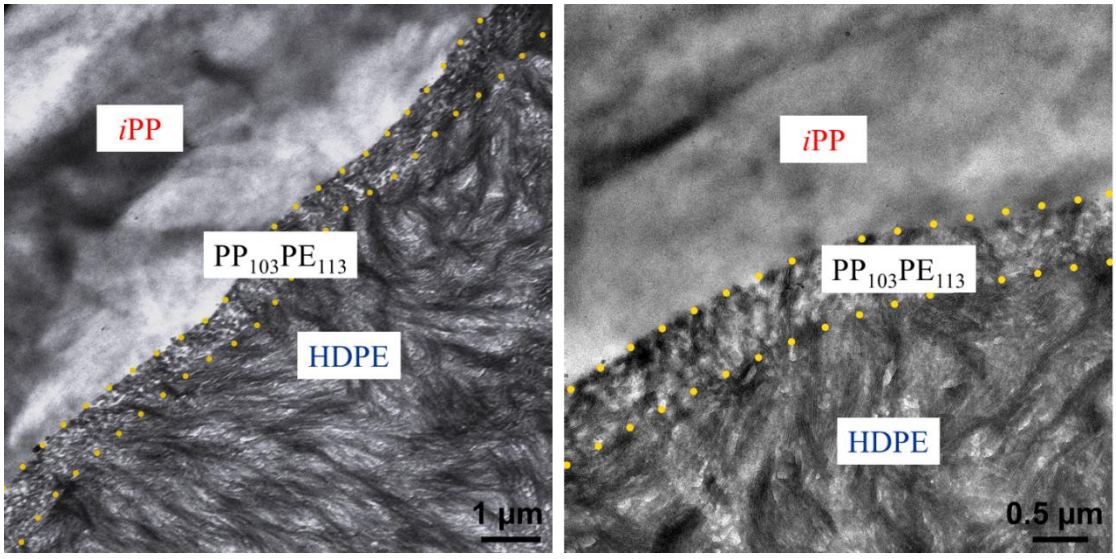

Figure 5.19 TEM micrographs of a *i*PP/$PP_{103}PE_{113}$/PE trilayer film with yellow dots highlighting the two interfaces.

The peel strengths of HDPE/*i*PP and HDPE/BCP/*i*PP laminates are shown in Figure 5.20. Laminates without the middle BCP adhesive layer can be peeled apart very easily with a peel strength of 0.2 N/mm (black curve in Figure 5.20). With a thin layer of $PP_{73}PE_{50}$ (red curve) steady state displacement is reached with an 'equilibrium' peel strength value of approximately 2.5 N/mm. Middle layers of $PP_{103}PE_{113}$, $PP_{36}PE_{20}PP_{34}PE_{24}$ and $PP_{100}PE_{81}PP_{113}PE_{108}$ (blue, green and purple curves, respectively) do not peel apart. After full extension of the tabs, which accounts for the initial increase in the peel force, the HDPE film yields then draws and breaks at 6 N/mm. These results are virtually indistinguishable from our previous findings based on 100 μm thick block copolymer adhesive layers.[134]

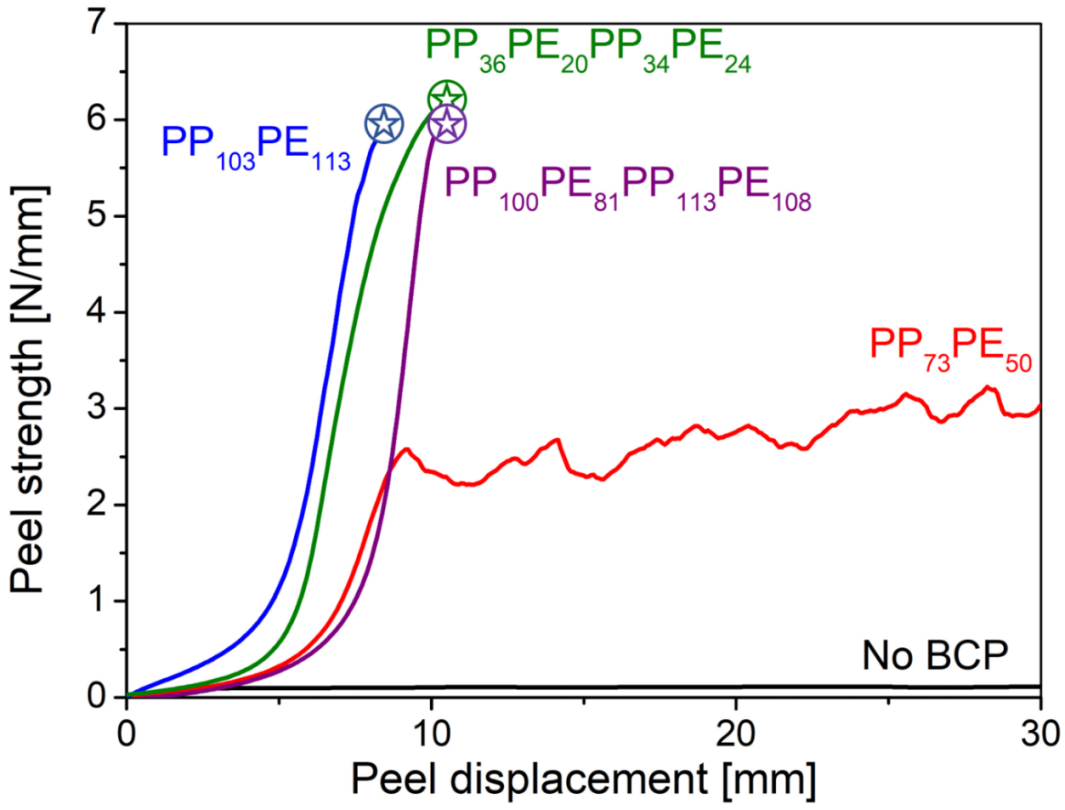

Figure 5.20 Peel strength of iPP/HDPE laminates (2 cm wide, 6 cm long, 0.35 mm thick) with and without BCP layer. The stars indicate failure or yielding of the HDPE film. The average film thickness is provided in Figure 5.18.

We examined the *i*PP and HDPE surfaces without a BCP layer and with the $PP_{73}PE_{50}$ adhesive layer after peel testing using SEM (See Figure 5.21 and Figure 5.22 respectively). Both surfaces from the bilayer homopolymer laminate were very smooth with barely distinguishable small features (~ 1 μm) at high magnification, consistent with the low peel strength. On the other hand, peeling apart the block copolymer containing trilayer produced *i*PP and HDPE film surfaces that were both rough and decorated in places with grossly deformed fibrils, which accounts the higher peel strength since such plastic deformation consumes energy. Obviously, there were no peel surfaces to inspect with specimens that exhibited HDPE film failure.

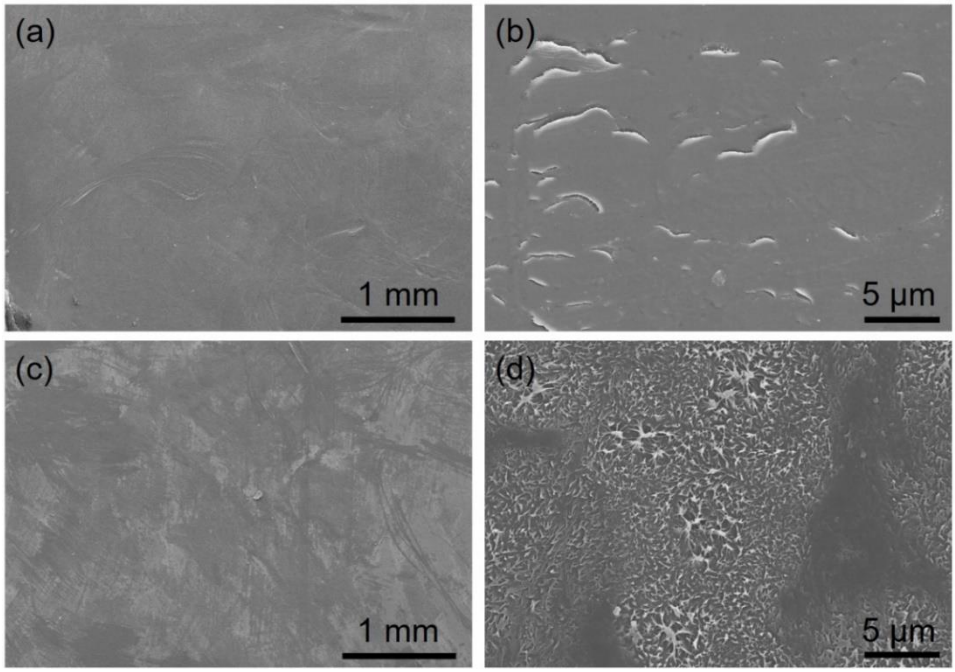

Figure 5.21 SEM micrographs of the peel surface of (a) HDPE and (c) *i*PP laminates without block copolymer adhesive layer after testing. Higher-magnification images are provided in (b) and (d) for the HDPE and *i*PP respectively.

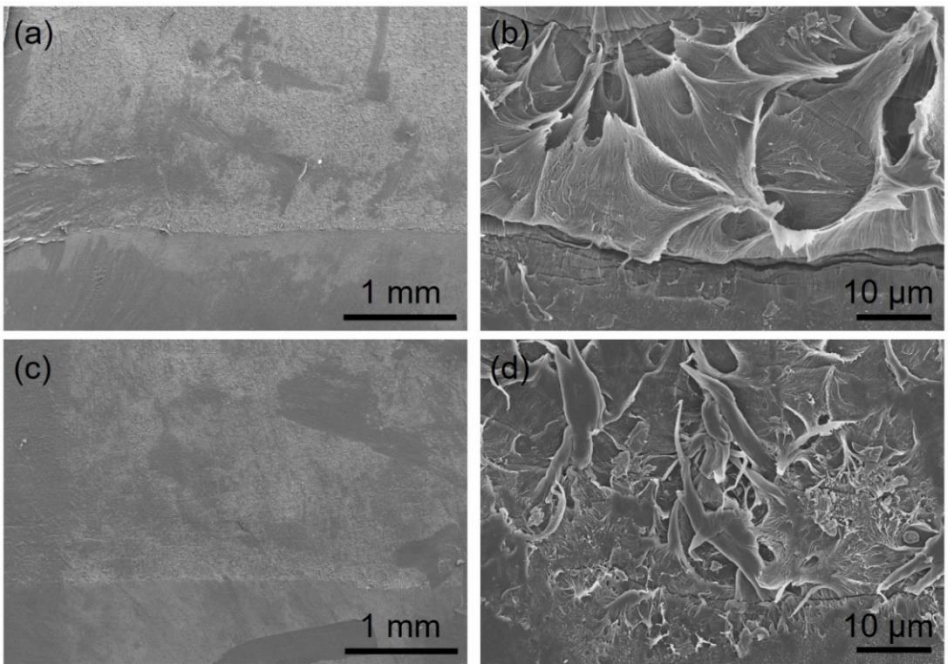

Figure 5.22 SEM micrographs of the peel surface of (a) HDPE and (c) *i*PP laminates with an adhesive layer of 50nm-thick $PP_{73}PE_{50}$ after testing. Higher-magnification images are provided in (b) and (d) for the HDPE and *i*PP respectively.

5.3.5 Adhesion models

The adhesion results obtained with the sub-100 nm thick BCP films are quantitatively consistent with those reported earlier based on much thicker (ca. 5-100 μm) binding layers. Taken together, the two sets of peel test data and the blend mechanical property results obtained over a range of low block copolymer concentrations (0.2 to 5 wt%) reinforce the interfacial adhesion models proposed in our preliminary publication.[134] Chaffin *et al.*[186] first showed that non-crystalline components (presumably highly branched and/or low molecular weight chains) tend to accumulate at the interface in bilayer homopolymer laminates formed from Ziegler-Natta *i*PP and HDPE homopolymers, thus rendering poor peel strength as seen in Figure 5.20. Block copolymers apparently displace such material from the interface between phase separated *i*PP and HDPE; this mechanism should be operative in both laminates and phase separated blends. We have characterized this action as being analogous to the role played by welding flux, which shields surfaces from oxidation during the joining of two metals.[187] However, in order to create a robust joint, the block copolymer must engage mechanically with the homopolymer.

Previously we proposed two molecular level mechanisms to explain the trilayer peel test results, both of which rely on the semicrystalline nature of the components. Here we briefly summarize these models; see Figure 2 of Eagan *et al.*[134] for illuminating illustrations. Long *i*PP-PE diblocks bridge the interface and co-crystallize with homopolymer crystalline lamellae thus locking together the opposing phases leading to high peel strength. Short diblocks fail to engage mechanically due to an inability to sufficiently integrate with the crystalline homopolymer, resulting in block pull-out and weak adhesion. High molecular weight *i*PP-PE-*i*PP-PE tetrablock copolymers will also

cocrystallize but carry the added advantage that half the *i*PP and PE blocks are flanked by the opposing blocks. Hence, even at relatively low molecular weights, simple entanglement of the internal blocks with chain-folded loops of the semicrystalline homopolymer lamellae at the interface, in conjunction with microdomain crystallization, creates a strong mechanical coupling. Here we note that the relatively thick interface associated with phase separated PE/*i*PP melts ($d_I \approx 4$ nm)[57] and low entanglement molecular weights ($M_{e,PE} = 1$ kg/mol[127] and $M_{e,iPP} = 6$ kg/mol[188]) promote such interfacial entanglement. We believe these models can be extrapolated to the limit of sub-monolayer interfacial BCP coverage associated with the HDPE/BCP/*i*PP blends. Even for the most concentrated case we have studied, 5 wt% BCP (0.5 μm diameter *i*PP droplets, Figure 5.9), equation 1 predicts a maximum interfacial layer thickness $l \approx 14$ nm; this assumes all the BCP lies at the interface. Based on our interpretation of q^* for $iPP_{103}PE_{113}$ this represents roughly half a domain period. In general, the blends we have studied will have at most monolayer BCP coverage. Nevertheless, sub-monolayer coverage should function in the same way as the thicker BCP films as illustrated in Figure 5.23. The short diblocks should entangle with the homopolymers chains in the melt state since the molecular weights are well above the entanglement molecular weights M_e of HDPE and *i*PP. However, upon cooling, the blocks are not long enough to reach and co-crystallize with the homopolymer crystalline domains (shaded layers in Figure 5.23) hence will be prone to easy chain pull out (See Figure 5.23(a)). When the block lengths go above a threshold value (~ 70 kg/mol)[134], they can integrate with the homopolymer crystalline domains resulting in strong adhesion (Figure 5.23(b)). The importance of interfacial entanglement and co-crystallization is highlighted in a recent study by Jordan *et al.*[189], who demonstrated a reduction in peel strength with the

addition of oligomers to HDPE/*i*PP laminates. Additional support for this model is provided by a study of polystyrene (PS) and polyethylene (PE) adhesion mediated by PS-PE block copolymer by Benkoski *et al.*[190] who found that when the PE block molecular weight $M_n \leq 30$ kg/mol, chain pullout was the predominant mechanism and that maximum adhesion was achieved only when PE block molecular weight was more than 85 kg/mol. These limits coincide with the critical value observed in our own study.[134] We argue that the radius of gyration (R_g) of the PE and *i*PP blocks must be greater than the amorphous thickness at the interface (presumed to be of order 10 nm) to penetrate into the crystalline layer and co-crystallize, which requires molecular weights of 48 and 87 kg/mol for PE and *i*PP respectively.

Even though the block molecular weights of the low molecular weight tetrablocks such as $PP_{36}PE_{20}PP_{34}PE_{24}$ are below the critical molecular for bridging the amorphous regions, the molecular architecture ensures a fraction of the internal blocks can form 'anchor sites' and at least half of them can entangle with the homopolymers chains in the form of loops. Upon cooling, crystallization would trap and lock these entangled loops in place, effectively stitching the interface and significantly enhancing the interfacial strength as illustrated in Figure 5.23(c). High molecular weight tetrablocks such as $PP_{100}PE_{81}PP_{113}PE_{108}$, benefit from both interlocked entanglements and co-crystallization (Figure 5.23(d)).

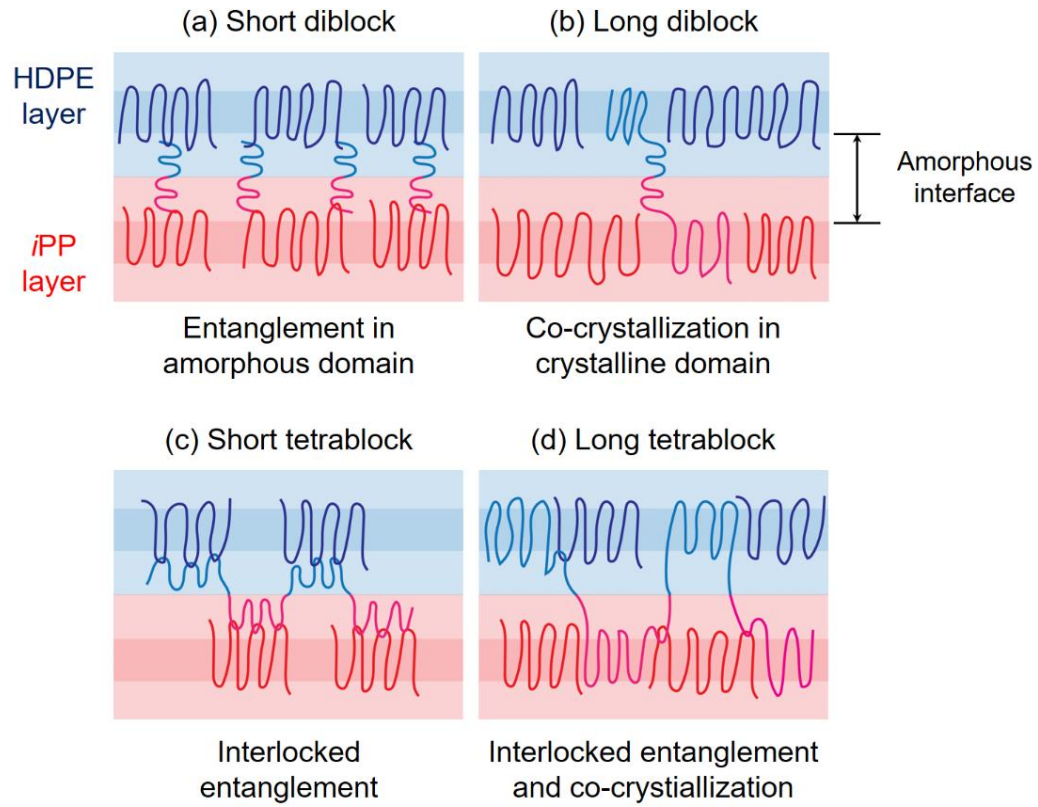

Figure 5.23 Schematic illustrations of proposed mechanisms of adhesion in phase separated *i*PP/BCP/PE blends in the limit of low concentrations of (a) short diblock, (b) long diblock, (c) short tetrablock and (d) long tetrablock copolymers.

5.4 Summary and conclusions

We have investigated a series of -(*i*PP-PE)- diblock, tetrablock, and hexablock copolymers with various molecular weights and architectures, synthesized using a powerful catalyst system, as HDPE/*i*PP compatibilizers. These materials offer superior compatibilization performance. Melt blending 1 wt% of the BCPs with a 70%/30% blend of commercial HDPE and *i*PP homopolymers reduces the average diameter of the dispersed droplets from 2 to 1 μm, increases the strain at break in tension from 10% to more than 500% and elevates the impact toughness to a level equivalent to pure HDPE. This

remarkable toughening effect, attributed to enhanced interfacial strength, remains evident down to BCP concentrations as low as 0.2 wt%.

Interfacial adhesion was further studied by molding thin BCP films (≤ 100 nm), fabricated by high temperature spin coating, between layers of HDPE and *i*PP and subjecting these trilayer laminates to T-peel testing. Laminates formed with low molecular weight diblocks separate by adhesive failure. High molecular weight diblocks, and tetrablocks containing low or high block molecular weights, produce a strong interfacial joint between the homopolymer layers that exceeds the cohesive strength of the HDPE film. Molecular level mechanisms involving block-homopolymer co-crystallization at the interfaces, augmented by interlocked entanglements in tetrablock and multiblock copolymers, are proposed to account for both the blend toughening and laminate adhesion results.

These findings offer exciting opportunities for combining the world's top two polymers by melt blending plastics recovered from waste streams, followed by remolding into mechanically superior products.

6. Chapter 6: Summary and outlook

The work presented in this thesis has provided new insights on polyolefin mixing thermodynamics and utilized this fundamental knowledge to design block copolymer (BCP) toughening agents to improve the mechanical properties of *i*PP and *i*PP/PE compatibilizers that can potentially revolutionize the plastic recycling industry. In this final chapter, we first summarize the main results and conclusions of the previous chapters (Section 6.1) and then propose future research directions with some preliminary attempts and results to further advance our understanding in this field (Section 6.2 and 6.3).

6.1 Thesis summary

The toughening of *i*PP has drawn enormous research interest and blending second phase modifiers, such as rubbers, rigid particles and hybrid core-shell particles has been the most widely used technique to improve mechanical properties[38, 40, 43, 45, 59, 101, 102]. In this rich portfolio of toughness modifiers, truly effective ones are in great demand. A large amount of rubber (> 20 wt%) is often required to generate desirable toughness, greatly compromising the high strength and optical clarity of pure *i*PP material. We aim to come up with new solutions that significantly improve the toughness and meanwhile maintain

the other desirable material properties. Block copolymers have been extensively used in our group to toughen thermoset epoxies[66, 67, 69, 71, 73] and recently applied in glassy thermoplastic polylactide (PLA)[74]. They offer many great advantages: the block copolymers are dispersed in the form of nano-sized micelles, scattering less light and therefore maintaining transparency; the micelle shapes are tunable from spherical, cylindrical to vesicles by changing the block molecular weights and composition, offering opportunities to study the fundamental toughening mechanism of various blend morphologies; most importantly, the block copolymers are superior toughening agents, dramatically enhancing the toughness with as little as 5 wt% BCP addition. Inspired by previous studies, we pursued this unprecedented toughening method in semicrystalline matrices.

Commercially available block copolymers have been utilized in *i*PP toughening, such as styrene-butadiene-styrene (SBS) triblocks[51] and olefin block copolymers (OBCs)[53, 191]. Unlike the specially designed BCPs, they phase separate and form large domains in the *i*PP matrix, similar to common rubbers, so their performance is only slightly better than traditional rubbers. The block copolymers in our work were strategically designed to possess *i*PP-miscible and *i*PP-immiscible blocks, enabling them to self-assemble into nano-size micelles.

In Chapter 3, we synthesized a series of poly(cyclohexyl ethylene-*ran*-ethylene) (CE) copolymers to match the statistical segment length of *i*PP, which are potentially ideal candidates for the *i*PP-miscible blocks according to conformational asymmetry theory[7]. However, these copolymers turned out to be immiscible with *i*PP while surprisingly were uniformly dispersed as nanoscale droplets. It is well known that χ is composed of an

entropic part χ_S and an enthalpic part χ_H. Matching the statistical segment length minimizes χ_S but there was still a non-neglectable χ_H due to their density difference (i.e. ρ_{CE} is 10% larger). Using rheological measurements and model fitting, we estimated the interfacial tensions between CE copolymers and *i*PP, which were very low owing to the marginal immiscibility imparted by almost zero χ_S and small χ_H. More interestingly, these *i*PP/CE copolymer blends demonstrated great toughness in tensile testing with little loss in the tensile strength and optical clarity. Cavitation induced shear yielding and crazing was the most probable mechanism based on SEM observations. This work provides useful guidance for the design of tough polymer blends. By carefully adjusting the statistical segment length and density mismatches, one can control the blend morphology and prepare blends with great strength, toughness and transparency. Furthermore, this work has advanced our understanding of polyolefin blend mixing thermodynamics and will hopefully stimulate more interest in this field full of opportunities.

In Chapter 4, we chose poly(ethyl ethylene-*ran*-ethylene) (PEE_E) with 70-90% EE content as the *i*PP-miscible block and poly(ethylene-*alt*-propylene) (PEP) as the *i*PP-immiscible block to prepare 'amphiphilic' PEP-PEE_E block copolymers, which are capable of self-assembling into nano-sized micelles. Using TEM and SEM, we found that these block copolymers form micelles as small as 80 nm in diameter. Furthermore, they were very effective in toughening *i*PP, significantly enhancing the tensile and impact toughness and maintaining the high tensile strength with merely 5-10 wt% block copolymer addition. They outperformed the *i*PP blends modified with PEP and the other commercial SBS, SEBS and OBC benchmarks. TEM of the specimens at the yield point revealed very uniformly dispersed nanovoids created by the micelle cavitation and the evidence of

simultaneous shear yielding of the matrix. To explain our observations, we utilized a well-established model of rubber modified blend systems to construct a stress map to connect micelle cavitation and matrix plastic deformation. It was found that there is an optimal range of particle size, i.e. 40-200 nm in diameter, in our blend system to ensure the concurrent occurrence of micelle cavitation and matrix shear yielding. When the particle size is too small (< 40 nm), the cavitation is energetically unfavorable and the matrix plastic deformation is hard to be activated due to the volumetric constraint. On the other hand, if the particle size is very large, crazing starts to compete with shear yielding and the matrix tends to deform by crazing, eventually leading to premature failure, which is the case in the PEP modified blend. This work has demonstrated the great potential of micelle toughening technique in a broader choice of matrix materials and provided practical approaches to preparing blends with a superior mechanical performance by mastering polyolefin mixing thermodynamics and carefully designing 'amphiphilic' block copolymers. Furthermore, the optimal particle size range of *i*PP blends discovered in our work will be a useful guideline to peers working in the same field. To build on what we have also established, I propose more possible toughening approaches by combining micelle toughening and other techniques (i.e. rigid particles) in section 6.2.

In Chapter 5, we were motivated to tackle the plastic recycling problem faced by society. If the current production and waste treatment continue, approximately 12,000 million metric tons of plastic waste is estimated to be accumulated in the landfill or natural environment by 2050.[192] Polyethylene and polypropylene are the top two plastics in the world, making up two-thirds of global production. They have very similar densities, making it extremely challenging to sort them out in the recycling facility. One approach is

to melt compound them together and mold the blends into recycled products. However, PP and PE tend to phase separate and the interfaces are very weak, resulting in very poor blend mechanical properties and little economic incentives to recycle these materials. To make products with equal or higher values, they need compatibilization. We have collaborated with the Cornell University to develop *i*PP-PE block copolymers as PP/PE compatibilizers. With the new catalysts, multiblock (i.e. two blocks to six blocks) copolymers with well-controlled molecular weights and low dispersity have been synthesized. A comprehensive study of molecular weight and architecture effects on the compatibilization performance has been carried out by investigating the morphology, mechanical property and adhesion through TEM, tensile testing and peel testing respectively. In peel testing, it was found that a thin middle layer of diblocks with certain critical block lengths and multiblocks (i.e. tetrablocks and hexablocks) provided such strong adhesion that the PE film broke rather than middle adhesive layer failed. The great improvement in the adhesion also translates into superior blend mechanical properties, improving the strain at break from 10% for the neat blend to more than 400% with only 5 wt% BCP addition in a PP/PE 30/70 blend. Upon further TEM investigation, the PP droplet size decreased from 2.2 μm to as small as 0.5 μm. And at lower BCP compatibilizer concentrations, the multiblocks have better performance than the diblocks, yielding tough blends with just 0.5% addition. To explain this interesting molecular weight and architecture effects, we proposed the following mechanisms. The diblocks need to be long enough to penetrate deeply into the homopolymer interfaces and co-crystallize with them to have high interfacial strengthTetrablocks can effectively entangle with the homopolymer chains in the form of loops, wiggle back and forth multiple times between the two phases and stitch the

immiscible interfaces. These remarkable block copolymers can potentially revolutionize the recycling business since a very little amount is needed to produce blends with great properties. Moreover, this work has shed light on the design of high-performance compatibilizers in semicrystalline blends: entanglements and cocrystallization with the homopolymers are both important factors to consider. There are still many unanswered questions in this work that deserves further investigations and I'll propose some possible directions in section 6.3.

6.2 Synergistic toughening of isotactic polypropylene with block copolymer micelles and rigid fillers

There has been continuous interest in ternary blends of *i*PP, rubber and rigid fillers[47, 50, 193-195]. Besides the rubber incorporation due to their merits in toughening performance, a variety of rigid fillers, including calcium carbonate, silica and clay, are also added because of their low cost and high strength to potentially lead to synergistic toughening effects from both components and achieve an optimum balance of strength and toughness. A recent work by Li *et al.*[72] has shown that block copolymer micelles and rigid fillers (i.e. graphene) demonstrate a significant synergistic toughening performance with soft micelle cavitation and rigid particle debonding triggering epoxy matrix plastic deformation and then crack pinning and deflection mechanism because of the present rigid particles. The PEP-PEE_E block copolymer micelles in our work are proven to be much more effective toughening agents than commonly used rubbers, i.e. EPR and EPDM rubbers. On the other hand, the work by Thio *et al.*[44] reported an increase of four times in impact energy by

adding 0.7 μm diameter $CaCO_3$ particles in *i*PP, which are ideal candidates for rigid fillers. By combining PEP-PEE_E micelles with cheap yet effective $CaCO_3$ fillers, blends with both high strength and toughness might be obtained. We note that the addition of rigid fillers can possibly alter the crystallization behavior of *i*PP and the dispersion of block copolymer micelles. Furthermore, the concentrations of $CaCO_3$ particles need to be carefully tuned so that it will not have detrimental effects on the tensile properties as low strains at break are commonly seen in blends with high concentrations of rigid fillers.

6.3 *i*PP/PE compatibilizers with various architectures and mechanistic study on the compatibilization performance

In Chapter 5, we have demonstrated the interesting dependence of *i*PP/PE adhesion enhancement and compatibilization performance on the molecular weight and architecture of the *i*PP-PE block copolymer compatibilizers. We have proposed mechanisms concerning co-crystallization and entanglement to explain our observations, however, more studies need to be conducted to lend evidence to the mechanisms. Furthermore, the remarkable interfacial activity of these block copolymers is not well understood, i.e. they tend to go to the immiscible interface rather than form micelles.

The block copolymers will be melt mixed with *i*PP or PE homopolymers to explore the micellization process and probe how molecular weights and architecture affect it. Traditional characterization/imaging techniques, such as SEM and TEM, may not work well in the mechanistic study due to the limited contrast between the semicrystalline homopolymers and semicrystalline block copolymers, especially at very low block

copolymer concentrations. We are planning to isotope label the block copolymers with deuterium gas according to the methods reported by Habersberg *et al.*[176] and Zeng *et al.*[177]. Deuterium will have a very different scattering length density than that of hydrogen, offering sufficient contrast in small angle neutron scattering (SANS) experiments. SANS will provide invaluable insights into the segregation structures of the block copolymers and the possible sources of the interfacial activity. What's more, the deuterium-labeled polymers have a distinct wavelength for C-D stretching than their hydrogenous counterparts in infrared spectroscopy (IR). In a recent work, Rickard *et al.*[196] deuterium labeled ethylene-propylene (EP) copolymers and used AFM-IR to image the location of EP in the ternary blends of PP/PE/EP. This technique can also be applied in our system to visualize the location of *i*PP-PE block copolymers in compatibilized PP/PE blends and further elucidate how different molecular weights and architecture can make a difference.

There are other interesting architectures worth exploring besides linear multiblocks, for example, graft copolymers and star polymers as shown in Figure 6.1. The copolymers can be synthesized by our collaborators in the Cornell University using the chemical scheme in Figure 6.1. They can be even more effective than the multiblock copolymers since there are more anchoring and stitching sites at the immiscible interface.

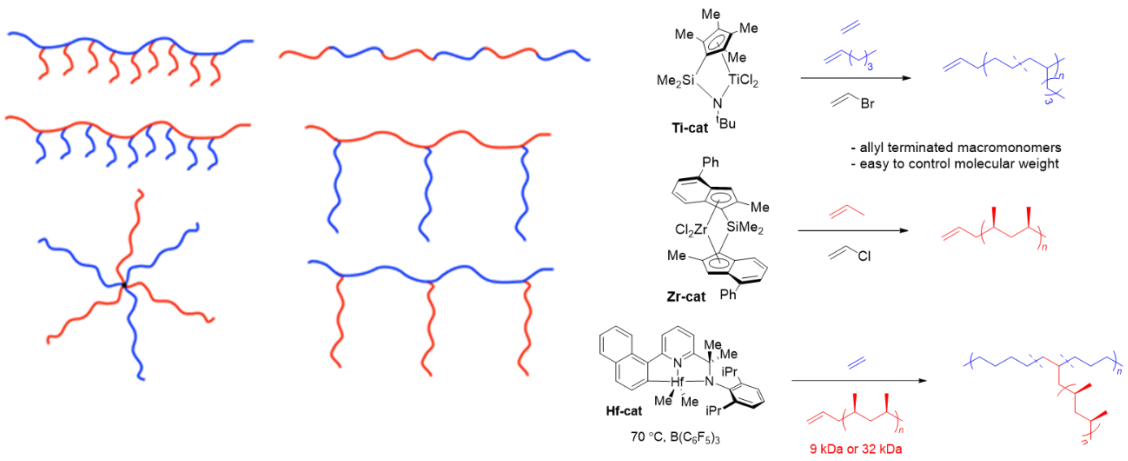

Figure 6.1 *i*PP-PE graft and star copolymers and synthetic schematic

Bibliography

(1) Flory, P. J. Thermodynamics of High Polymer Solutions. *J. Chem. Phys.* **1942,** *10*, 51-61.

(2) Flory, P. J. Thermodynamics of Heterogeneous Polymers and Their Solutions. *J. Chem. Phys.* **1944,** *12*, 425-438.

(3) Flory, P. J.; Orwoll, R. A.; Vrij, A. Statistical Thermodynamics of Chain Molecule Liquids. II. Liquid Mixtures of Normal Paraffin Hydrocarbons. *J. Am. Chem. Soc.* **1964,** *86*, 3515-3520.

(4) Flory, P. J. Statistical Thermodynamics of Liquid Mixtures. *J. Am. Chem. Soc.* **1965,** *87*, 1833-1838.

(5) Flory, P. J. Fifteenth Spiers Memorial Lecture. Thermodynamics of Polymer Solutions. *Discuss Faraday Soc.* **1970,** *49*, 7-29.

(6) Bates, F. S.; Schulz, M. F.; Rosedale, J. H.; Almdal, K. Correlation of Binary Polyolefin Phase Behavior with Statistical Segment Length Asymmetry. *Macromolecules* **1992,** *25*, 5547-5550.

(7) Bates, F. S.; Fredrickson, G. H. Conformational Asymmetry and Polymer-Polymer Thermodynamics. *Macromolecules* **1994,** *27*, 1065-1067.

(8) Balsara, N. P.; Fetters, L. J.; Hadjichristidis, N.; Lohse, D. J.; Han, C. C.; Graessley, W. W.; Krishnamoorti, R. Thermodynamic Interactions in Model Polyolefin Blends Obtained by Small-Angle Neutron Scattering. *Macromolecules* **1992,** *25*, 6137-6147.

(9) Graessley, W. W.; Krishnamoorti, R.; Balsara, N. P.; Butera, R. J.; Fetters, L. J.; Lohse, D. J.; Schulz, D. N.; Sissano, J. A. Thermodynamics of Mixing for Blends of Model Ethylene-Butene Copolymers. *Macromolecules* **1994,** *27*, 3896-3901.

(10) Krishnamoorti, R.; Graessley, W. W.; Dee, G. T.; Walsh, D. J.; Fetters, L. J.; Lohse, D. J. Pure Component Properties and Mixing Behavior in Polyolefin Blends. *Macromolecules* **1996,** *29*, 367-376.

(11) Reichart, G. C.; Graessley, W. W.; Register, R. A.; Lohse, D. J. Thermodynamics of Mixing for Statistical Copolymers of Ethylene and α-Olefins. *Macromolecules* **1998,** *31*, 7886-7894.

(12) Mulhearn, W. D.; Register, R. A. Melt Miscibility in Diblock Copolymers Containing Polyethylene and Substituted Hydrogenated Polynorbornenes. *Macromolecules* **2017,** *50*, 5830-5838.

(13) Qiu, J.; Mongcopa, K. I.; Han, R.; López-Barrón, C. R.; Robertson, M. L.; Krishnamoorti, R. Thermodynamic Interactions in a Model Polydiene/Polyolefin Blend Based on 1,2-Polybutadiene. *Macromolecules* **2018,** *51*, 3107-3115.

(14) Schweizer, K. S.; Singh, C. Microscopic Solubility-Parameter Theory of Polymer Blends: General Predictions. *Macromolecules* **1995,** *28*, 2063-2080.

(15) Schweizer, K. S. Analytic Prism Theory of Structurally Asymmetric Polymer Blends and Copolymers. *Macromolecules* **1993,** *26*, 6050-6067.

(16) Dudowicz, J.; Freed, M. S.; Freed, K. F. Effect of Monomer Structure and Compressibility on the Properties of Multicomponent Polymer Blends and Solutions. 2. Application to Binary Blends. *Macromolecules* **1991,** *24*, 5096-5111.

(17) Chen, Q. P.; Xie, S.; Foudazi, R.; Lodge, T. P.; Siepmann, J. I. Understanding the Molecular Weight Dependence of χ and the Effect of Dispersity on Polymer Blend Phase Diagrams. *Macromolecules* **2018,** *51*, 3774-3787.

(18) Chen, Q. P.; Chu, J. D.; DeJaco, R. F.; Lodge, T. P.; Siepmann, J. I. Molecular Simulation of Olefin Oligomer Blend Phase Behavior. *Macromolecules* **2016,** *49*, 3975-3985.

(19) Chen, Q. P.; Barreda, L.; Oquendo, L. E.; Hillmyer, M. A.; Lodge, T. P.; Siepmann, J. I. Computational Design of High-χ Block Oligomers for Accessing 1 nm Domains. *ACS Nano* **2018,** *12*, 4351-4361.

(20) Freed, K. F.; Dudowicz, J. Lattice Cluster Theory for Pedestrians: The Incompressible Limit and the Miscibility of Polyolefin Blends. *Macromolecules* **1998,** *31*, 6681-6690.

(21) Dudowicz, J.; Freed, K. F. Effect of Monomer Structure and Compressibility on the Properties of Multicomponent Polymer Blends and Solutions: 1. Lattice Cluster Theory of Compressible Systems. *Macromolecules* **1991,** *24*, 5076-5095.

(22) Graessley, W. W.; Krishnamoorti, R.; Reichart, G. C.; Balsara, N. P.; Fetters, L. J.; Lohse, D. J. Regular and Irregular Mixing in Blends of Saturated Hydrocarbon Polymers. *Macromolecules* **1995,** *28*, 1260-1270.

(23) White, R. P.; Lipson, J. E. G.; Higgins, J. S. New Correlations in Polymer Blend Miscibility. *Macromolecules* **2012,** *45*, 1076-1084.

(24) White, R. P.; Lipson, J. E. G.; Higgins, J. S. How Pure Components Control Polymer Blend Miscibility. *Macromolecules* **2012,** *45*, 8861-8871.

(25) Fredrickson, G. H.; Liu, A. J.; Bates, F. S. Entropic Corrections to the Flory-Huggins Theory of Polymer Blends: Architectural and Conformational Effects. *Macromolecules* **1994,** *27*, 2503-2511.

(26) Helfand, E.; Sapse, A. M. Theory of Unsymmetric Polymer–Polymer Interfaces. *J. Chem. Phys.* **1975,** *62*, 1327-1331.

(27) Weimann, P. A.; Jones, T. D.; Hillmyer, M. A.; Bates, F. S.; Londono, J. D.; Melnichenko, Y.; Wignall, G. D.; Almdal, K. Phase Behavior of Isotactic Polypropylene−Poly(Ethylene/Ethylethylene) Random Copolymer Blends. *Macromolecules* **1997,** *30*, 3650-3657.

(28) Bates, F. S.; Kumar, A.; Schulz, M. F. Isotactic Polypropylene-Compatible Block Copolymer. *J. Polym. Sci., Part B: Polym. Phys.* **1995,** *33*, 1423-1427.

(29) Cochran, E. W.; Bates, F. S. Thermodynamic Behavior of Poly(Cyclohexylethylene) in Polyolefin Diblock Copolymers. *Macromolecules* **2002,** *35*, 7368-7374.

(30) Bai, L.; Sharma, R.; Cheng, X.; Macosko, C. W. Kinetic Control of Graphene Localization in Co-Continuous Polymer Blends Via Melt Compounding. *Langmuir* **2018,** *34*, 1073-1083.

(31) Huang, S.; Bai, L.; Trifkovic, M.; Cheng, X.; Macosko, C. W. Controlling the Morphology of Immiscible Cocontinuous Polymer Blends Via Silica Nanoparticles Jammed at the Interface. *Macromolecules* **2016,** *49*, 3911-3918.

(32) Bai, L.; He, S.; Fruehwirth, J. W.; Stein, A.; Macosko, C. W.; Cheng, X. Localizing Graphene at the Interface of Cocontinuous Polymer Blends: Morphology, Rheology, and Conductivity of Cocontinuous Conductive Polymer Composites. *J. Rheol.* **2017,** *61*, 575-587.

(33) Zhang, Q.; Xu, J.; Song, Q.; Li, N.; Zhang, Z.; Li, K.; Du, Y.; Wu, L.; Tang, M.; Liu, L.; Cheng, G.; Liu, J. Synthesis of Amphiphilic Reduced Graphene Oxide with an Enhanced Charge Injection Capacity for Electrical Stimulation of Neural Cells. *J. Mater. Chem. B* **2014,** *2*, 4331-4337.

(34) Du, Y.; Xu, J.; Sakizadeh, J. D.; Weiblen, D. G.; McCormick, A. V.; Francis, L. F. Modulus- and Surface-Energy-Tunable Thiol–Ene for UV Micromolding of Coatings. *ACS Appl. Mat. Interfaces* **2017,** *9*, 24976-24986.

(35) Zhi, S.-H.; Deng, R.; Xu, J.; Wan, L.-S.; Xu, Z.-K. Composite Membranes from Polyacrylonitrile with Poly(N,N-Dimethylaminoethyl Methacrylate)-Grafted Silica Nanoparticles as Additives. *React. Funct. Polym.* **2015,** *86*, 184-190.

(36) Zhi, S.-H.; Xu, J.; Deng, R.; Wan, L.-S.; Xu, Z.-K. Poly(Vinylidene Fluoride) Ultrafiltration Membranes Containing Hybrid Silica Nanoparticles: Preparation, Characterization and Performance. *Polymer* **2014,** *55*, 1333-1340.

(37) van der Wal, A.; Mulder, J. J.; Oderkerk, J.; Gaymans, R. J. Polypropylene–Rubber Blends: 1. The Effect of the Matrix Properties on the Impact Behaviour. *Polymer* **1998,** *39*, 6781-6787.

(38) Jang, B. Z.; Uhlmann, D. R.; Sande, J. B. V. Rubber-Toughening in Polypropylene. *J. Appl. Polym. Sci.* **1985,** *30*, 2485-2504.

(39) Jiang, W.; Tjong, S. C.; Li, R. K. Y. Brittle–Tough Transition in PP/EPDM Blends: Effects of Interparticle Distance and Tensile Deformation Speed. *Polymer* **2000,** *41*, 3479-3482.

(40) Yokoyama, Y.; Ricco, T. Toughening of Polypropylene by Different Elastomeric Systems. *Polymer* **1998,** *39*, 3675-3681.

(41) Wei, G. X.; Sue, H. J.; Chu, J.; Huang, C.; Gong, K. Toughening and Strengthening of Polypropylene Using the Rigid–Rigid Polymer Toughening Concept Part I. Morphology and Mechanical Property Investigations. *Polymer* **2000,** *41*, 2947-2960.

(42) Rong, M. Z.; Zhang, M. Q.; Zheng, Y. X.; Zeng, H. M.; Walter, R.; Friedrich, K. Structure–Property Relationships of Irradiation Grafted Nano-Inorganic Particle Filled Polypropylene Composites. *Polymer* **2001,** *42*, 167-183.

(43) Chan, C.-M.; Wu, J.; Li, J.-X.; Cheung, Y.-K. Polypropylene/Calcium Carbonate Nanocomposites. *Polymer* **2002,** *43*, 2981-2992.

(44) Thio, Y. S.; Argon, A. S.; Cohen, R. E.; Weinberg, M. Toughening of Isotactic Polypropylene with Caco3 Particles. *Polymer* **2002,** *43*, 3661-3674.

(45) Lin, Y.; Chen, H.; Chan, C.-M.; Wu, J. High Impact Toughness Polypropylene/$CaCO_3$ Nanocomposites and the Toughening Mechanism. *Macromolecules* **2008,** *41*, 9204-9213.

(46) Lin, Y.; Chen, H.; Chan, C.-M.; Wu, J. The Toughening Mechanism of Polypropylene/Calcium Carbonate Nanocomposites. *Polymer* **2010,** *51*, 3277-3284.

(47) Premphet K.; Horanont P. Influence of Stearic Acid Treatment of Filler Particles on the Structure and Properties of Ternary-Phase Polypropylene Composites. *J. Appl. Polym. Sci.* **1999,** *74*, 3445-3454.

(48) Zhang, L.; Li, C.; Huang, R. Toughness Mechanism in Polypropylene Composites: Polypropylene Toughened with Elastomer and Calcium Carbonate. *J. Polym. Sci., Part B: Polym. Phys.* **2004,** *42*, 1656-1662.

(49) Uotila, R.; Hippi, U.; Paavola, S.; Seppälä, J. Compatibilization of PP/Elastomer/Microsilica Composites with Functionalized Polyolefins: Effect on Microstructure and Mechanical Properties. *Polymer* **2005,** *46*, 7923-7930.

(50) Ma, C. G.; Mai, Y. L.; Rong, M. Z.; Ruan, W. H.; Zhang, M. Q. Phase Structure and Mechanical Properties of Ternary Polypropylene/Elastomer/Nano-$CaCO_3$ Composites. *Compos. Sci. Tech.* **2007,** *67*, 2997-3005.

(51) Abreu, F. O. M. S.; Forte, M. M. C.; Liberman, S. A. SBS and SEBS Block Copolymers as Impact Modifiers for Polypropylene Compounds. *J. Appl. Polym. Sci.* **2005,** *95*, 254-263.

(52) Liu, G.; Zhang, X.; Liu, C.; Chen, H.; Walton, K.; Wang, D. Morphology and Mechanical Properties of Binary Blends of Polypropylene with Statistical and Block Ethylene-Octene Copolymers. *J. Appl. Polym. Sci.* **2011,** *119*, 3591-3597.

(53) Liu, G.; Zhang, X.; Li, X.; Chen, H.; Walton, K.; Wang, D. Correlation of Miscibility and Mechanical Properties of Polypropylene/Olefin Block Copolymers: Effect of Chain Composition. *J. Appl. Polym. Sci.* **2012,** *125*, 666-675.

(54) Bucknall, C. B.; Karpodinis, A.; Zhang, X. C. A Model for Particle Cavitation in Rubber-Toughened Plastics. *J. Mater. Sci.* **1994,** *29*, 3377-3383.

(55) Lazzeri, A.; Bucknall, C. B. Applications of a Dilatational Yielding Model to Rubber-Toughened Polymers. *Polymer* **1995,** *36*, 2895-2902.

(56) Zhang, L.; Li, C.; Huang, R. Toughness Mechanism of Polypropylene/Elastomer/Filler Composites. *J. Polym. Sci., Part B: Polym. Phys.* **2005,** *43*, 1113-1123.

(57) Bucknall, C. B.; Paul, D. R. Notched Impact Behavior of Polymer Blends: Part 1: New Model for Particle Size Dependence. *Polymer* **2009,** *50*, 5539-5548.

(58) Bucknall, C. B.; Paul, D. R. Notched Impact Behaviour of Polymer Blends: Part 2: Dependence of Critical Particle Size on Rubber Particle Volume Fraction. *Polymer* **2013,** *54*, 320-329.

(59) Chen, F.; Shangguan, Y.; Jiang, Y.; Qiu, B.; Luo, G.; Zheng, Q. Toughening with Little Rigidity Loss and Mechanism for Modified Polypropylene by Polymer Particles with Core–Shell Structure. *Polymer* **2015,** *65*, 81-92.

(60) Argon, A. S., *The Physics of Deformation and Fracture of Polymers*. Cambridge University Press: Cambridge, 2013.

(61) Bucknall, C. B.; Heather, P. S.; Lazzeri, A. Rubber Toughening of Plastics. *J. Mater. Sci.* **1989,** *24*, 2255-2261.

(62) Lazzeri, A.; Bucknall, C. B. Dilatational Bands in Rubber-Toughened Polymers. *J. Mater. Sci.* **1993,** *28*, 6799-6808.

(63) Liang, J. Z.; Li, R. K. Y.; Tjong, S. C. Impact Fracture Behavior of PP/EPDM/Glass Bead Ternary Composites. *Polym. Eng. Sci.* **2000,** *40*, 2105-2111.

(64) Dasari, A.; Zhang, Q.-X.; Yu, Z.-Z.; Mai, Y.-W. Toughening Polypropylene and Its Nanocomposites with Submicrometer Voids. *Macromolecules* **2010,** *43*, 5734-5739.

(65) Bartczak, Z.; Galeski, A., Mechanical Properties of Polymer Blends. In *Polymer Blends Handbook*, Utracki, L. A.; Wilkie, C. A., Eds. Springer Netherlands: Dordrecht, 2014; pp 1203-1297.

(66) Hillmyer, M. A.; Lipic, P. M.; Hajduk, D. A.; Almdal, K.; Bates, F. S. Self-Assembly and Polymerization of Epoxy Resin-Amphiphilic Block Copolymer Nanocomposites. *J. Am. Chem. Soc.* **1997,** *119*, 2749-2750.

(67) Wu, J.; Thio, Y. S.; Bates, F. S. Structure and Properties of PBO–PEO Diblock Copolymer Modified Epoxy. *J. Polym. Sci., Part B: Polym. Phys.* **2005,** *43*, 1950-1965.

(68) Liu, J.; Sue, H.-J.; Thompson, Z. J.; Bates, F. S.; Dettloff, M.; Jacob, G.; Verghese, N.; Pham, H. Nanocavitation in Self-Assembled Amphiphilic Block Copolymer-Modified Epoxy. *Macromolecules* **2008,** *41*, 7616-7624.

(69) Thio, Y. S.; Wu, J.; Bates, F. S. The Role of Inclusion Size in Toughening of Epoxy Resins by Spherical Micelles. *J. Polym. Sci., Part B: Polym. Phys.* **2009,** *47*, 1125-1129.

(70) Declet-Perez, C.; Francis, L. F.; Bates, F. S. Cavitation in Block Copolymer Modified Epoxy Revealed by in Situ Small-Angle X-Ray Scattering. *ACS Macro Lett.* **2013,** *2*, 939-943.

(71) Li, T.; Heinzer, M. J.; Redline, E. M.; Zuo, F.; Bates, F. S.; Francis, L. F. Microstructure and Performance of Block Copolymer Modified Epoxy Coatings. *Prog. Org. Coat.* **2014,** *77*, 1145-1154.

(72) Li, T.; He, S.; Stein, A.; Francis, L. F.; Bates, F. S. Synergistic Toughening of Epoxy Modified by Graphene and Block Copolymer Micelles. *Macromolecules* **2016,** *49*, 9507-9520.

(73) Li, T.; Heinzer, M. J.; Francis, L. F.; Bates, F. S. Engineering Superior Toughness in Commercially Viable Block Copolymer Modified Epoxy Resin. *J. Polym. Sci., Part B: Polym. Phys.* **2016,** *54*, 189-204.

(74) Li, T.; Zhang, J.; Schneiderman, D. K.; Francis, L. F.; Bates, F. S. Toughening Glassy Poly(Lactide) with Block Copolymer Micelles. *ACS Macro Lett.* **2016,** *5*, 359-364.

(75) Ruzette, A.-V.; Leibler, L. Block Copolymers in Tomorrow's Plastics. *Nat. Mater.* **2005,** *4*, 19-31.

(76) Xanthos, M.; Dagli, S. S. Compatibilization of Polymer Blends by Reactive Processing. *Polym. Eng. Sci.* **1991,** *31*, 929-935.

(77) Tselios, C.; Bikiaris, D.; Maslis, V.; Panayiotou, C. In Situ Compatibilization of Polypropylene–Polyethylene Blends: A Thermomechanical and Spectroscopic Study. *Polymer* **1998,** *39*, 6807-6817.

(78) Colbeaux, A.; Fenouillot, F.; Gerard, J.-F.; Taha, M.; Wautier, H. Compatibilization of a Polyolefin Blend through Covalent and Ionic Coupling of Grafted Polypropylene and Polyethylene. Ii. Morphology. *J. Appl. Polym. Sci.* **2004,** *93*, 2237-2244.

(79) Khalili, R.; Jafari, S. H.; Saeb, M. R.; Khonakdar, H. A.; Wagenknecht, U.; Heinrich, G. Toward in Situ Compatibilization of Polyolefin Ternary Blends through Morphological Manipulations. *Macromol. Mater. Eng.* **2014,** *299*, 1197-1212.

(80) Chiu, W.-Y.; Fang, S.-J. Mechanical Properties and Morphology of Crosslinked PP/PE Blends and PP/PE/Propylene–Ethylene Copolymer Blends. *J. Appl. Polym. Sci.* **1985,** *30*, 1473-1489.

(81) Gu, J.; Xu, H.; Wu , C. The Effect of PP and Peroxide on the Properties and Morphology of HDPE and HDPE/PP Blends. *Adv. Polym. Tech.* **2013,** *32*.

(82) Yu, D. W.; Xanthos, M.; Gogos, C. G. Peroxide Modified Polyolefin Blends—Part II: Effects on LDPE/PP Blends with Polymer Components of Dissimilar Initial Viscosities. *Adv. Polym. Tech.* **1992,** *11*, 295-304.

(83) Borsig, E.; Fiedlerová, A.; Rychlá, L.; Lazár, M.; Rätzsch, M.; Haudel, G. Crosslinking of Polypropylene–Polyethylene Blends by Peroxide and the Effect of Pentaerythritol Tetrallyl Ether. *J. Appl. Polym. Sci.* **1989,** *37*, 467-478.

(84) D'Orazio, L.; Greco, R.; Martuscelli, E.; Ragosta, G. Effect of the Addition of EPM Copolymers on the Properties of High Density Polyethylene/Isotactic Polypropylene Blends: II. Morphology and Mechanical Properties of Extruded Samples. *Polym. Eng. Sci.* **1983,** *23*, 489-497.

(85) D'Orazio, L.; Greco, R.; Mancarella, C.; Martuscelli, E.; Ragosta, G.; Silvesrte, C. Effect of the Addition of Ethylene-Propylene Random Copolymers on the Properties of High-Density Polyethylene/Isotactic Polypropylene Blends: Part 1—Morphology and Impact Behavior of Molded Samples. *Polym. Eng. Sci.* **1982,** *22*, 536-544.

(86) Hemmati, M.; Nazokdast, H.; Shariat Panahi, H. Study on Morphology of Ternary Polymer Blends. I. Effects of Melt Viscosity and Interfacial Interaction. *J. Appl. Polym. Sci.* **2001,** *82*, 1129-1137.

(87) Plawky, U.; Schlabs, M.; Wenig, W. The Role of Styrene–Ethylene/Butylene–Styrene Triblock Copolymer as Impact Modifier in Polypropylene–Polyethylene Blends. *J. Appl. Polym. Sci.* **1996,** *59*, 1891-1896.

(88) Kallel, T.; Massardier-Nageotte, V.; Jaziri, M.; Gérard, J.-F.; Elleuch, B. Compatibilization of PE/PS and PE/PP Blends. I. Effect of Processing Conditions and Formulation. *J. Appl. Polym. Sci.* **2003,** *90*, 2475-2484.

(89) Ubonnut, L.; Thongyai, S.; Praserthdam, P. Interfacial Adhesion Enhancement of Polyethylene–Polypropylene Mixtures by Adding Synthesized Diisocyanate Compatibilizers. *J. Appl. Polym. Sci.* **2007,** *104*, 3766-3773.

(90) Louizi, M.; Massardier, V.; Cassagnau, P. Contribution of High-Shear Processing to the Compatibilization of (PP/EPR)/PE Ternary Blends. *Macromol. Mater. Eng.* **2014,** *299*, 674-688.

(91) Nedkov, T.; Lednický, F. Morphologies of Polyethylene–Ethylene/Propylene/Diene Monomer Particles in Polypropylene-Rich Polyolefin Blends: Flake Structure. *J. Appl. Polym. Sci.* **2003,** *90*, 3087-3092.

(92) Zhu, W.; Zhang, X.; Huang, B.; Feng, Z. Modification of PP/HDPE Blends by PP-PE Sequential Polymerization Product. *J. Appl. Polym. Sci.* **1995,** *58*, 515-521.

(93) Lin, Y.; Marchand, G. R.; Hiltner, A.; Baer, E. Adhesion of Olefin Block Copolymers to Polypropylene and High Density Polyethylene and Their Effectiveness as Compatibilizers in Blends. *Polymer* **2011,** *52*, 1635-1644.

(94) Lin, Y.; Yakovleva, V.; Chen, H.; Hiltner, A.; Baer, E. Comparison of Olefin Copolymers as Compatibilizers for Polypropylene and High-Density Polyethylene. *J. Appl. Polym. Sci.* **2009,** *113*, 1945-1952.

(95) Vranjes, N.; Rek, V. Effect of EPDM on Morphology, Mechanical Properties, Crystallization Behavior and Viscoelastic Properties of iPP+HDPE Blends. *Macromol. Symp.* **2007,** *258*, 90-100.

(96) Chaffin, K. A.; Bates, F. S.; Brant, P.; Brown, G. M. Semicrystalline Blends of Polyethylene and Isotactic Polypropylene: Improving Mechanical Performance by Enhancing the Interfacial Structure. *J. Polym. Sci., Part B: Polym. Phys.* **2000,** *38*, 108-121.

(97) Sardelis, K.; Michels, H. J.; Allen, G.; F.R.S. Graded Block and Randomized Copolymers of Butadiene-Styrene. *Polymer* **1984,** *25*, 1011-1019.

(98) Pangborn, A. B.; Giardello, M. A.; Grubbs, R. H.; Rosen, R. K.; Timmers, F. J. Safe and Convenient Procedure for Solvent Purification. *Organometallics* **1996,** *15*, 1518-1520.

(99) Bates, F. S.; Fredrickson, G. H.; Hucul, D.; Hahn, S. F. PCHE-Based Pentablock Copolymers: Evolution of a New Plastic. *AlChE J.* **2001,** *47*, 762-765.

(100) Brown, G. M.; Butler, J. H. New Method for the Characterization of Domain Morphology of Polymer Blends Using Ruthenium Tetroxide Staining and Low Voltage Scanning Electron Microscopy (LVSEM). *Polymer* **1997,** *38*, 3937-3945.

(101) Wang, Z. Toughening and Reinforcing of Polypropylene. *J. Appl. Polym. Sci.* **1996,** *60*, 2239-2243.

(102) Ou, Y. C.; Guo, T. T.; Fang, X. P.; Yu, Z. Z. Toughening and Reinforcing Polypropylene with Core–Shell Structured Fillers. *J. Appl. Polym. Sci.* **1999,** *74*, 2397-2403.

(103) Zuiderduin, W. C. J.; Westzaan, C.; Huétink, J.; Gaymans, R. J. Toughening of Polypropylene with Calcium Carbonate Particles. *Polymer* **2003,** *44*, 261-275.

(104) Zhu, L. D.; Yang, H. Y.; Cai, G. D.; Zhou, C.; Wu, G. F.; Zhang, M. Y.; Gao, G. H.; Zhang, H. X. Submicrometer-Sized Rubber Particles as "Craze-Bridge" for Toughening Polystyrene/High-Impact Polystyrene. *J. Appl. Polym. Sci.* **2013,** *129*, 224-229.

(105) Kowalczyk, M.; Piorkowska, E.; Dutkiewicz, S.; Sowinski, P. Toughening of Polylactide by Blending with a Novel Random Aliphatic–Aromatic Copolyester. *Eur. Polym. J.* **2014,** *59*, 59-68.

(106) Bartczak, Z.; Argon, A. S.; Cohen, R. E.; Weinberg, M. Toughness Mechanism in Semi-Crystalline Polymer Blends: I. High-Density Polyethylene Toughened with Rubbers. *Polymer* **1999,** *40*, 2331-2346.

(107) Liang, J. Z.; Li, R. K. Y. Rubber Toughening in Polypropylene: A Review. *J. Appl. Polym. Sci.* **2000,** *77*, 409-417.

(108) Wu, S. Phase Structure and Adhesion in Polymer Blends: A Criterion for Rubber Toughening. *Polymer* **1985,** *26*, 1855-1863.

(109) Margolina, A.; Wu, S. Percolation Model for Brittle-Tough Transition in Nylon/Rubber Blends. *Polymer* **1988,** *29*, 2170-2173.

(110) Bartczak, Z.; Argon, A. S.; Cohen, R. E.; Weinberg, M. Toughness Mechanism in Semi-Crystalline Polymer Blends: II. High-Density Polyethylene Toughened with Calcium Carbonate Filler Particles. *Polymer* **1999,** *40*, 2347-2365.

(111) Jiang, W.; Liu, C. H.; Wang, Z. G.; An, L. J.; Liang, H. J.; Jiang, B. Z.; Wang, X. H.; Zhang, H. X. Brittle-Tough Transition in PP/EPDM Blends: Effects of Interparticle Distance and Temperature. *Polymer* **1998,** *39*, 3285-3288.

(112) Orwoll, R. A.; Flory, P. J. Thermodynamic Properties of Binary Mixtures of n-Alkanes. *J. Am. Chem. Soc.* **1967,** *89*, 6822-6829.

(113) Graessley, W. W.; Krishnamoorti, R.; Balsara, N. P.; Fetters, L. J.; Lohse, D. J.; Schulz, D. N.; Sissano, J. A. Deuteration Effects and Solubility Parameter Ordering in Blends of Saturated Hydrocarbon Polymers. *Macromolecules* **1994,** *27*, 2574-2579.

(114) Graessley, W. W.; Krishnamoorti, R.; Balsara, N. P.; Fetters, L. J.; Lohse, D. J.; Schulz, D. N.; Sissano, J. A. Effect of Deuterium Substitution on Thermodynamic Interactions in Polymer Blends. *Macromolecules* **1993,** *26*, 1137-1143.

(115) Knychała, P.; Timachova, K.; Banaszak, M.; Balsara, N. P. 50th Anniversary Perspective: Phase Behavior of Polymer Solutions and Blends. *Macromolecules* **2017,** *50*, 3051-3065.

(116) Jackson, C.; Chen, Y.-J.; Mays, J. W. Size Exclusion Chromatography with Multiple Detectors: Solution Properties of Linear Chains of Varying Flexibility in Tetrahydrofuran. *J. Appl. Polym. Sci.* **1996,** *61*, 865-874.

(117) Kim, J.; Mok, M. M.; Sandoval, R. W.; Woo, D. J.; Torkelson, J. M. Uniquely Broad Glass Transition Temperatures of Gradient Copolymers Relative to Random and Block Copolymers Containing Repulsive Comonomers. *Macromolecules* **2006,** *39*, 6152-6160.

(118) Mok, M. M.; Kim, J.; Wong, C. L. H.; Marrou, S. R.; Woo, D. J.; Dettmer, C. M.; Nguyen, S. T.; Ellison, C. J.; Shull, K. R.; Torkelson, J. M. Glass Transition Breadths and

Composition Profiles of Weakly, Moderately, and Strongly Segregating Gradient Copolymers: Experimental Results and Calculations from Self-Consistent Mean-Field Theory. *Macromolecules* **2009,** *42*, 7863-7876.

(119) Wu, S. Formation of Dispersed Phase in Incompatible Polymer Blends: Interfacial and Rheological Effects. *Polym. Eng. Sci.* **1987,** *27*, 335-343.

(120) Naiki, M.; Matsumura, T.; Matsuda, M. Tensile Elongation of High-Fluid Polypropylene/Ethylene–Propylene Rubber Blends: Dependence on Molecular Weight of the Components and Propylene Content of the Rubber. *J. Appl. Polym. Sci.* **2002,** *83*, 46-56.

(121) Palierne, J. F. Linear Rheology of Viscoelastic Emulsions with Interfacial Tension. *Rheol. Acta* **1990,** *29*, 204-214.

(122) Graebling, D.; Muller, R.; Palierne, J. F. Linear Viscoelastic Behavior of Some Incompatible Polymer Blends in the Melt. Interpretation of Data with a Model of Emulsion of Viscoelastic Liquids. *Macromolecules* **1993,** *26*, 320-329.

(123) Bousmina, M. Rheology of Polymer Blends: Linear Model for Viscoelastic Emulsions. *Rheol. Acta* **1999,** *38*, 73-83.

(124) Krishnamoorti, R.; Graessley, W. W.; Zirkel, A.; Richter, D.; Hadjichristidis, N.; Fetters, L. J.; Lohse, D. J. Melt-State Polymer Chain Dimensions as a Function of Temperature. *J. Polym. Sci., Part B: Polym. Phys.* **2002,** *40*, 1768-1776.

(125) Van Krevelen, D. W., Chapter 7 - Cohesive Properties and Solubility. In *Properties of Polymers*, 3rd ed.; Elsevier: Amsterdam, 1997; pp 189-225.

(126) Boyer, R. F.; Spencer, R. S. Thermal Expansion and Second-Order Transition Effects in High Polymers: Part I. Experimental Results. *J. Appl. Phys.* **1944,** *15*, 398-405.

(127) Fetters, L. J.; Lohse, D. J.; Richter, D.; Witten, T. A.; Zirkel, A. Connection between Polymer Molecular Weight, Density, Chain Dimensions, and Melt Viscoelastic Properties. *Macromolecules* **1994,** *27*, 4639-4647.

(128) Helfand, E.; Tagami, Y. Theory of the Interface between Immiscible Polymers. *J. Polym. Sci., Part B: Polym. Phys.* **1971,** *9*, 741-746.

(129) Helfand, E.; Tagami, Y. Theory of the Interface between Immiscible Polymers. II. *J. Chem. Phys.* **1972,** *56*, 3592-3601.

(130) Kotek, J.; Raab, M.; Baldrian, J.; Grellmann, W. The Effect of Specific β-Nucleation on Morphology and Mechanical Behavior of Isotactic Polypropylene. *J. Appl. Polym. Sci.* **2002,** *85*, 1174-1184.

(131) Luo, F.; Geng, C.; Wang, K.; Deng, H.; Chen, F.; Fu, Q.; Na, B. New Understanding in Tuning Toughness of β-Polypropylene: The Role of β-Nucleated Crystalline Morphology. *Macromolecules* **2009,** *42*, 9325-9331.

(132) Zhang, L.; Li, C.; Huang, R. Toughness Mechanism in Polypropylene Composites: Polypropylene Toughened with Elastomer and Calcium Carbonate. *J. Polym. Sci., Part B: Polym. Phys.* **2004,** *42*, 1656-1662.

(133) Xu, J.; Mittal, V.; Bates, F. S. Toughened Isotactic Polypropylene: Phase Behavior and Mechanical Properties of Blends with Strategically Designed Random Copolymer Modifiers. *Macromolecules* **2016,** *49*, 6497-6506.

(134) Eagan, J. M.; Xu, J.; Di Girolamo, R.; Thurber, C. M.; Macosko, C. W.; LaPointe, A. M.; Bates, F. S.; Coates, G. W. Combining Polyethylene and Polypropylene: Enhanced Performance with PE/*i*PP Multiblock Polymers. *Science* **2017,** *355*, 814-816.

(135) D'Orazio, L.; Mancarella, C.; Martuscelli, E.; Sticotti, G. Polypropylene/Ethylene-co-Propylene Blends: Influence of Molecular Structure of EPR and Composition on Phase Structure of Isothermally Crystallized Samples. *J. Mater. Sci.* **1991,** *26*, 4033-4047.

(136) D'Orazio, L.; Mancarella, C.; Martuscelli, E.; Sticotti, G.; Cecchin, G. Isotactic Polypropylene/Ethylene-co-Propylene Blends: Influence of the Copolymer Microstructure on Rheology, Morphology, and Properties of Injection-Molded Samples. *J. Appl. Polym. Sci.* **1999,** *72*, 701-719.

(137) Yamaguchi, M.; Miyata, H.; Nitta, K.-H. Compatibility of Binary Blends of Polypropylene with Ethylene-α-Olefin Copolymer. *J. Appl. Polym. Sci.* **1996,** *62*, 87-97.

(138) Bai, S.-L.; Wang, G.-T.; Hiver, J.-M.; G'Sell, C. Microstructures and Mechanical Properties of Polypropylene/Polyamide 6/Polyethelene-Octene Elastomer Blends. *Polymer* **2004,** *45*, 3063-3071.

(139) Jose, S.; Aprem, A. S.; Francis, B.; Chandy, M. C.; Werner, P.; Alstaedt, V.; Thomas, S. Phase Morphology, Crystallisation Behaviour and Mechanical Properties of Isotactic Polypropylene/High Density Polyethylene Blends. *Euro. Polym. J.* **2004,** *40*, 2105-2115.

(140) Jafari, S. H.; Gupta, A. K. Impact Strength and Dynamic Mechanical Properties Correlation in Elastomer-Modified Polypropylene. *J. Appl. Polym. Sci.* **2000,** *78*, 962-971.

(141) Liu, Y.; Kontopoulou, M. The Structure and Physical Properties of Polypropylene and Thermoplastic Olefin Nanocomposites Containing Nanosilica. *Polymer* **2006,** *47*, 7731-7739.

(142) van der Wal, A.; Nijhof, R.; Gaymans, R. J. Polypropylene–Rubber Blends: 2. The Effect of the Rubber Content on the Deformation and Impact Behaviour. *Polymer* **1999,** *40*, 6031-6044.

(143) Krishnamoorti, R.; Graessley, W. W.; Balsara, N. P.; Lohse, D. J. Structural Origin of Thermodynamic Interactions in Blends of Saturated Hydrocarbon Polymers. *Macromolecules* **1994,** *27*, 3073-3081.

(144) Seki, M.; Nakano, H.; Yamauchi, S.; Suzuki, J.; Matsushita, Y. Miscibility of Isotactic Polypropylene/Ethylene−Propylene Random Copolymer Binary Blends. *Macromolecules* **1999,** *32*, 3227-3234.

(145) Koizumi, S.; Hasegawa, H.; Hashimoto, T. Spatial Distribution of Homopolymers in Block Copolymer Microdomains as Observed by a Combined SANS and SAXS Method. *Macromolecules* **1994,** *27*, 7893-7906.

(146) Karian, H., *Handbook of Polypropylene and Polypropylene Composites, Revised and Expanded*. CRC press: 2003.

(147) Brandrup, J.; Immergut, E. H.; Grulke, E. A.; Abe, A.; Bloch, D. R., *Polymer Handbook*. 3rd ed.; John Wiley & Sons: New York, 1989.

(148) Bates, F. S.; Rosedale, J. H.; Bair, H. E.; Russell, T. P. Synthesis and Characterization of a Model Saturated Hydrocarbon Diblock Copolymer. *Macromolecules* **1989,** *22*, 2557-2564.

(149) Mears, D. R.; Pae, K. D.; Sauer, J. A. Effects of Hydrostatic Pressure on the Mechanical Behavior of Polyethylene and Polypropylene. *J. Appl. Phys.* **1969,** *40*, 4229-4237.

(150) Fasce, L. A.; Pettarin, V.; Frontini, P. M., The Yielding of Propylene Polymers. In *SPE Annual Technical Conference - ANTEC, Conference Proceedings*, 2007; pp 264-268.

(151) Declet-Perez, C. Toughness in Block Copolymer Modified Epoxies. University of Minnesota, 2014.

(152) Deblieck, R. A. C.; van Beek, D. J. M.; Remerie, K.; Ward, I. M. Failure Mechanisms in Polyolefines: The Role of Crazing, Shear Yielding and the Entanglement Network. *Polymer* **2011,** *52*, 2979-2990.

(153) Global Polyethylene Market Research Report 2017-2021- Research and Markerts. *PR Newswire* 2017.

(154) Global Polypropylene (PP) Market Report 2017: $100+ Billion Market Size, Demand Forecasts, Industry Trends and Updates 2016-2022 - Research and Markets. *PR Newswire* 2017.

(155) Chemical Solutions for a Chemical Problem. *C&EN Global Enterprise* **2018,** *96*, 26-29.

(156) Wang, Y.; Hillmyer, M. A. Polyethylene-Poly(L-Lactide) Diblock Copolymers: Synthesis and Compatibilization of Poly(L-Lactide)/Polyethylene Blends. *J. Polym. Sci., Part A: Polym. Chem.* **2001,** *39*, 2755-2766.

(157) Macosko, C. W.; Guégan, P.; Khandpur, A. K.; Nakayama, A.; Marechal, P.; Inoue, T. Compatibilizers for Melt Blending: Premade Block Copolymers. *Macromolecules* **1996,** *29*, 5590-5598.

(158) Eastwood, E. A.; Dadmun, M. D. Multiblock Copolymers in the Compatibilization of Polystyrene and Poly(Methyl Methacrylate) Blends: Role of Polymer Architecture. *Macromolecules* **2002,** *35*, 5069-5077.

(159) Fayt, R.; Jérôme, R.; Teyssié, P. Molecular Design of Multicomponent Polymer Systems. III. Comparative Behavior of Pure and Tapered Block Copolymers in Emulsification of Blends of Low-Density Polyethylene and Polystyrene. *J. Polym. Sci., Part B: Polym. Phys.* **1982,** *20*, 2209-2217.

(160) Lee, M. S.; Lodge, T. P.; Macosko, C. W. Can Random Copolymers Serve as Effective Polymeric Compatibilizers? *J. Polym. Sci., Part B: Polym. Phys.* **1997,** *35*, 2835-2842.

(161) Helfand, E.; Sapse, A. M. Theory of Unsymmetric Polymer–Polymer Interfaces. *J. Chem. Phys.* **1975,** *62*, 1327-1331.

(162) Stehling, F. C.; Huff, T.; Speed, C. S.; Wissler, G. Structure and Properties of Rubber-Modified Polypropylene Impact Blends. *J. Appl. Polym. Sci.* **1981,** *26*, 2693-2711.

(163) Noolandi, J.; Hong, K. M. Interfacial Properties of Immiscible Homopolymer Blends in the Presence of Block Copolymers. *Macromolecules* **1982,** *15*, 482-492.

(164) Werner, A.; Schmid, F.; Binder, K.; Müller, M. Diblock Copolymers at a Homopolymer−Homopolymer Interface: A Monte Carlo Simulation. *Macromolecules* **1996,** *29*, 8241-8248.

(165) Creton, C.; Kramer, E. J.; Hadziioannou, G. Critical Molecular Weight for Block Copolymer Reinforcement of Interfaces in a Two-Phase Polymer Blend. *Macromolecules* **1991,** *24*, 1846-1853.

(166) Creton, C.; Kramer, E. J.; Hui, C. Y.; Brown, H. R. Failure Mechanisms of Polymer Interfaces Reinforced with Block Copolymers. *Macromolecules* **1992,** *25*, 3075-3088.

(167) Zhang, Z.; Chiu, D. S.; Siu, G. G. Sudy on the Polypropylene/High Density Polyethylene/Styrene-Butadiene-Styrene Block Copolymer Ternary Blends II. The Effect of Processing on the Properties and Morphology of Polypropylene/High Density Polyethylene/ Styrenebutadiene-Styrene Ternary Blends. *J. Reinf. Plast. Compos.* **1996,** *15*, 452-466.

(168) Chiu, D. S.; Zhang, Z.; Siu, G. G. Study on the Polypropylene/High Density Polyethylene/Styrene-Butadiene-Styrene Block Copolymer Ternary Blends: I-Composition, Morphology and Properties of Polypropylene/High Density Polyethylene/Styrene-Butadiene-Styrene Block Copolymer Blends. *J. Reinf. Plast. Compos.* **1996,** *15*, 74-85.

(169) Souza, A. M. C.; Demarquette, N. R. Influence of Coalescence and Interfacial Tension on the Morphology of PP/HDPE Compatibilized Blends. *Polymer* **2002,** *43*, 3959-3967.

(170) Arriola, D. J.; Carnahan, E. M.; Hustad, P. D.; Kuhlman, R. L.; Wenzel, T. T. Catalytic Production of Olefin Block Copolymers Via Chain Shuttling Polymerization. *Science* **2006,** *312*, 714-719.

(171) Busico, V.; Cipullo, R.; Friederichs, N.; Ronca, S.; Togrou, M. The First Molecularly Characterized Isotactic Polypropylene-Block-Polyethylene Obtained Via "Quasi-Living" Insertion Polymerization. *Macromolecules* **2003,** *36*, 3806-3808.

(172) Huh, K. M.; Bae, Y. H. Synthesis and Characterization of Poly(Ethylene Glycol)/Poly(L-Lactic Acid) Alternating Multiblock Copolymers. *Polymer* **1999,** *40*, 6147-6155.

(173) Chen, X.; McCarthy, S. P.; Gross, R. A. Synthesis and Characterization of [L]-Lactide−Ethylene Oxide Multiblock Copolymers. *Macromolecules* **1997,** *30*, 4295-4301.

(174) Lu, Y.; Lyu, D.; Xiong, B.; Chen, R.; Men, Y. Inter-Fibrillar Tie Chains Determined Critical Stress of Large Strain Cavitation in Tensile Stretched Isotactic Polypropylene. *Polymer* **2018,** *138*, 387-395.

(175) Butler, M. F.; Donald, A. M.; Bras, W.; Mant, G. R.; Derbyshire, G. E.; Ryan, A. J. A Real-Time Simultaneous Small- and Wide-Angle X-Ray Scattering Study of in-Situ Deformation of Isotropic Polyethylene. *Macromolecules* **1995,** *28*, 6383-6393.

(176) Habersberger, B. M.; Lodge, T. P.; Bates, F. S. Solvent Selective Hydrogen–Deuterium Exchange on Saturated Polyolefins. *Macromolecules* **2012,** *45*, 7778-7782.

(177) Zeng, Y.; López-Barrón, C. R.; Kang, S.; Eberle, A. P. R.; Lodge, T. P.; Bates, F. S. Effect of Branching and Molecular Weight on Heterogeneous Catalytic Deuterium Exchange in Polyolefins. *Macromolecules* **2017,** *50*, 6849-6860.

(178) Xu, J.; Howard, M. J.; Mittal, V.; Bates, F. S. Block Copolymer Micelle Toughened Isotactic Polypropylene. *Macromolecules* **2017,** *50*, 6421-6432.

(179) Jiang, X.; Drzal, L. T. Multifunctional High Density Polyethylene Nanocomposites Produced by Incorporation of Exfoliated Graphite Nanoplatelets 1: Morphology and Mechanical Properties. *Polym. Compos.* **2010,** *31*, 1091-1098.

(180) Tai, C. M.; Li, R. K. Y.; Ng, C. N. Impact Behaviour of Polypropylene/Polyethylene Blends. *Polym. Test.* **2000,** *19*, 143-154.

(181) Tjong, S. C.; Li, W. D.; Li, R. K. Y. Impact Toughening Behaviour of Quaternary PP/HDPE/EPDM/EP Blends. *Euro. Poly. J.* **1998,** *34*, 755-760.

(182) Choudhary, V.; Varma, H. S.; Varma, I. K. Effect of EPDM Rubber on Melt Rheology, Morphology and Mechanical Properties of Polypropylene/HDPE (9010) Blend. 2. *Polymer* **1991,** *32*, 2541-2545.

(183) Blom, H. P.; Teh, J. W.; Rudin, A. iPP/HDPE Blends. II. Modification with EPDM and EVA. *J. Appl. Polym. Sci.* **1996,** *60*, 1405-1417.

(184) Ha, M. H.; Kim, B. K.; Kim, E. Y. Effects of Dispersed Phase Composition on Thermoplastic Polyolefins. *J. Appl. Polym. Sci.* **2004,** *93*, 179-188.

(185) Norrman, K.; Ghanbari-Siahkali, A.; Larsen, N. 6 Studies of Spin-Coated Polymer Films. *Annu. Rep. Prog. Chem., Sect. C* **2005,** *101*, 174-201.

(186) Chaffin, K. A.; Knutsen, J. S.; Brant, P.; Bates, F. S. High-Strength Welds in Metallocene Polypropylene/Polyethylene Laminates. *Science* **2000,** *288*, 2187-2190.

(187) Cary, H. B.; Helzer, S. C., *Modern Welding Technology*. 6th ed.; Pearson: 2011.

(188) Eckstein, A.; Suhm, J.; Friedrich, C.; Maier, R. D.; Sassmannshausen, J.; Bochmann, M.; Mülhaupt, R. Determination of Plateau Moduli and Entanglement Molecular Weights of Isotactic, Syndiotactic, and Atactic Polypropylenes Synthesized with Metallocene Catalysts. *Macromolecules* **1998,** *31*, 1335-1340.

(189) Jordan, A. M.; Kim, K.; Soetrisno, D.; Hannah, J.; Bates, F. S.; Jaffer, S. A.; Lhost, O.; Macosko, C. W. Role of Crystallization on Polyolefin Interfaces: An Improved Outlook for Polyolefin Blends. *Macromolecules* **2018,** *51*, 2506-2516.

(190) Benkoski, J. J.; Flores, P.; Kramer, E. J. Diblock Copolymer Reinforced Interfaces between Amorphous Polystyrene and Semicrystalline Polyethylene. *Macromolecules* **2003,** *36*, 3289-3302.

(191) Liu, G.; Zhang, X.; Liu, Y.; Li, X.; Chen, H.; Walton, K.; Marchand, G.; Wang, D. Effect of Elastomer on Crystalline Transition and Deformation Behavior of Isotactic Polypropylene. *Polymer* **2013,** *54*, 1440-1447.

(192) Geyer, R.; Jambeck, J. R.; Law, K. L. Production, Use, and Fate of All Plastics Ever Made. *Sci. Adv.* **2017,** *3*.

(193) Jancar, J.; Dibenedetto, A. T. The Mechanical Properties of Ternary Composites of Polypropylene with Inorganic Fillers and Elastomer Inclusions. *J. Mater. Sci.* **1994,** *29*, 4651-4658.

(194) Lim, J. W.; Hassan, A.; Rahmat, A. R.; Wahit, M. U. Phase Morphology and Mechanical Properties of Rubber-Toughened Polypropylene Nanocomposites: Effect of Elastomer Polarity. *Polym.-Plast. Tech. Eng.* **2008,** *47*, 411-419.

(195) Momen, O.; Mehrabi-Mazidi, M.; Jahangiri, N. Isotactic Polypropylene (PP) Modified by ABS and $CaCO_3$ Nanoparticles: Effect of Composition and Compatibilization on the Phase Morphology, Mechanical Properties and Fracture Behavior. *Polym. Bull.* **2015,** *72*, 2757-2782.

(196) Rickard, M. A.; Meyers, G. F.; Habersberger, B. M.; Reinhardt, C. W.; Stanley, J. J. Nanoscale Chemical Imaging of a Deuterium-Labeled Polyolefin Copolymer in a Polyolefin Blend by Atomic Force Microscopy-Infrared Spectroscopy. *Polymer* **2017,** *129*, 247-251.

(197) Horváth, F.; Gombár, T.; Varga, J.; Menyhárd, A. Crystallization, Melting, Supermolecular Structure and Properties of Isotactic Polypropylene Nucleated with Dicyclohexyl-Terephthalamide. *J. Therm. Anal. Calorim.* **2017,** *128*, 925-935.

(198) Chen, Y.; Yang, H.; Yang, S.; Ren, P.; Zhang, Q.; Li, Z. Polypropylene Films with High Barrier Performance Via Crystal Morphology Manipulation. *J. Mater. Sci.* **2017,** *52*, 5449-5461.

(199) Sheng, Q.; Zhang, Y.; Xia, C.; Mi, D.; Xu, X.; Wang, T.; Zhang, J. A New Insight into the Effect of β Modification on the Mechanical Properties of iPP: The Role of Crystalline Morphology. *Mater. Des.* **2016,** *95*, 247-255.

(200) Kersch, M.; Schmidt, H. W.; Altstädt, V. Influence of Different Beta-Nucleating Agents on the Morphology of Isotactic Polypropylene and Their Toughening Effectiveness. *Polymer* **2016,** *98*, 320-326.

(201) Chen, Y.; Yang, S.; Yang, H.; Zhong, G.; Fang, D.; Hsiao, B. S.; Li, Z. Deformation Behavior of Oriented β-Crystals in Injection-Molded Isotactic Polypropylene by in Situ X-Ray Scattering. *Polymer* **2016,** *84*, 254-266.

(202) Zhang, Y.; Zhang, L.; Liu, H.; Du, H.; Zhang, J.; Wang, T.; Zhang, X. Novel Approach to Tune Mechanics of β-Nucleation Agent Nucleated Polypropylene: Role of Oriented β Spherulite. *Polymer* **2013,** *54*, 6026-6035.

(203) Tordjeman, P.; Robert, C.; Marin, G.; Gerard, P. The Effect of A, B Crystalline Structure on the Mechanical Properties of Polypropylene. *Euro. Phys .J. E* **2001,** *4*, 459-465.

(204) Rozanski, A.; Galeski, A. Controlling Cavitation of Semicrystalline Polymers During Tensile Drawing. *Macromolecules* **2011,** *44*, 7273-7287.

(205) Jiří, K.; Miroslav, R.; Josef, B.; Wolfgang, G. The Effect of Specific β-Nucleation on Morphology and Mechanical Behavior of Isotactic Polypropylene. *J. Appl. Polym. Sci.* **2002,** *85*, 1174-1184.

Appendix A: Toughen isotactic polypropylene with hybrid micelles

A.1 PCHE-PEE$_E$ micelles

Researches have shown that hybrid core-shell particles could potentially have advantages over rubbery particles since they enjoy the toughness benefits brought by rubbers while the tensile strength is not compromised with the presence of rigid particles.[59, 102] However, there are not a lot of good performing hybrid particles reported in the literature. As discussed in Chapter 2, PCHE-PEE$_E$ block copolymer can be synthesized in the same manner as PEP-PEE$_E$ by simply changing the monomer from isoprene to styrene, enabling us to study hybrid core-shell micelle particles with a glassy core and rubbery shell. We have successfully made a compositionally symmetric PCHE-PEE$_E$ with a total molecular weight of 40 kg/mol and PDI < 1.1. The polystyrene aliquot molecular weight was obtained using SEC and universal calibration and the block copolymer composition was calculated from ^{1}H NMR, which gave the total molecular weight of PCHE-PEE$_E$. The polydispersity was reported from the SEC result of PCHE-PEE$_E$. The SEC traces and ^{1}H NMR spectra of PCHE-PEE$_E$ and parent polymer PS-PB are shown in Figure A.1. The 1,2 contents in the PS-PB block copolymer were calculated to be 80% with ^{1}H NMR.

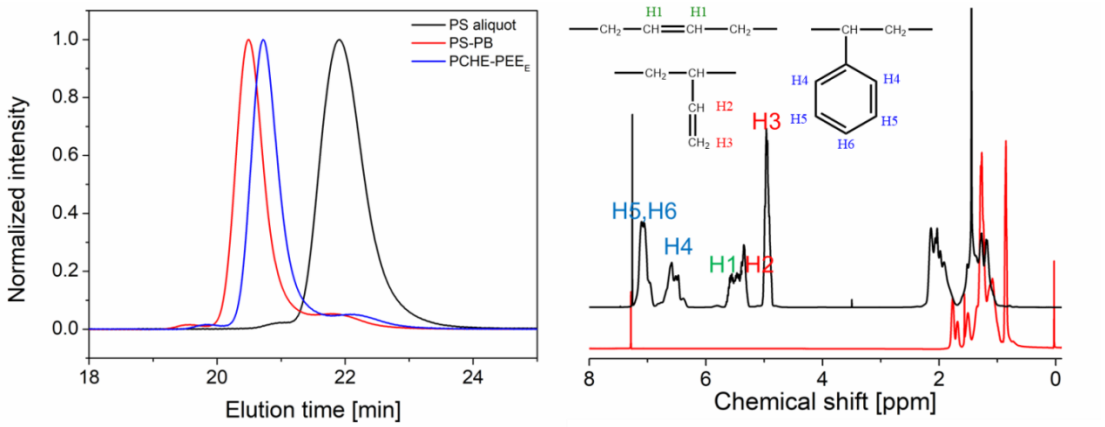

Figure A.1 SEC traces of PCHE-PEEE, unhydrogenated counterpart PS-PB and PS aliquot, and NMR traces of PCHE-PEEE and PS-PB with characteristic peaks assigned. The disappearance of peaks associated with aromatic hydrogen in the NMR spectrum and an invariant SEC trace indicate complete hydrogenation without degradation.

The PCHE-PEE$_E$ block copolymer was compression molded at 180 °C into 0.5 mm thick film. TEM and SAXS were used to investigate the morphology of this diblock copolymer. The results of TEM micrograph and room temperature small angle X-ray scattering (SAXS) profile are displayed in Figure A.2. TEM revealed the micro-phase separated lamellae structure with approximately a domain spacing of d = 25 nm, which is consistent with the first ordering peak at q^* = 0.23 nm^{-1} ($d^* = 2\pi/ q^*$ = 27 nm). These results suggest that the block copolymer is ordered at 180 °C, which is the temperature we conducted microcompounding with *i*PP at.

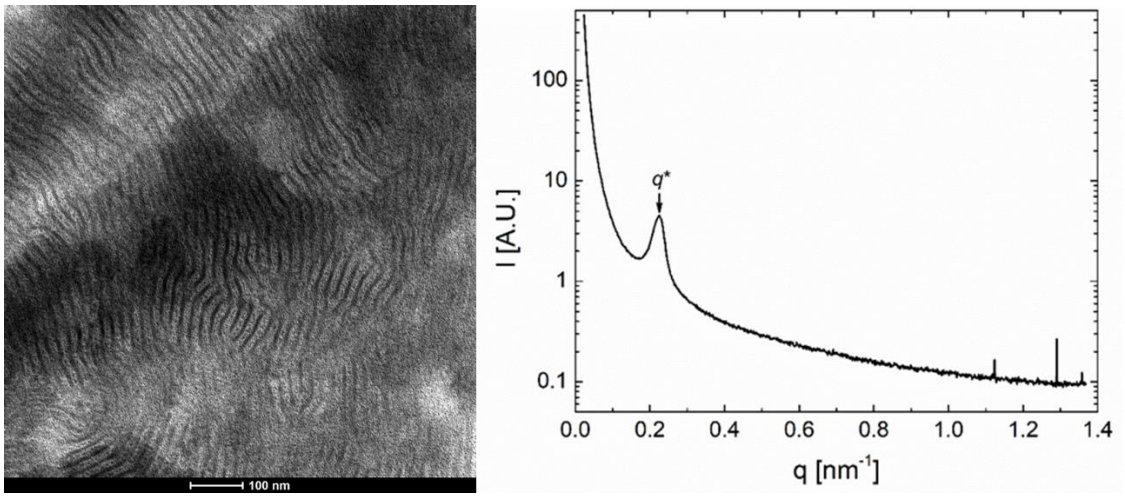

Figure A.2 TEM micrograph (left) and room temperature SAXS profile (right) of compression molded PCHE-PEE_E film.

The blends of PCHE-PEE_E/*i*PP with 5 wt%, 10 wt% and 20 wt% block copolymer have been prepared with a DSM microcompounder at 180 °C for 5 min and blend morphologies were investigated with TEM. The representative TEM images are provided in Figure A.3. The micelle sizes were very small and somewhat invariant to the composition, around 40 nm in diameter in all blends. They were also very uniformly dispersed with nearly no clusters observed.

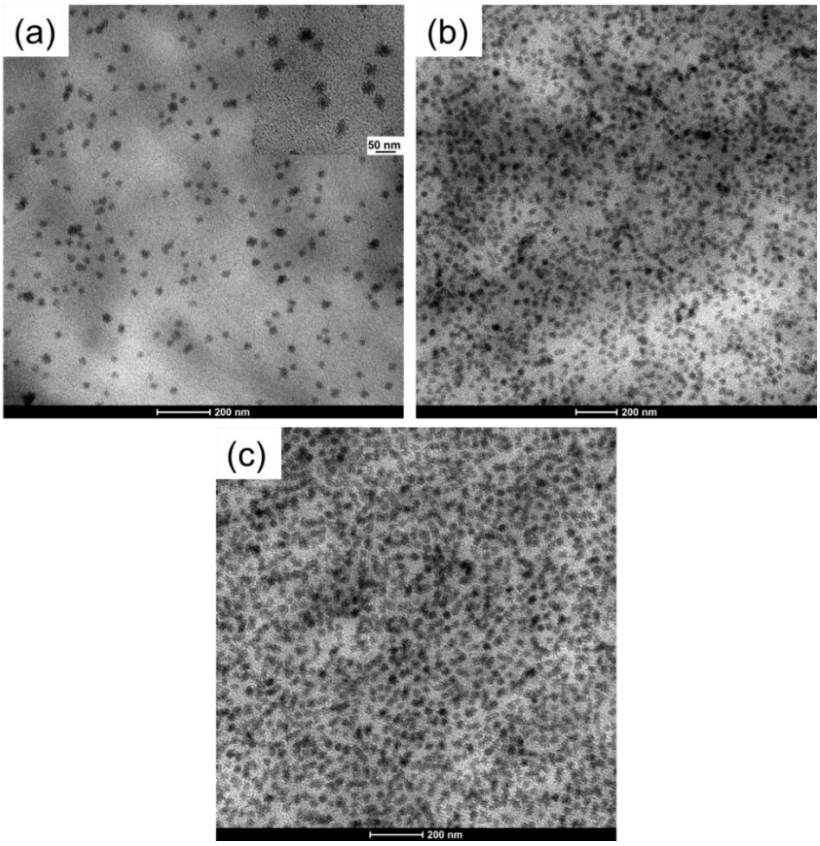

Figure A.3 Representative TEM images of (a) 5 wt%, (b) 10 wt% and (c) 20 wt% PCHE-PEE_E/*i*PP blends

The blend mechanical properties were evaluated with tensile testing. Representative stress-strain curves with different PCHE-PEE_E concentrations are presented in Figure A.4. The strain at break increased dramatically from 20% to 500% with merely 5 wt% block copolymer additives and nearly no loss in the yield stress was observed. Furthermore, the blends stayed transparent even with 20 wt% block copolymer possibly due to matched density ($\rho_{\text{PCHE-PEEE}} \approx \rho_{\text{CE50}}$[133]) and nano-scale micelle size. Various crosshead speeds were utilized to further investigate the mechanical properties of the 5 wt% blends (See Figure A.5). The blends demonstrated great mechanical properties compared

with neat *i*PP even at relatively high testing speeds and the yield stresses increased with crosshead speeds as expected since faster speed is equivalent to a lower temperature.

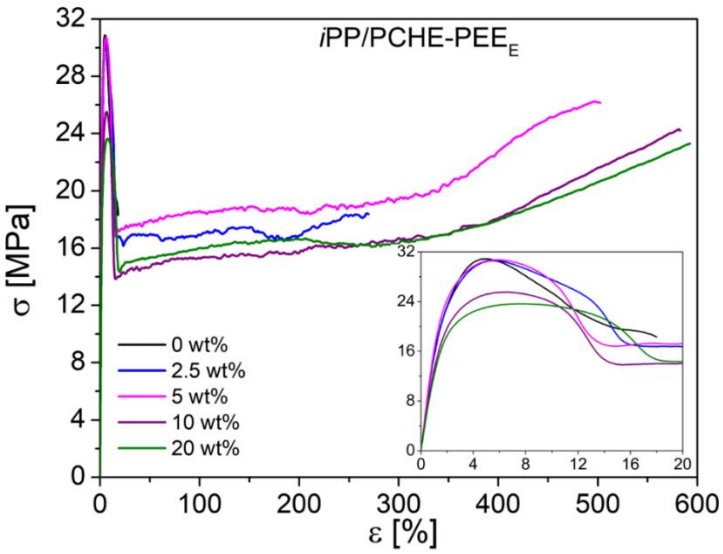

Figure A.4 Representative stress-strain curves of *i*PP/PCHE-PEE$_E$ blends with different block copolymer concentrations.

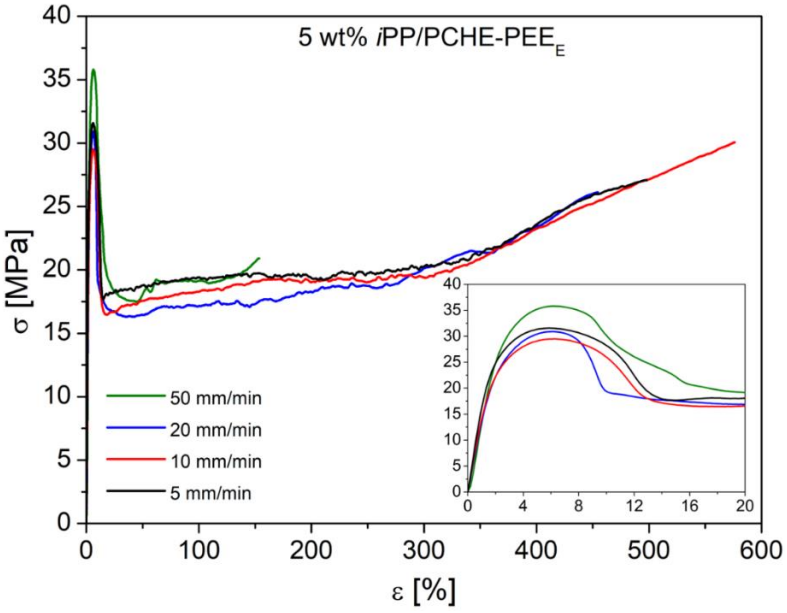

Figure A.5 Representative stress-strain curves of 5 wt% *i*PP/PCHE-PEE$_E$ blends with different crosshead speeds.

However, when evaluated with Izod impact testing, the blends modified with 5 and 10 wt% PCHE-PEE_E block copolymers were as brittle as neat *i*PP material with an impact strength of around 30 J/m. We suspect that in impact testing, the specimens were subject to a stress state that is close to plane strain, which makes it very difficult for the glassy core to cavitate. The cavitation events can be further investigated using in-situ SAXS while stretching the specimens.

A.2 PE-PEE_E micelles

Another hybrid micelle we can study is PE-PEE_E with semi-crystalline cores and rubbery shells. As discussed in Chapter 2, PE-PEE_E block copolymer can be synthesized in the same manner as PEP-PEE_E by simply switching the monomer from isoprene to butadiene. We have successfully made a compositionally symmetric PE-PEE_E with a total molecular weight of 48 kg/mol and PDI < 1.1. The polybutadiene aliquot molecular weight was obtained using SEC and universal calibration, and the block copolymer composition was calculated from the amount of added butadiene for the two blocks, which gave the total molecular weight of PE-PEE_E. The polydispersity was reported from the high-temperature SEC result of PE-PEE_E. The high temperature and room temperature SEC traces of PE-PEE_E and parent polymer $PB_{1,4}$-$PB_{1,4/1,2}$ are shown in. The high-temperature SEC was conducted at 135 °C with 1,2,4-trichlorobenzene (TCB) as the mobile phase and an RI detector. And with ^{1}H NMR as shown in Figure A.7, 1,2 contents in the second block of parent polymer $PB_{1,4}$-$PB_{1,4/1,2}$ were calculated to be 84%.

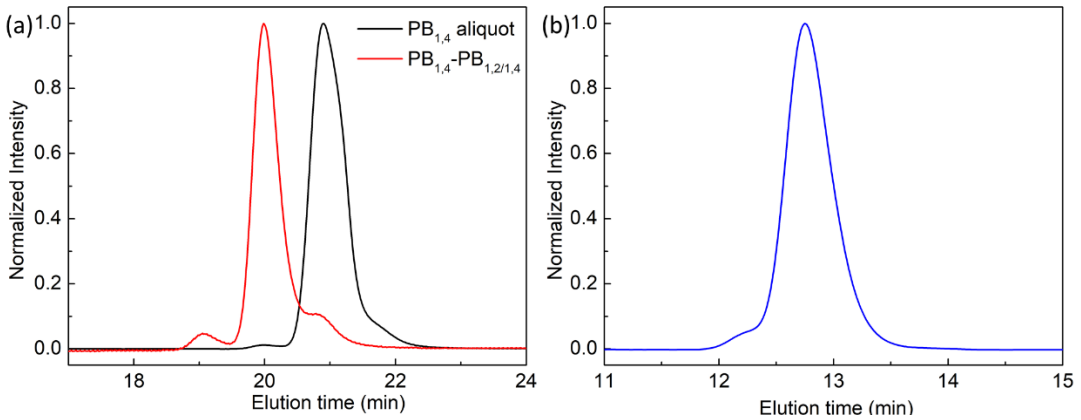

Figure A.6 (a) Room temperature SEC traces of PB aliquot and parent polymer $PB_{1,4}$-$PB_{1,4/1,2}$ and (b) High-temperature SEC trace of PE-PEE_E.

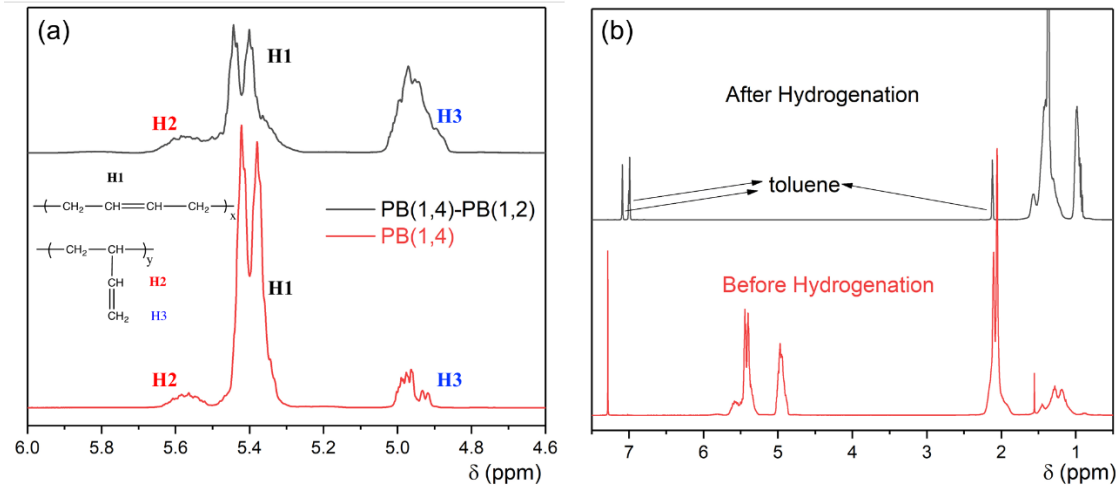

Figure A.7 ^{1}H NMR traces of (a) PB aliquot and parent polymer $PB_{1,4}$-$PB_{1,4/1,2}$ and (b) $PB_{1,4}$-$PB_{1,4/1,2}$ and PE-PEE_E. NMR of PE-PEE_E was conducted at 100 °C in d-toluene and the others at room temperature in d-chloroform.

To investigate the order-disorder transition of PE-PEE_E, a temperature ramp from 180 to 230 °C at a heating rate of 10 °C/min was performed on a rheometer to record the elastic modulus G´ and loss modulus G´´ at various temperatures as shown in Figure A.8. The order-disorder transition temperature (T_{ODT}) is around 215 °C where G´ drops dramatically, indicating that the PE-PEE_E block copolymer is ordered at micro-

compounding temperature, i.e. 180 °C. The morphology and mechanical properties of *i*PP/ PE-PEE$_E$ could be very interesting to investigate and provide some fundamental insights into the role of cavitation in toughening along with the study of PCHE-PEE$_E$ micelles.

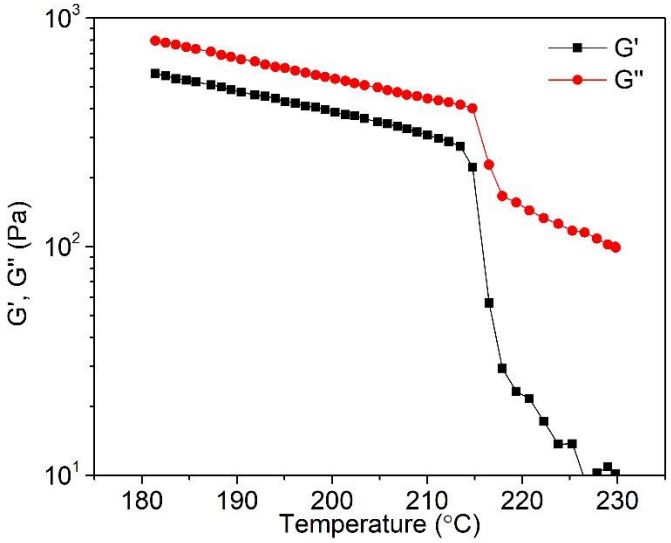

Figure A.8 Elastic modulus G´ and loss modulus G´´ of PE-PEE$_E$ at various temperatures

Appendix B: Isotactic polypropylene toughening with block copolymer micelles and beta crystal modification

The beta-form of isotactic polypropylene (β-*i*PP) has drawn enormous attention in the last decade because of much-improved impact resistance in comparison with the common monoclinic α form.[197-203] While the α phase is formed under conventional processing conditions, the beta form can be introduced by adding specific nucleating agents. In our work, we chose a commercially available beta nucleation agent used by other researchers[197, 200], dicyclohexyl-terephthalamide, to demonstrate the possibility of combining micelle toughening technique and beta modification to further enhance the impact strength.

We have prepared beta modified *i*PP with three commercial *i*PP materials at 180°C and nucleation agent loadings of 0.025, 0.05 and 0.1 weight percent in a twin-screw extruder. The information of the three *i*PPs used is summarized in Table B.1.

Table B.1 Commercial polypropylenes tested and their melt flow indices

*i*PP	Manufacturer	MFI g/10min (230 °C/2.16 kg)
HD915CF	Borouge (Abu Dhabi, United Arab Emirates)	8.0
Exxon 6262	ExxonMobil	2.8
Dow H314-02Z	Dow Chemical	2.0

These blends were injection molded into impact bars and subject to notched Izod impact testing according to ASTM D256. The impact strengths of all the beta modified blends are displayed in Figure B.1. We have only seen a 60% increase of impact strength in the Dow *i*PP modified with 0.025 and 0.05 wt% beta agents.

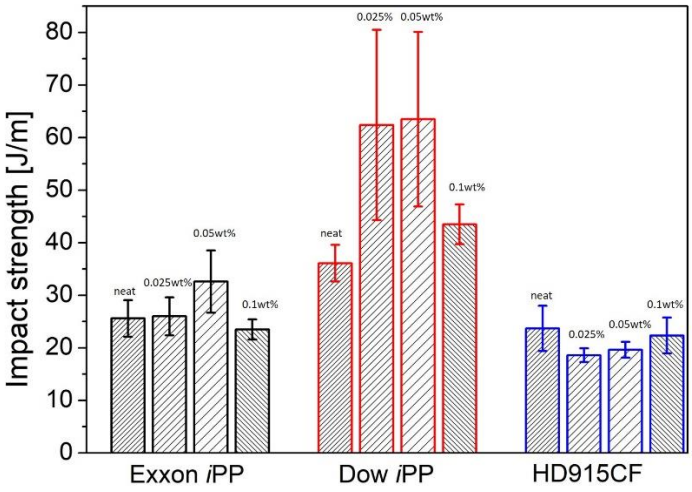

Figure B.1 Notched Izod impact strength of beta modified commercial *i*PPs.

A morphological study of these beta-crystallized Dow *i*PP samples was accomplished using scanning electron microscopy (SEM), following an etching procedure refined by Rozanski and Galeski[204]. Core layer surfaces were polished with a fine grit sandpaper and etched for two hours at room temperature in 0.7 wt% of potassium permanganate in a 5/4/1 by volume mixture of concentrated sulfuric acid, orthophosphoric acid, and distilled water. During these two hours of etching, the mixture was placed in an ultrasonic bath for 2 minutes every 20 minutes. Following etching, the samples were exposed to a series of four washes: diluted sulfuric acid (a 2/7 by volume mixture of concentrated sulfuric acid and water), hydrogen peroxide, distilled water, and acetone.

Each wash cycle was allowed several minutes in an ultrasonic bath. The dried samples were then sputtered with a 5nm thick iridium coating and imaged with a Hitachi S4700 scanning electron microscope.

Images of blends with 0.025 wt% and 0.05 wt% beta-nucleating agent loadings, as shown in Figures B.2 (a) and (b), revealed the presence of spherulitic structures, which appear to emanate from etched voids once occupied by the added nucleation sites. This sheaf-like morphology has been observed in previous work, and the greater toughness associated with beta-nucleated *i*PP has been attributed to bridging among spherulites and a greater continuity of the amorphous phase as compared to *i*PP containing alpha crystallites alone. Other beta-crystal morphologies have also been identified, in which increased toughness was likewise attributed to connections among crystallites[131]. An apparent coalescence of nucleation sites in the 0.05 wt% sample may indicate inadequate dispersal of nucleating agents or that an optimal nucleating agent loading, which has been observed in other studies[205], had been surpassed. An entirely different morphology, devoid of spherulitic structure, was exhibited by the 0.1 wt% loaded sample and is shown in Figure B.2 (c). This morphology indicates that the concentration of the beta crystallization agent is above the optimal range.

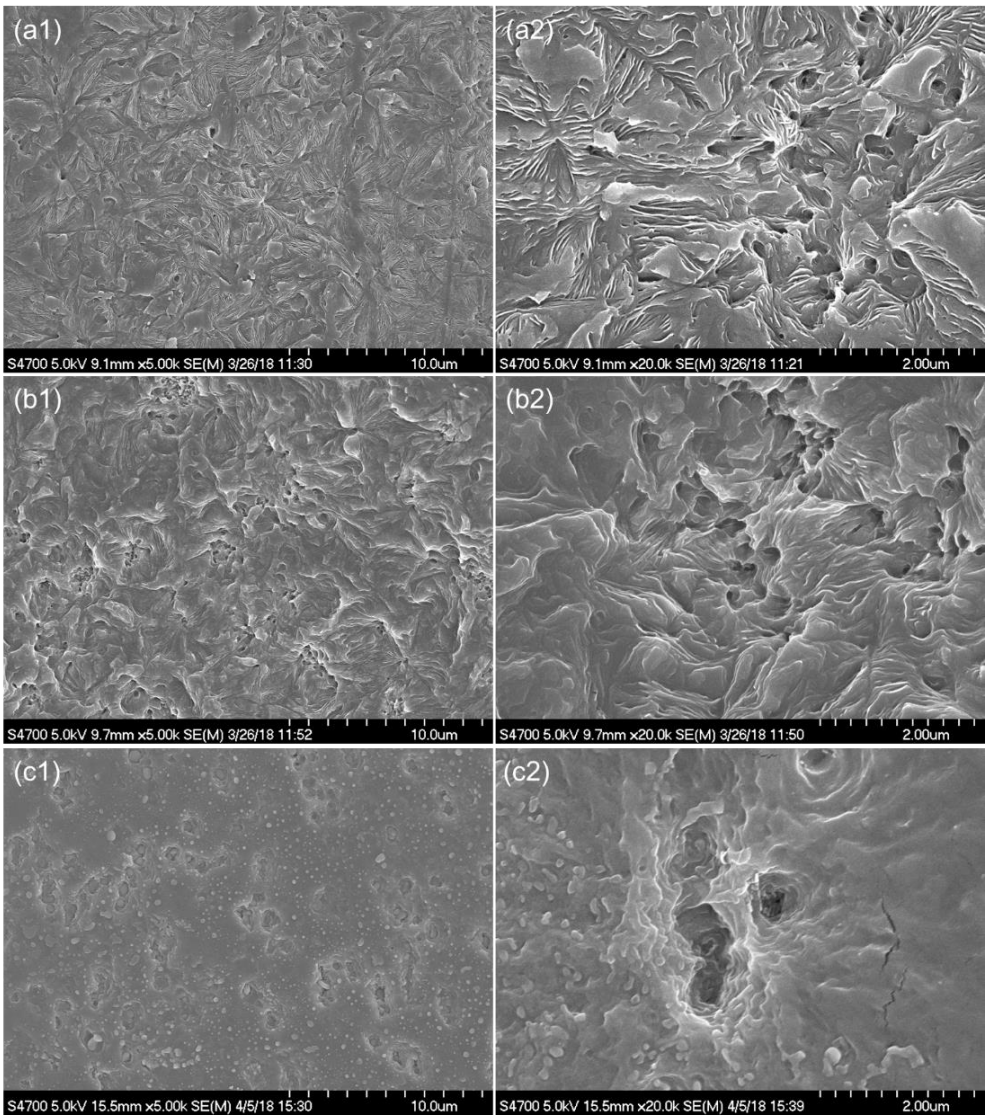

Figure B.2 SEM micrographs of Dow *i*PP modified with (a) 0.025wt%, (b) 0.05wt%, and (c) 0.1wt% beta nucleation agent. Low magnification pictures are in column 1 while higher magnification pictures are provided in column 2.

Wide angle X-ray scattering (WAXS) experiments were also performed on the core layers of the injection molded specimens to investigate the crystal structures of the beta modified *i*PPs (See Figure B.3). It is clear that a significant portion of beta crystals is formed in Dow *i*PP as evidenced by the distinct peak of (300) plane. Interestingly, the strongest intensity of the (300) comes from the 0.025 wt% sample, possibly suggesting that

0.025 wt% is sufficient in inducing a maximum level of beta crystallization. On the other hand, a very weak of (300) plane was observed in Exxon sample while no (300) peak was observed in HD915CF sample. We suspect that α crystallization agents are present and dominating in those polypropylenes according to the information provided by manufacturers, canceling the effects of subsequently added beta agents.

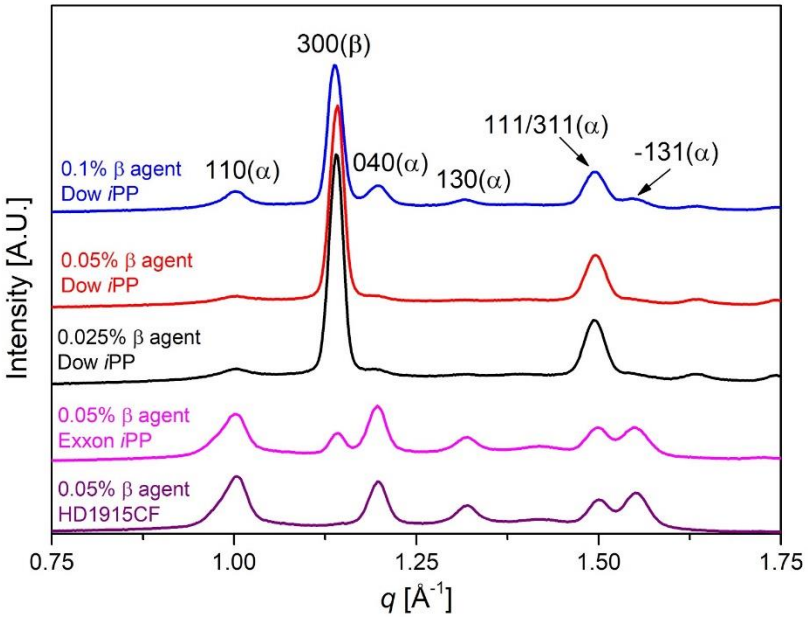

Figure B.3 WAXS profile of beta modified *i*PPs with the assignment of peaks associated with α and β phases.

With some optimization of the beta nucleation agent type and concentration, we can hopefully figure out the ideal conditions and then add the block copolymer micelles to achieve excellent impact resistance. It is worth noting that this method would decrease the tensile strength since the β phase has lower yield stress than that of α form and it will be further lowered with rubbery micelles. However, this can be mitigated with hybrid micelles as discussed in Appendix A.

Appendix C: Supporting Information for Chapter 3

MATLAB code for the interfacial tension fitting (Courtesy of Dr. Qile Chen)

Rheology_Fit.m

```
% initial guess of the gamma value
x0 = 500;

% ydata is Gm of mixture, the target value of fitting
ydata = complex(log(Gp_mix_exp), log(Gpp_mix_exp));

% create function
% xdata, Gp_iPP and Gpp_iPP are the w and Gm of iPP
fun = @(x,w)Fxn(x,w, xdata, Gp_iPP, Gpp_iPP);

% do the fit
x = lsqcurvefit(fun,x0,w,ydata)

% plot the fitted value using ww
ww = logspace(-2.5,2,1000)';

% calculate the theoretical (fitted) Gm
Gfinal = Fxn(real(x), ww, xdata, Gp_iPP, Gpp_iPP);
GpTheory = exp(real(Gfinal)); % <- G' output
GppTheory = exp(imag(Gfinal)); % <- G" output

% plot
% symbols are exp data
% lines are theoretical (fitted) data
loglog(w,Gp_mix_exp,'o',w,Gpp_mix_exp,'o',ww,GpTheory,ww,GppTheory)
```

Fxn.m

```
function Gfinal = Fxn( x, w, xdata, Gp_iPP, Gpp_iPP )

%lambdaM = 0.042; % unit: s
lambdaI = 0.001;
%etaM = 7511; % unit: Pa*s
etaI = 575;
```

```
%alpha = 1e-3; % unit: N/m
%R = 1e-6; % unit: m
lambda = real(x);
phi = 0.2;
maxI = 1;
Gmp = exp(real(spline(xdata,log(Gp_iPP),w)));
Gmpp = exp(real(spline(xdata,log(Gpp_iPP),w)));
Gm = complex(Gmp, Gmpp);

%GmTop = complex(0, w * etaM);
%GmBottom = complex(1, w * lambdaM);
%Gm = GmTop./GmBottom;
GiTop = complex(0, w * etaI);
GiBottom = complex(1, w * lambdaI);
Gi = GiTop./GiBottom;
sum = complex(0, 0);
for i = 1:maxI
   HiTop = 4*lambda*(2*Gm+5*Gi) + (Gi-Gm).*(16*Gm+19*Gi);
   HiBottom = 40*lambda*(Gm+Gi) + (2*Gi+3*Gm).*(16*Gm+19*Gi);
   Hi = HiTop./HiBottom;
   sum = sum + phi*Hi;
end
Gfinal = Gm.*(1+3*sum)./(1-2*sum);
Gpfinal = real(Gfinal);
Gppfinal = imag(Gfinal);
Gfinal = complex(log(Gpfinal), log(Gppfinal));
end
```

Appendix D: Supporting Information for Chapter 4

Sample calculation of K^* and ε_{vRo}

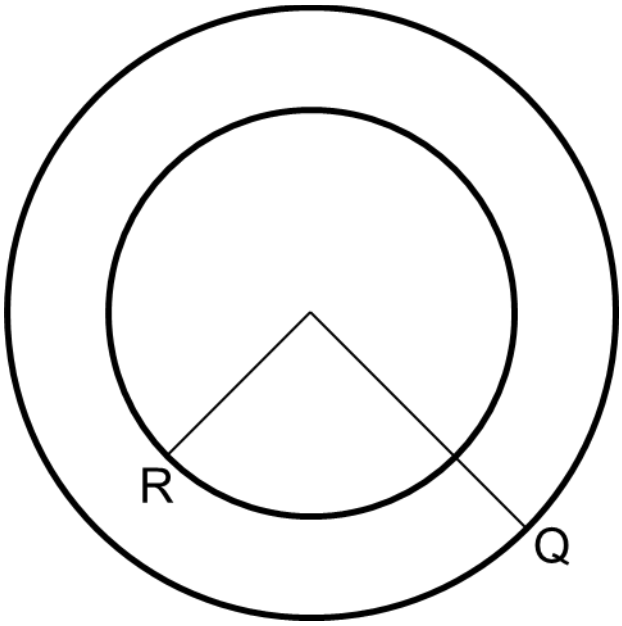

Figure D.1 Representative volume element (RVE) used to calculate the strains in rubber

Figure D.1 illustrates the RVE consisting of a spherical rubber particle with a radius of R encapsulated in a shell of rigid matrix of an external radius of Q. The method described by Bucknall and Paul leads to,

$$\frac{\varepsilon_{vR}}{\varepsilon_{vQ}} = \frac{G_m + 0.75K_m}{G_m + 0.75K_r + 0.75(K_m - K_r)\phi} = M_{RQ} \qquad (1)$$

where ε_{vR} and ε_{v0} are the volume strain at the particle-matrix interface and at the outer surface of the RVE (i.e. the overall average volume strain) respectively; G_m and K_m are the shear and bulk modulus of the matrix; K_r is the bulk modulus of the rubber; ϕ is the volume fraction of the rubber. M_{RQ} is called the volumetric strain magnification factor.

The $\varepsilon_{vR}/\varepsilon_{v0}$ ratio is calculated to be 1.49 using G_m = 0.6 GPa, K_m = 3.5 GPa, K_r = 2 GPa and ϕ = 5.4%. To include the matrix energy release, Bucknall and Paul introduced a

hypothetical rubber particle of the same radius but with a different bulk modulus (effective modulus) K^* subject to an initial volume strain ε_{vR0} given by,

$$K^* \varepsilon_{vR0} = K_r \varepsilon_{vR} \tag{2}$$

where ε_{vR0} can be obtained by setting K_r to zero, which gives $\varepsilon_{vR0}/\varepsilon_{v0} = (\varepsilon_{vR0}/\varepsilon_Q)/(\varepsilon_{v0}/\varepsilon_Q) = 4.39/1.49 = 2.9$ and $K^* = 0.69$ GPa.

In the article, the initial strain ε_Q (ε_v in the main context) experienced by the whole specimen was arbitrarily set to 0.5% and the initial volumetric strain of the hypothetical rubber particle $\varepsilon_{vR0} = 4.39\varepsilon_Q = 2.2\%$.

For a detailed derivation of the model and the equations, we refer the readers to the original papers by Bucknall and Paul.